12-2017

Investigations of Material Response to Fatigue Phenomena in Contacting Bodies

Aditya Walvekar
Purdue University

Recommended Citation

Walvekar, Aditya, "Investigations of Material Response to Fatigue Phenomena in Contacting Bodies" (2017). *Open Access Dissertations*. 1656.
https://docs.lib.purdue.edu/open_access_dissertations/1656

INVESTIGATIONS OF MATERIAL RESPONSE TO FATIGUE PHENOMENA IN CONTACTING BODIES

by

Aditya Walvekar

A Dissertation

Submitted to the Faculty of Purdue University
In Partial Fulfillment of the Requirements for the degree of

Doctor of Philosophy

School of Mechanical Engineering
West Lafayette, Indiana
December 2017

THE PURDUE UNIVERSITY GRADUATE SCHOOL
STATEMENT OF COMMITTEE APPROVAL

Dr. Farshid Sadeghi, Chair
    School of Mechanical Engineering
Dr. Anil Bajaj
    School of Mechanical Engineering
Dr. Charles Krousgrill
    School of Mechanical Engineering
Dr. Arun Prakash
    School of Civil Engineering

Approved by:
    Dr. Jay P. Gore
        Head of the Graduate Program

THIS DISSERTATION IS DEDICATED TO
MY PARENTS, AMRUTA & AVDHUT WALVEKAR,
MY SISTER, ANUSHREE, AND MY ADORABLE NEPHEW, AGASTYA
TO WHOM I OWE EVRYTHING

ACKNOWLEDGMENTS

First and foremost, I want to express my deepest appreciation to my advisor Cummins Distinguished Professor of Mechanical Engineering, Farshid Sadeghi for providing me with the unique opportunity to join his laboratory. His comments and guidance have had an invaluable impact on both my professional and personal life. Also, I would also like to thank Professor Anil Bajaj, Professor Krousgrill, and Professor Arun Prakash for serving on my advisory committee and providing their very important inputs.

I would like to acknowledge Schaeffler Technologies AG and Co. KG and Sentient Science for financially supporting this work. I would like to specially thank Mr. Martin Correns, Dr. Markus Dinkel, Mr. Toni Blass and Dr. Nick Weinzapfel from Schaeffler Group; Dr. Behrooz Jalalahmadi and Dr. Nathan Bolander from Sentient Science for their valuable contributions to my research projects.

I would like to thank my wonderful friends and lab mates at Mechanical Engineering Tribology Laboratory (METL): Chin-Pei Wang, Ben Leonard, Trevor Slack, Ankur Ashtekar, Anurag Warhadpande, John Bomidi, Andy Cross, Matthew Brouwer, Arnab Ghosh, Sina Moghadam, Neil Paulson, Lijun Cao, Mar Alonso Martinez, David Richardson, Zamzam Golmohmadi, Dallin Morris, Akhil Vijay, Arman Ahmadi, Kushagra Singh, Akshat Sharma. They made the work environment productive, friendly, and refreshing. Their help and inputs were immense help to my research.

My parents, Amruta and Avdhut Walvekar, and my sister, Anushree deserve my deepest appreciation for their love, care, encouragement, and sacrifices. Thank you for always supporting and believing me, which has got me to where I am today.

Last but not least, I would like to thank my friends and roommates: Rajas Karandikar, Ramdayalan Kumarasami, Astitva Tripathi, Akhil Salunkhe, Chinmay Joglekar; without their support surviving grad life would not have been possible.

TABLE OF CONTENTS

LIST OF TABLES

LIST OF FIGURES

ABSTRACT

Author: Walvekar, Aditya, Avdhut. Ph.D.
Institution: Purdue University
Degree Received: December 2017
Title: Investigations of Material Response to Fatigue Phenomena in Contacting Bodies
Major Professor: Dr. Farshid Sadeghi.

Investigating the fatigue performance of machine components has been of significant interest to improve reliability and reduce the maintenance costs. In the current work, analytical as well as experimental approaches are used to investigate material response to contact fatigue damage. In particular, two fatigue phenomena namely; fretting fatigue and rolling contact fatigue (RCF) are studied. Fretting fatigue is a damage mechanism observed in machine components subjected to fretting in tandem with fluctuating bulk stresses. A fretting test fixture was developed to investigate fretting fatigue behavior of AISI 4140 vs. Ti-6Al-4V in a cylinder-on-flat contact configuration. The critical damage value for AISI 4140 was extracted using the method of variation of elasticity modulus. The fretting fatigue lives obtained from the proposed computational fatigue damage model were found to be in good agreement with the experimental results.

The RCF investigation focuses on developing a modified 2D numerical model to simulate RCF damage in line contact configuration. First, a new computationally efficient approach is developed to investigate sub-surface initiated spalling in large bearings. Previously developed continuum damage mechanics based 2D fatigue model was modified to incorporate stress mapping procedure and dynamic remeshing tool to make the model computationally efficient. The new approach was validated against the previous numerical model for small rolling contacts. The scatter in the RCF lives and the progression of fatigue spalling for large bearings obtained from the model show good agreement with experimental results available in open literature. The ratio of L_{10} lives for different sized bearings computed from the model correlate well with the formula derived from the basic life rating for radial roller bearing as per ISO 281. Furthermore, the RCF model was extended to incorporate elastic-plastic material in order to investigate RCF of case carburized steels. A series of micro-indentation tests were conducted to obtain the hardness gradient in the case carburized 8620 steel. The hardness gradient in the material was modeled by changing the yield strength as a function of depth. The residual stress distribution due to carburization process was modeled by modifying the damage evolution law. The model was used to compare the rolling contact fatigue (RCF) lives of through hardened and case carburized bearing steel with different case depths. Based on the model results, the optimum case depths to maximize the RCF lives of the case carburized bearings at different loading conditions were obtained. This model was then modified to investigate RCF in refurbished case carburized bearings. Refurbishing process was simulated by removing a layer of material from the original surface after a set number of fatigue cycles. The original material properties, residual stresses and the fatigue damage accumulated prior to refurbishing in the remaining material were preserved. The refurbished geometry was then subjected to additional fatigue cycles until damage was detected. According to model results, more fatigue cycles prior to refurbishing enhance the total fatigue life of refurbished bearings. It was also found that beneficial impact of refurbishing on RCF lives of case carburized bearings depends on the relative values of case depth, contact half width, refurbishing depth.

1. INTRODUCTION

1.1 Background

Fatigue is the process of progressive damage accumulation which occurs when machine components are subjected to cyclic loading below the ultimate strength of the material. Fatigue causes localized damage which is manifested by the formation of micro-cracks, debonding, voids, etc. in areas of stress concentration within the material. These stress concentrations are typically associated with defects and inclusions at the microstructural level, grain boundaries which act as physical discontinuities in the polycrystalline material, or slip planes. The localized nature of fatigue damage coupled with random distribution of material microstructure results in a significant amount of variability in the fatigue life of machine components, making the fatigue life prediction a paramount aspect of the mechanical design. The fatigue failure process consists of three stages, crack nucleation, propagation, and catastrophic failure. Fatigue failures can be categorized as occurring in either the low or high cycle regimes based on the number of life cycles. Low cycle fatigue is characterized by significant plastic deformation which causes leads to early crack initiation and most of the life is spent in the crack propagation stage. On the other hand, little or no plastic strain can be detected at the macroscopic level in the high cycle fatigue regime. Plastic strains are confined to slip that occurs in a few poorly oriented grains. A major portion of fatigue life is spent in crack nucleation phase and once initiated the cracks propagates rapidly causing the component to fail. Therefore, in high cycle fatigue it is important to understand the factor governing the crack initiation process. Grain microstructure plays a significant role in the fatigue crack nucleation in the polycrystalline materials as grain boundaries can act as physical discontinuities.

The characteristics of two types of fatigue phenomena associated with contacting bodies namely, rolling contact fatigue and fretting fatigue will be reviewed in the sections which follow.

1.2 Rolling Contact Fatigue

Rolling element bearings (REB) are frequently used in machineries such as transmission systems, wind turbines, rail-wheel and cam-follower mechanisms. They are used to allow rotary motion and reduce friction between moving parts while supporting a significant amount of load. It is often presumed that if REBs are properly maintained and operated under conditions of elastohydrodynamic lubrication, thus the life-limiting failure mechanism is rolling contact fatigue (RCF) [1]. In rolling element bearings, RCF occurs when rolling bearing elements and the raceway roll with respect to each other, producing alternating contact stresses over a small volume. RCF manifests through a variety of different modes that eventually lead to failure.

The two most dominant modes of RCF failure are surface originated pitting and subsurface initiated spalling ([2], [3]). Pitting is characterized by the initiation of a crack at a surface irregularity e.g. dents or scratches [4]. Other causes for surface pitting can be improper lubrication which increases friction and wear or contaminants in the lubricant which can be trapped in the contact and leads to increase in the contact stress. On the other hand, sub surface spalling is characterized by micro-cracks originated below the surface at material inhomogeneities such as non-metallic inclusions which propagates towards the surface forming a relatively large spall. These cracks are often found to initiate in the region of maximum shear stress reversal below the surface. This mode of RCF is dominant when contacting surfaces are smooth, free of defects and operate under clean lubricated conditions ([1], [2]). Figure 1.1 compares the two modes of failure. As can be seen, in surface pitting, the crack propagates at a shallow angle to the surface until it reaches some critical length or depth at which time it branches and propagates to the surface, removing a piece of material [4]. The subsurface spalls are commonly deeper than those of surface failure.

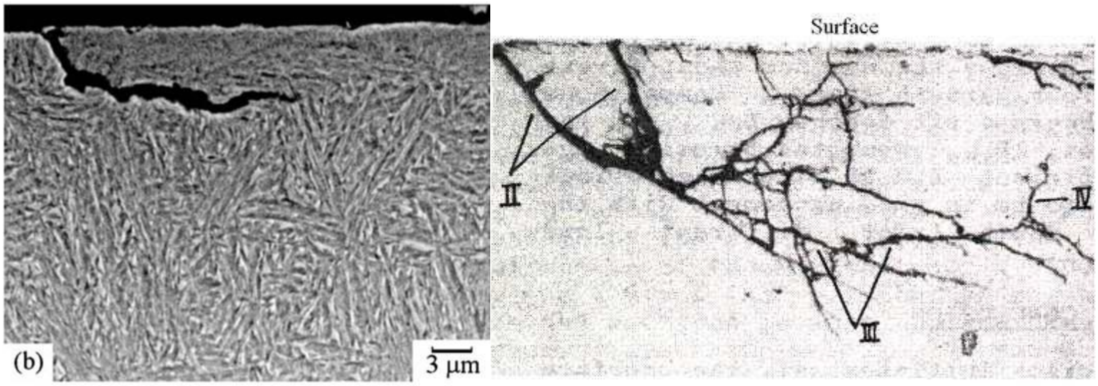

Figure 1.1: Surface pitting (left) and subsurface initiated spalling (right) [5].

1.2.1 Classical Fatigue vs. RCF

Investigation of rolling contact fatigue is more challenging compared to classical fatigue due to some key differences that distinguish them.

1. Classical fatigue failures generally initiate at the free surfaces due to existence of stress concentrating features such as scratches and/ or notches. Also, some common fatigue failures involving bending are caused by maximum tensile stress that occurs at the surface. The RCF damage is confined within subsurface material which makes it more difficult to locate and track prior to catastrophic failure to the load bearing surfaces.
2. In uniaxial or torsion fatigue, specimens are subjected to loadings that produce bulk stresses that cause damage to a large volume of the material and complete failure of the component. However, the stresses in RCF are highly localized in the region close to the non-conformal contact. Typical bearing contact half-widths are on the order of 100 – 500 µm. Consequently, very small volumes of the material are subjected to RCF.
3. In Hertzian line contact loading, there is a significant compressive component of hydrostatic stress in rolling contacts. Therefore, mode I crack growth is inhibited and crack propagation is dominated by mode II crack. However, there is not sufficient information regarding how compressive hydrostatic stress affects the Mode II crack growth.
4. Due to limited knowledge of mode II crack growth, it becomes difficult to apply common fatigue analysis methods such as linear elastic fracture mechanics (LEFM).

Further, the localized nature of stresses can cause the crack propagation to be affected by microstructural geometry of the material.

5. The state of stress experienced by a material point during a loading cycle is non-proportional [6]. Figure 1.2 illustrates the stress history of a material point at depth of the maximum orthogonal shear stress during a rolling cycle. In the figure the stress components are non-dimensionalized with the maximum Hertzian contact pressure, p_{max}, and the spatial location is non-dimensionalized with the Hertzian half width, b. Contrary to classical fatigue, different stress components are out of phase during a loading cycle. The shear stress, τ_{xz} is the only stress component which undergoes reversal, while normal stresses are always compressive. Due to this complex multiaxial stress distribution, the direction and magnitude of principle stresses vary significantly during a loading cycle.

The above points are some of the reasons classical fatigue results cannot be directly translated to RCF. Therefore, the RCF phenomenon has drawn attention of many researchers over the last century. The next section presents a review of important rolling contact fatigue life models and their limitations.

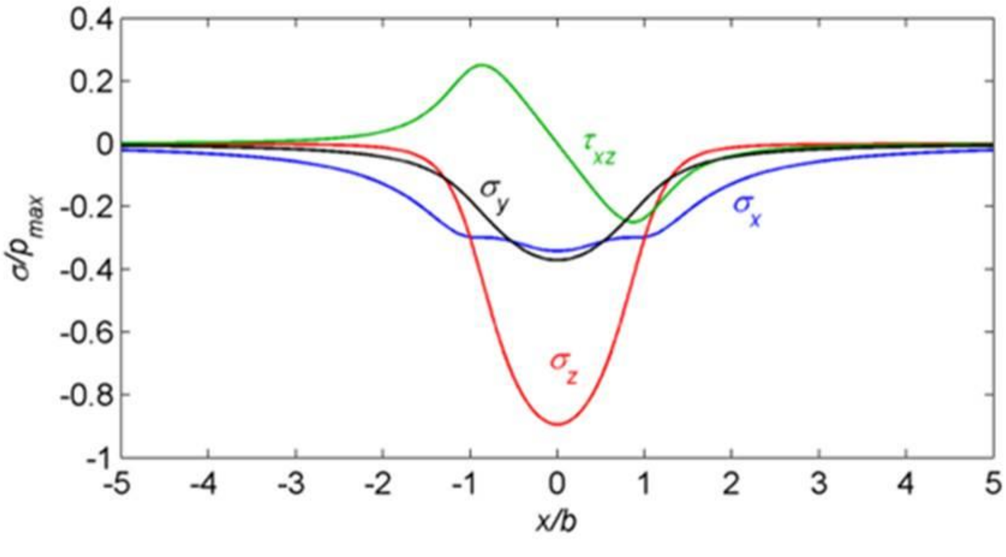

Figure 1.2: Stress history at a material point at the depth of maximum orthogonal shear stress as Hertzian line contact passes over the surface.

1.2.2 Review of RCF Life Models

A vast array of models has been developed to predict RCF failures in bearing components. According to Sadeghi et al. [7], these models can be classified as: (1) Empirical models; (2) Analytical models; and (3) Computational models.

- **Empirical models:** As discussed previously, it is difficult to directly correlate RCF to classical fatigue due to the major differences in underlying phenomena, which led most of the early investigators to pursue an empirical characterization of the phenomenon [8]. These empirical models were mostly probabilistic providing a statistical characterization of RCF based on variables obtained from extensive full-scale bearing fatigue testing. Hence, the empirical formulas possessed a limited scope of validity over operating conditions and bearing geometries. The first bearing life model which served as the basis for the first industrial bearing life standards [9] and many subsequent models for REBs was proposed by Lundberg and Palmgren [10], [11]. They correlated the scatter in the fatigue lives of REBs to the location of crack initiation. They postulated that a crack originates from sub-surface "weak points" of the in the vicinity of maximum orthogonal shear stress. Assuming stochastic distribution for the material weak points and applying The Weibull strength theory to the stressed volume in a pure Hertzian contact, Lundberg and Palmgren postulated following expression for the probability of survival, S for bearings subjected to N fatigue cycles –

$$\ln\frac{1}{S} \sim \frac{\tau_0^c N^e V}{z_0^h} \tag{1.1}$$

where, τ_0 is the maximum orthogonal shear stress in the contact at a depth, z_0. V represents the stressed volume. The exponents c, e and h must be determined experimentally. The parameter e is the Weibull slope for the experimental life data. The stressed volume V was assumed to be proportional to an annular volume of the bearing ring material directly affected by contact stresses

$$V \sim bz_0(2\pi r_r) \tag{1.2}$$

where, b and r_r correspond to contact half-width and raceway radius, respectively. Substituting for τ_0, z_0 and V in terms of the bearing dimensions and Hertzian contact parameter, the following load-life equation was obtained by Lundberg and Palmgren -

$$L_{10} = \left(\frac{C}{P}\right)^{p} \tag{1.3}$$

where L_{10} is the life cycles at which probability of failure is 10%, C is the bearing basic dynamic load rating and P is the equivalent load on the bearing. The exponent p is 3 for ball bearings having an elliptical contact area, 10/3 for roller bearings having modified line contact areas and 4 for pure line contacts. Though the LP theory was widely accepted, it ignores possibility of surface initiated failure, the effects of lubrication, contamination, surface shear traction, etc. It also assumes the contacting surfaces to be perfectly smooth, ignoring surface roughness, scratches and dents, which affects the stress distribution in the material.

Ioannides and Harris [12] attempted to overcome some of the limitations associated with the Lundberg-Palmgren model and to establish a link structural fatigue and RCF. Their first distinction was considering the bearing raceway to be composed of discrete material volumes. They assumed that fatigue crack can originate at any point in the material, therefore each discrete material volume will have its own probability of survival. The the overall failure risk for the bearing is the multiplication of failure risks of individual volumes. They also incorporated a stress threshold below which failure would not occur, similar to a fatigue limit in classical structural fatigue. Based upon these modifications, the bearing's probability of survival according to Ioannides and Harris [12] –

$$\ln\frac{1}{S} \sim AN^{e}\int_{V_R}\frac{(\sigma-\sigma_u)^{c}}{z^{h}}\,dV \tag{1.4}$$

where, σ is a stress quantity occurring at a depth z, σ_u is the stress threshold and A is an empirical constant. V_R are the volumes that are at risk of failure, i.e. where $\sigma > \sigma_u$. Here, the critical stress quantity, σ could be any stress causing the fatigue damage, e.g., the orthogonal shear stress, the maximum shear stress or the equivalent von Mises stress. The load-life equation was modified by Ioannides et al. [13] to

$$L_{10} = a_1\left[\frac{A}{\langle 1-\left(\eta\frac{P_u}{P}\right)^{w}\rangle^{\frac{c}{e}}}\right]\left(\frac{C}{P}\right)^{p}, P > P_u \tag{1.5}$$

where, a_1 is the reliability factor (a_1=1 for n=10), P_u is the load corresponding to the stress threshold σ_u. The threshold modification parameter, η accommodates the deviation in stress from Hertzian theory. Setting σ_u = 0 in (1.5) makes the Ioannides and Harris model equivalent to the LP model.

The current ISO standard [9] for rolling bearing life is based on modified Lundberg-Palmgren equation -

$$L_{10} = a_1 a_2 a_3 \left(\frac{C}{P}\right)^p \tag{1.6}$$

where a_1, a_2 and a_3 are life modifying factors that account for reliability, material and operating conditions.

The Lundberg- Palmgren Equation (1.1) can be rearranged to relate the life of a bearing for a given probability of survival S to the critical stress, τ_0 and the Weibull slope, e as follows

$$\mathrm{N} \propto \frac{z_0^{h/e}}{\tau_0^{c/e} V^{1/e}} \tag{1.7}$$

This indicates that the stress-life exponent depends on the scatter in bearing life data. However, exponents published in the literature appear to be independent of the life scatter. Therefore Zaretsky [14] presented a modified Lundberg and Palmgren [11] model with two changes: 1) eliminating the dependence of the stress-life relation on the Weibull slope e, and 2) eliminating the depth term. Additionally, Zaretsky changed the critical stress quantity to the maximum shear stress instead of the orthogonal shear stress. The equation developed by Zaretsky is given by

$$\ln\frac{1}{S} \sim \tau_0^{ce} N^e V \tag{1.8}$$

- **Analytical models:** As opposed to the empirical models, the analytical models consider the physical mechanisms of the failure process that occurs during RCF. Typically, the analytical models study either the crack initiation or crack propagation stage of the fatigue phenomenon by trying to address the underlying physical mechanisms responsible for RCF. Using the stress-strain behavior information for the materials, these models are usually combined with a material failure model to estimate the RCF lives.

The first analytical model for RCF phenomenon was developed by Keer and Bryant [15] who used fracture mechanics approach for crack propagation in rolling/sliding Hertzian contacts. They considered hydraulic effects and friction forces to study the propagation of inclined surface crack. They assumed crack nucleation life to be small compared to propagation life.

$$N \approx N_c = \frac{1}{2\beta_o}\int_{b_0}^{b} \frac{db}{\Delta \mathrm{K^m}} = \beta_0^{-1} p_{max}^{-m} c^{1-\frac{m}{2}} \tag{1.9}$$

where β_o and m are the Paris' law material parameters and ΔK is the stress intensity range at the crack tip. p_{max} is the maximum Hertzian pressure and c is the contact half-width. However, this model predicted fatigue lives orders of magnitude shorter than those predicted for similar Hertzian pressures using empirical models [16].

Hanson and Keer [17] extended this model to a 3D crack propagation model for line contact. They replaced the stress intensity factor in the Paris law by energy release rate, ΔG to account for mixed-mode propagation,

$$\begin{gathered} \frac{da}{dN} = C(\Delta G)^m \langle \Delta G - \Delta G_{th} \rangle \\ \Delta G = [(1-\nu)\Delta K_I^2 + (1-\nu)\Delta K_{II}^2 + \Delta K_{III}^2\,]/2\mu \end{gathered} \tag{1.10}$$

Where C and m are Paris law constants for the material and ΔG_{th} is a threshold energy release rate below which a crack does not propagate. This model predicted fatigue lives in the order of 10^7 cycles for maximum Hertzian pressures near 2 GPa, which is within the experimentally observed ranges.

Zhou et al. ([18], [19]) introduced a life model incorporating both the crack nucleation and crack propagation stages. The equation for final life was -

$$N = \frac{AW_c}{(\Delta\sigma - 2\sigma_k)^2 D} + \int_{a_1}^{a} \frac{db}{\mathrm{c}\Delta \mathrm{K^m}} \tag{1.11}$$

Where, A, c and m are material parameters, W_c is the specific fracture energy per unit area, $\Delta\sigma$ is the local shear stress range, σ_k is the friction stress for the material, D is the accumulated damage and ΔK is range of the stress intensity factor at the crack tip.

Bhargava et al. [6] developed a RCF life model in which the fatigue life were predicted from the accumulated plastic strain under cyclic contact stress in strain hardening materials. Jiang and Sehitoglu [20] computed RCF lives for crack initiation in line contacts using an elastic-plastic FE model incorporating the effects of cyclic ratcheting in conjunction with a multi-axial fatigue criterion [21]. Total damage D was assumed to be a sum of damage due to fatigue (D_f) and ratcheting (D_r). The rates of damage accumulation for the two phenomena were given by

$$\frac{dD_f}{dN} = \frac{(FP - FP_0)^m}{C}; \ \frac{dD_r}{dN} = \frac{\left|\frac{d\gamma_r}{dN}\right|}{\gamma_{cric}} \tag{1.12}$$

where, FP is a fatigue parameter, γ_r is the ratcheting strain, FP_0, m, C and γ_{cric} are material constants. The fatigue parameter FP was calculated from stresses and strains on the critical plane according to the following multi-axial fatigue criterion [21],

$$FP = \frac{\Delta\epsilon}{2}\sigma_{max} + J\Delta\gamma\Delta\tau \tag{1.13}$$

where, $\Delta\epsilon$ is the normal strain range , σ_{max} is the maximum normal stress, $\Delta\gamma$ is the shear strain range, $\Delta\tau$ is the shear stress range and J is a material constant. It was found that the combination of fatigue and ratcheting damage is the maximum at a depth corresponding to the occurrence of maximum orthogonal shear stress range, which is in agreement with predictions from the Lundberg-Palmgren theory.

- **Computational models:** Since, these analytical models assume a homogeneous description of the material microstructure and do not directly include the microstructural features in the life prediction mechanisms, they fail to capture the stochastic nature of RCF. However, in RCF, the localized nature of the contact stresses enhances the effects of these heterogeneous microscale features such as grain size and orientation, distribution of initial defects and material inclusions on the fatigue life and lead to the scatter in the RCF lives of otherwise identical bearings [22].

Raje et al. [23] presented a statistical model to estimate life scatter in rolling element bearings taking into account the material microstructure explicitly. The fatigue life N was assumed to be related to the critical stress and the corresponding depth -

$$N \sim \frac{z^r}{\tau^q} \tag{1.14}$$

The advantage of this model was that an explicit Weibull life distribution was not assumed, hence Weibull parameters from experimental data were not required. Instead, it was hypothesized that the variation occurring in the critical stress τ and corresponding depth z due to randomness in the material microstructural characteristics lead to scatter in fatigue life. They assumed that fatigue damage occurs along the weak planes that experiences the maximum alternating shear stress during the loading cycle. This assumption is similar to several multi-axial fatigue criteria proposed in literature ([24]–[26]). The geometric randomness and topological variability of material microstructure were simulated in the model using a Voronoi tessellation of randomly generated nucleation or seed points. They used discrete element method to capture the stress history during a rolling cycle for forty random Voronoi meshes. Applying Equation (1.14), they found that the scatter in the RCF lives obtained from the model results compared well with experimental results.

This model was further improved upon by incorporating a continuum damage mechanics based fatigue model to simulate the gradual material degradation due to fatigue [27]. In continuum damage mechanics, the Damage due to fatigue is incorporated through an internal damage variable D which varies from 0 to 1. Raje et al. [27] implemented the damage variable in their discrete element model through degradation of the springs. Damage evolution rate given by [28] was modified for shear stress driven rolling contact fatigue as following

$$\frac{dD}{dN} = \left[\frac{\Delta\tau}{\tau_r(1-D)}\right]^m \tag{1.15}$$

where $\Delta\tau$ is the critical stress range acting along the inter-element joint, τ and m are material parameters that are experimentally determined. The growth of damaged zones in the material is interpreted an spalling. They concluded that the initiation lives do not show much scatter. The scatter in the total lives (Weibull slope = 1.85) is primarily governed by the scatter in propagation lives.

Jalalahmadi and Sadeghi [29] developed the similar model in a finite element framework with elastically deformable material grains. They also used Voronoi tessellation to represent the randomness in the material microstructure. They studied the influence of the randomness inherent in the microstructure model on the magnitude and location of shear stress quantities supposed to be causing the RCF damage. Moreover, they found that introducing heterogeneity in the material model by varying the elastic properties and randomly distributing material flaws increased the fatigue life scatter. Jalalahmadi [30] also improved the model incorporating damage mechanics theory to simulate the RCF process similar to the model developed by Raje et al. [27].

These RCF models utilized a two-dimensional simplification of the material microstructure. However, 3D geometry is a more realistic representation of the subsurface material topology. Recognizing that the three-dimensional characteristics of the microstructure can significantly influence the fatigue lives, Weinzapfel et al. [31] extended the damage mechanics based RCF model by incorporating 3D Voronoi Tessellation. Since, constructing the model in a three-dimensional framework incurs a substantial increase in computational expense; Bomidi et al. [32] implemented several solution strategies to improve efficiency. Warhadpande et al. [33] and Bomidi et al. [34] included the effect of plasticity to accurately capture the stresses in the contact region under high loads.

1.3 Fretting Fatigue

Fretting is a combination of wear, fatigue and corrosion that can occur between contacting bodies due to small amplitude relative oscillatory motion between the surfaces [35]. The relative movement can result from external vibration, or can be the consequence of one of the members of the contact being subjected to a cyclic stress. Fretting damage may be classified into two different regimes depending on the magnitude of displacement between the contacting surfaces. In the partial slip regime, a portion of contact sticks while the remainder slips. In the gross slip regime, all the points in contact experience relative slip. Crack formation mainly occurs under partial slip conditions while gross slip conditions cause wear or galling. Fretting fatigue damage is prevalent in mechanical components. The combination of vibratory surface load and centripetal force in the dovetail blade/disk type attachments in gas turbine engines makes them vulnerable to fretting damage. Bolted or riveted structures such as aircraft wings subjected to alternating stress also experience fretting. Splines are usually designed to allow slight misalignments at the junction, which may increase their vulnerability to fretting damage. The corrosive conditions produced by the body fluids may give rise to fretting fatigue failures in bone plates used to fix fractured bones.

1.3.1 Classical Fatigue vs. Fretting Fatigue

Similar to rolling contact fatigue, fretting fatigue displays a number of important features that sets it apart from classical fatigue. As per Nowell [36], the following features must be considered in any experimental and analytical analysis or while designing susceptible machine components:

I. Due to the localized stress concentration at the contact, the magnitude of stress gradients is usually much higher than those associated with typical design features of components (e.g. notches and holes).

II. The non-proportional loading in the contact region caused by the non-linear nature of the friction at the contact interface, although the external loading is applied in a proportional fashion.

III. As cracks propagate away from the contact, they experience a variable R-ratio.

IV. Due to high localized stresses, the surface damage at the asperity level may accelerate crack initiation at the asperity scale.

1.3.2 History of Fretting Fatigue

The ‘fretting’ phenomenon has been researched for well over a century. In early days, it was recognized primarily as a surface damage phenomenon, which is now known as ‘fretting wear’. Eden et al. [37] in 1911 reported that brown oxide debris was formed in the steel grips of their fatigue machine in contact with a steel specimen. However, fretting fatigue was not specifically mentioned in their study.

The first experimental investigation of fretting was conducted by Tomlinson [38] in 1927. He designed two machines to produce small amplitude rotational movement between two annuli, and an annulus and a flat. A long lever system controlled the movement of the components. He established that the damage could be a result of relative movement of the components of amplitudes as small as a few millionths of an inch. He termed the relative motion of the component as 'slip'. Further, the resultant debris on his steel specimens was the red iron oxide which had arisen from chemical reaction with oxygen in the air, he coined the phrase 'fretting corrosion'. Warlow-Davies [39] in 1941 investigated the adverse effects of fretting of fatigue strength of the materials. They applied fretting damage on the gauge length of steel fatigue specimens and found that pitting of the surface reduces the fatigue strength. Later investigations by McDowell [40] showed that the combined action of fretting and fatigue, which is often the case in real applications, was much more adverse reducing the fatigue strength considerably. In 1958, Fenner and Field [41] demonstrated that fretting greatly accelerated the crack initiation process. Following these early investigations, the phenomenon where microslip between contacting surfaces leads to a reduction in fatigue life when compared to a plain fatigue was came to be referred as ‘fretting fatigue’.

1.3.3 Review of Fretting Fatigue Investigations

Multitude of inter-dependent parameters influence the fretting fatigue strength of machine components. These include materials, relative displacement amplitudes, normal force at the fretting contact, alternating tangential force, the contact geometry, surface integrity parameters, the environment, etc. Different types of experimental apparatus have been developed to study fretting fatigue at various design service conditions and determine the effects of fretting parameters on the fatigue lives. Fretting fatigue tests are generally performed in one of three types of loading configurations. In the ‘bridge’ configuration which was popular till 1990s, the bridge-type pads (Figure 1.1(a)) were simply clamped to the specimen by a proving ring or similar arrangement. The cyclic strain in the specimen causes relative motion between the bridge feet and the specimen. However, in this configuration, the conditions at the pad feet are difficult to characterize as the slip at each foot may not be absolutely identical. Nishioka and Hirakawa ([42], [43]) used cylindrical pads clamped against a flat specimen (Figure 1.3(b)). In this configuration, the pad alignment is less critical compared to the bridge type as flat-on-flat contact is avoided. Further, the theoretical stresses can be predicted by classical Hertzian contact equations. Important parameters for subsequent stress analysis (normal load, P, tangential load Q(t), and specimen remote stress $\sigma(t)$ can be readily monitored. Many other researchers, including Hills et al. [44], Szolwinski and Farris [45], Cortez et al.[46], Jin and Mall [47] adopted this configuration. The grip-type fretting fatigue test configuration (Figure 1.3(c)) is usually employed for flat fretting pads. Some researchers designed a test set-up closely related mimicking the geometry of the machine component under investigation. For example, Ruiz et al. [48], Papaniknos and Meguid [49], and Conner and Nicholas [50] performed fretting experiments in a dovetail geometry. Since, the large number of interacting variables which affect fretting fatigue makes experimental testing difficult, efforts to establish fretting fatigue test standards have been going on since the late eighties.

Attia and Waterhouse [51] summarized some of the previous works which examined the possibility of standardizing the fretting fatigue test methods and equipment. ASTM Task Group E0.05.05 has been developing a standard guide for fretting fatigue since 2007, with latest version ASTM E2789-10 [52] published in 2011. Neu [53] reviewed the current standards pertaining to fretting fatigue testing and discussed the new developments in the standardization.

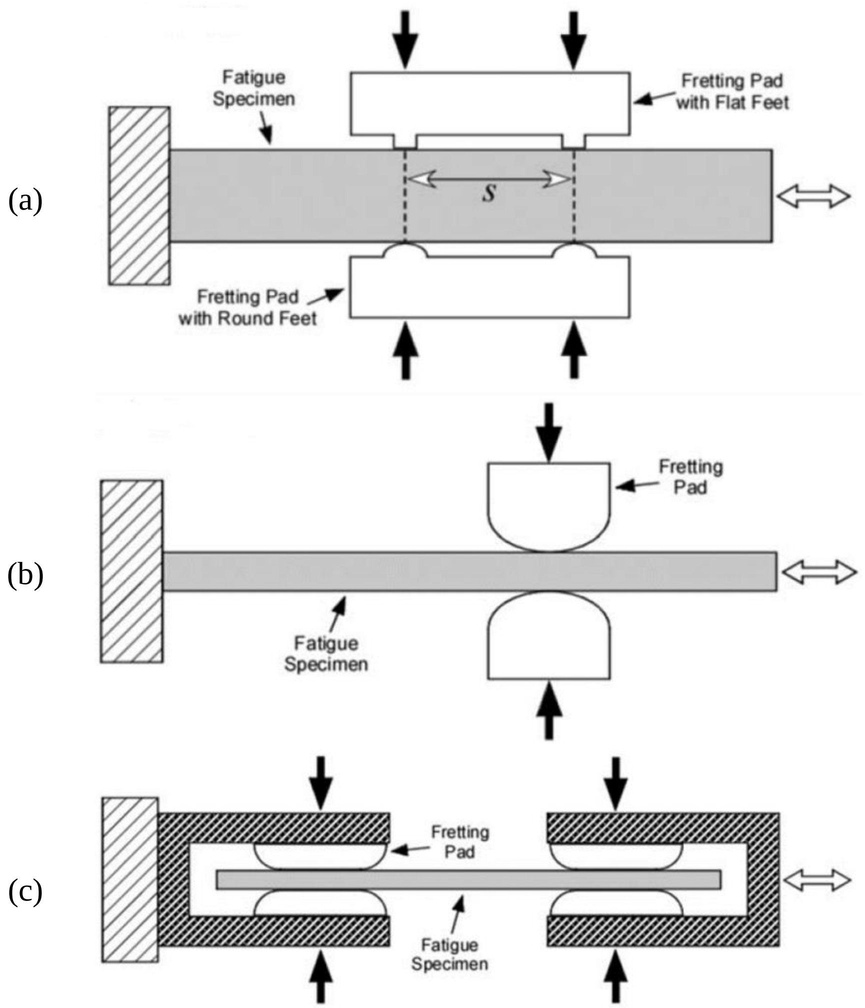

Figure 1.3: Fretting fatigue test configurations (a) Bridge-type, (b) Single clamps and (c) Grip-type [52].

Many different approaches have been developed to analytically model both crack initiation and propagation aspects of the fretting fatigue phenomenon. The initial fretting fatigue models can be divided into three distinct categories – (1) empirical models, (2) fatigue parameter based models, and (3) fracture mechanics based models [54]. The empirical models attempted to estimate fretting fatigue life as a function of applied alternating stress without taking into account the effect of stress concentration caused by the contact ([55]–[57]). Harris [58] developed a sensitivity index based on the difference in fatigue strength for plain fatigue and fretting fatigue. However, these empirical models did not attempt to determine the stress distribution along the contact surface for the applied loading conditions. Many investigators ([59]–[61]) studied the stress concentration at the edge of contact due to fretting and derived an equation for stress intensity factor as a function of axial stress amplitude and the frictional force. They studied different contact and loading conditions and determined the stress intensity factors required for onset of crack propagation and crack arrest. Golden and Grandt[62], Fadag et al. [63], Proudhon and Basseville [64] used fracture mechanics to analyze the fretting fatigue crack propagation rate. Recently, Giner et al. [65] and Baietto et al. [66] have used XFEM to predict fretting fatigue crack propagation. However, the drawback of the fracture mechanics approach is that it requires an initial crack length to start the analysis. Thus, it cannot predict the fatigue life for the crack initiation stage. As significant amount of life is consumed during this stage, there has been lot of focus to estimate the fretting fatigue life consumed in this stage. Early attempts frequently employed ‘special’ empirical parameters, some based on classical fatigue while some formulated solely for the fretting case. The two parameters proposed by Ruiz et al. [67] which come under the second category are particularly popular. The first Ruiz parameter was based on maximum frictional work the product of the local slip amplitude with the maximum shear traction.

$$\kappa_1 = (\tau\delta)_{\max} \tag{1.16}$$

Where, δ is the local slip amplitude and τ is the maximum shear traction.

The second Ruiz parameter which combined surface tangential stress with the first Ruiz parameter was more successful in predicting the location of crack initiation [68], though they lack in exact physical sense.

$$\kappa_2 = (\sigma_T\tau\delta)_{\max} \tag{1.17}$$

Elkholy [22] developed a fretting fatigue strength reduction parameter, σ_R which should be subtracted from plain fatigue strength. Here, u is the slip and f is the friction coefficient.

$$\frac{\sigma_R}{p_0} = 2f\left(1 - \exp\left(-\frac{Eu}{ap_0}\right)\right) \tag{1.18}$$

The more general classical fatigue based parameters consider the inherent multiaxial nature of the stress field in the fretting region. These include Socie [69], Nishioka and Hirakawa [70], Smith, Watson, Topper[71], etc. Socie [69] used maximum principle strain while Nishioka and Hirakawa [70] used maximum principle stress as a criterion for the location of fretting crack initiation. These parameters were also modified to incorporate the “critical plane” approach. For example, Szolwinski and Farris [45] assumed that crack initiation occur on the plane where SWT parameter is maximum.

$$\Gamma = \sigma_{max}\epsilon_a \tag{1.19}$$

Socie [72] developed a critical plane multiaxial parameter based on shear initiation. They postulated that during the shear loading frictional forces at irregularly shaped cracks surfaces reduce crack tip stress, thus retarding the crack initiation. However, normal load on the crack faces diminishes this impact [54]. Including these effects, they proposed the following parameter -

$$\mathrm{FS} = \Delta\gamma\left[1+\frac{\sigma_{n,max}}{\sigma_y}\right] \tag{1.20}$$

Where $\Delta\gamma$ is the shear strain range on the critical plane, $\sigma_{n,max}$ is the maximum value of direct stress across the plane, σ_y is the yield stress, and k' is a fitting parameter. Neu et al. [73] found that F-S parameter was most effective at prediction the location and initial growth direction of fretting fatigue cracks in PH 13-8 stainless steel. Fouvry et al. [74] applied Dang Van’s mesoscopic parameter (Dang Van et al.[75]) with averaging dimension of 6µm and found the fretting results to be consistent with plain fatigue in low alloy steel (30NCD16).

Nowell et al. [36] have reviewed more recent developments, including applying multiaxial initiation criteria to the fretting problem, size effects, crack arrests and characterizing crack initiation using asymptotic analysis.

1.4 Scope of this Work

As noted before, multitude of machine components are susceptible to fretting and rolling contact fatigue and the complex multi-axial nature of state of stress in the contact region makes their study a challenging research task. Further, the advancements in wind turbines where the contacts are an order of magnitude higher in scale and improvements in steel production and processing techniques to enhance the fatigue life of the material open new areas of research. Therefore, it is of significant importance to modify the current fatigue models for accurate predictions of fatigue lives for these new frontiers of research. The objectives of this investigation are to expand the continuum damage mechanics based fatigue model to determine the material response to fretting fatigue and rolling contact fatigue.

The second chapter presents the experimental investigation of the fretting fatigue behavior of AISI 4140 vs. Ti-6-4 in a cylinder-on-flat contact configuration. It also discusses a microstructure sensitive computational model based on continuum damage mechanics developed to simulate the experiments.

Chapter three onwards, this dissertation focus on the study of rolling contact fatigue in 2D line contact configuration. This study utilizes an existing fatigue model as a basis. However, the existing model requires significant computational effort to study large rolling contacts. Since large bearings employed in wind turbine applications have half-contact widths that are usually greater than 1 mm, chapter three presents a modified computationally efficient approach to investigate RCF life scatter and spall formation in large bearings. It consists of a Delaunay triangle mesh and stress mapping to improve efficiency and dynamic remeshing tool for mesh refinement to retain accuracy in stress calculations around the fatigue damage. The model is applied to obtain the L_{10} lives and fatigue life scatter for different half-contact widths at fixed maximum contact pressure. An equation for the ratio of L10 lives for different half-contact widths is derived based on the basic life rating for radial roller bearing as per ISO 281 to validate the model results. The effect of random distribution of initial defects on the fatigue lives for different contact widths is also investigated.

The RCF models developed till now assumes homogeneous pristine material with uniform distribution of material properties. However, the case carburized material which is getting popular in the manufacturing of high performance ball and rolling element bearings, is characterized by the hardened exterior and gradient in the material properties as a function of depth. Therefore, chapter four presents an elastic-plastic finite element model based on micro-indentation tests to investigate the rolling contact fatigue of case carburized bearings.

It considers both yield strength and residual stress gradient within the material due to carburizing process. The model is used to compare the rolling contact fatigue (RCF) lives of through hardened and case carburized bearing steel with different case depths at contact pressures ranging from 2 to 3.5 GPa. The model results are used to obtain the optimum case depth in order to maximize the RCF lives for the applied load.

Chapter 5 builds upon the RCF damage model developed in Chapter 4 to add the capability to simulate RCF in refurbished bearing made from case carburized steel. To simulate the refurbishing process, accumulated damage is calculated for a set number of fatigue cycles (fatigue cycles prior to the refurbishing) with the original bearing geometry. Then, a layer of preset depth (refurbishing depth) is removed from the from the top of the random Voronoi domains preserving the original material properties, residual stresses and the accumulated fatigue damage in the remaining material. The model is implemented for various refurbishing depths and number of fatigue cycles prior to the refurbishing, to analyze their influence on the life of refurbished case carburized bearings. The results are used to compare the improvement in the RCF lives due to refurbishing of case carburized steels with different case depths and through hardened steel.

Finally, Chapter 6 summarizes the developments made in this dissertation and offers recommendations for further research.

2. EXPERIMENTAL AND NUMERICAL ANALYSIS OF FRETTING FATIGUE

2.1 Introduction

Low amplitude tangential relative oscillatory motion between contacting bodies causes different forms of fretting damage such as pits, scarring, and material transfer on the surface. If the material is concurrently subjected to partial slip fretting and fluctuating bulk loading, the geometrically significant stick zone in the fretted area causes a stress concentration at the contact region resulting in premature nucleation and acceleration of crack growth when compared to fatigue situations without fretting [76]. This type of fatigue damage is known as fretting fatigue.

A number of mechanical, physical and environmental factors affect the fretting fatigue degradation process. These primarily include macroscopic factors such as bulk stress amplitude, contact geometry, normal contact load, coefficient of friction, slip amplitude, frequency, material properties, and temperature [56]. Due to the complex nature of the problem and its significance in the engineering applications, extensive research work has been undertaken over the past decades to characterize the fretting fatigue phenomenon both experimentally and analytically. Depending on the objective of the tests, fretting fatigue tests can be performed in various contact and loading configurations: single clamp loading configuration (Szolwinski and Farris [45], Cortez et al. [46], Jin and Mall [47]), grip type loading configuration (Hutson et al. [77]), and the bridge type loading configuration (Rayaprolu and Cook [55], Pape and Neu [78]). Many investigators have studied the crack initiation process with strain or critical plane based parameters such as Smith-Watson-Topper (SWT), and Fatemi-Socie (FS) which predict fretting fatigue initiation life from uniaxial fatigue tests. Ruiz parameters have also been used to investigate crack initiation in fretting fatigue. Lykins et al. [79] have compared several commonly used fatigue parameters and found that strain or critical plane based parameters are more effective in predicting cycles to crack initiation and its location. Quraishi et al. [80], Aghdam et al. [81], Zhang et al. [82], and Hojjati-Talemi and Wahab [83] have employed continuum damage mechanics approach for predicting crack formation in fretting. Scatter in fretting fatigue has been analyzed by Golden et al. [84] using probabilistic analysis to predict total life and Slack et al. [85] using the randomness of material microstructure topology to predict initiation.

In the current work, experimental results for the line contact between an AISI 4140 flat specimen and Ti-6-4 cylindrical contact pads are presented for the single clamp loading configuration. Figure 2.1 illustrates a schematic of the single clamp fretting fatigue tests for cylinder on flat contact configuration as given in [52].

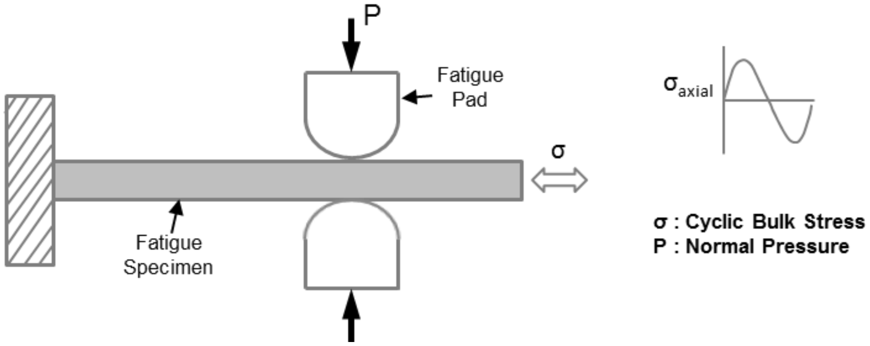

Figure 2.1: Fretting fatigue test configuration as given in ASTM standard [52].

The focus of the analytical part of this work is to develop a new approach to estimate fretting fatigue life using damage mechanics. A finite element model was developed using the commercial FEM software ABAQUS to evaluate the stress at the microstructure level. In order to incorporate the material randomness and disorder, the internal topology of the material microstructure is modeled using Voronoi tessellation with Voronoi cells representing grains of the material microstructure. Gradual material degradation induced by fretting fatigue is modeled using damage mechanics. Randomly generated Voronoi domains were subjected to fretting fatigue loading conditions and the fatigue damage model was applied to estimate the fretting fatigue lives and conduct life variability studies. Life estimates from analytical model compare well with the experimental results conducted as a part of this investigation.

2.2 Fretting Fatigue Test Rig

2.2.1 Experimental Setup

A fretting fatigue test rig was designed and developed to investigate the fretting fatigue behavior of an AISI 4140 specimen in contact with two Ti-6-4 pads. The contact pads are modularly designed so that the rig is capable of performing experiments with different contact configurations i.e. point contact (sphere on flat), line contact (cylinder on flat) and area contact (flat on flat). Also, by changing the geometry of contact pads, it is possible to perform tests in both bridge type and single clamp type loading configurations. In this study, experiments were conducted under the single clamp configuration with line contact. A schematic of the fretting test rig is shown in Figure 1.2. The test rig uses a 100 kN (22 kip) capacity Material Testing System (MTS) 810 machine. This system has hydraulic actuators capable of applying a precise axial load to the specimen gripped between the hydraulic clamps. The actuator is attached to the bottom grip while the top grip is attached to the crosshead which is held stationary. The position of the crosshead can be adjusted in order to incorporate various specimen sizes. The MTS machine is controlled by a computer and MTS Flex-Test SE which also acts as a data acquisition system. The amplitude and mean of the sinusoidal axial load applied to the specimen can be controlled via computer. In this study, the frequency was kept constant at 5 Hz to ensure that the rig was operated with minimal vibrations and the tests were completed in a reasonable amount of time. The MTS contains a load cell between the bottom grips and the actuator to measure the axial load applied to the specimen. In the case of fretting fatigue, the fretting fixture attached to the test frame applies normal contact load to the specimen. Since axial bulk load is applied at the bottom end of the specimen while the top end is held stationary, tangential force (F_T) is induced between the specimen and contact pads. This tangential load varies in phase with the applied bulk axial load. Due to the presence of this tangential load, different axial loads (F_u and F_b) are experienced by the specimen sections above and below the contact area. A second load cell is located between the crosshead and the upper grip of the MTS machine to measure the axial load on the upper section of specimen. The difference between the axial loads in the lower and upper sections of specimen is the tangential load transmitted between the pads and specimen:

$$F_b - F_u = 2F_T \tag{2.1}$$

Figure 2.2 depicts the force flow in the test rig. In order to apply the fretting loading to the specimen, the fretting fixture was mounted on the MTS frame and the specimen was clamped from both sides. The CAD model of the designed fretting fixture is shown in Figure 2.3. In this configuration there is a cylindrical pad on each side of the specimen.

Normal contact force is applied using a load screw. An inline load cell is added to continuously monitor the normal force. The edges of the specimen and the contact pads must be aligned to minimize the stress concentration at the edges. Therefore, the plates carrying the contact pads were supported with precision shafts and all parts were precision machined. Oil free bushings were used between the plates and the shafts since they are more precise than linear bushings. Since the position of the specimen is fixed by the MTS grips, the contact pads must be moved for contact alignment. If the contact pads are not centered properly, the specimen will bend due to the non-symmetric loading. This would also apply a side load to the MTS hydraulic actuator. The positioning mechanism centers the contact pads on the specimen automatically as the normal load is applied using the load screw. The two contact pads are attached to the plates numbered 2 and 3. Plates 1 and 3 are constrained to float together on the support shafts. The load screw is threaded into the plate 1 and adjusts the position of the plate 2 on the support shafts with respect to the plate 3. To apply the normal load, load screw is rotated so that it pushes the plate 2 towards the specimen. After the cylindrical pad on plate 2 comes into contact with the specimen; load screw is further turned to pull plate 3 towards the specimen. Any imbalanced force would move plates 1 and 3 assembly until the force is again balanced. After desired normal load is achieved, a lock nut is used to prevent the load screw from relaxing while in operation. In order for plates to move freely on the support shafts, there must be a clearance between the bushing and the shafts; this would cause the plates to vibrate during the test. To avoid this, the top support bars (Figure 2.4) are affixed to the plates after the desired normal load is achieved. The addition of the top support bars negligibly altered the applied normal load. The bars also add to the stiffness of the test rig. Figure 2.4 shows the fretting fatigue fixture constructed for this investigation and mounted on the MTS machine.

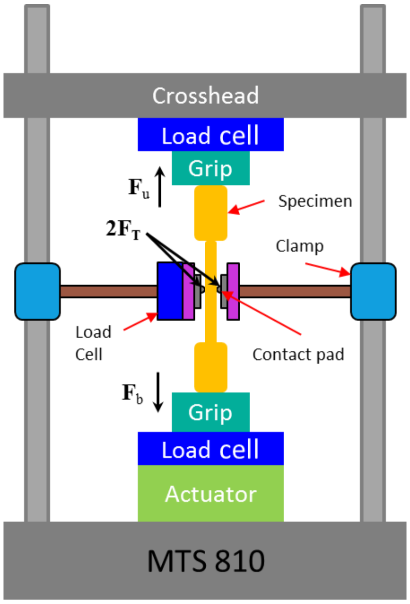

Figure 2.2: Schematic of fretting fatigue test rig.

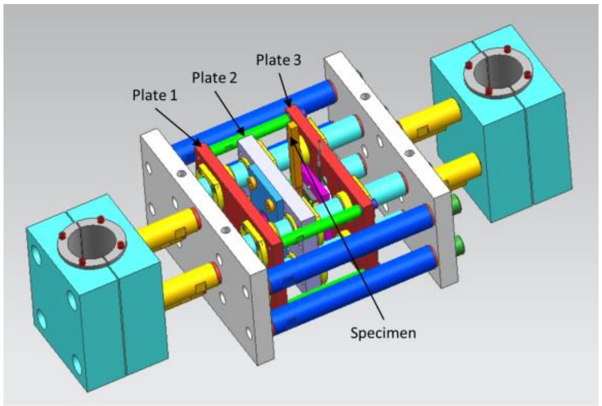

Figure 2.3: CAD model of fretting fatigue test fixture.

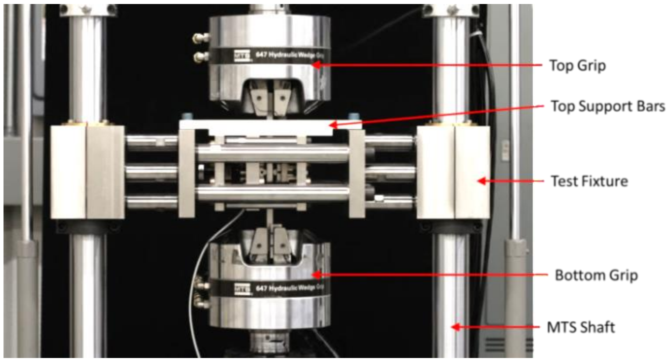

Figure 2.4: Fretting fatigue fixture mounted on MTS machine.

2.2.2 Specimen and Contact Pad Geometry

In this investigation, the flat tensile specimens were AISI 4140 steel while the 5 mm radius cylindrical pads were made from Ti-6-4. For a normal force of 11 kN the contact has a Hertzian pressure of 3 GPa and half width of 364 µm. The fatigue specimen dimensions are the same as those used by Cortez et al. [46] except for an extended griping section. To avoid edge effects, both the specimen and cylindrical pads are edge relieved. The contacting surfaces were ground to surface finish of $R_a = 0.2$µm. Figure 2.5 shows a CAD drawing of the tensile specimen and the contact pad.

Contact pads are attached to the fretting fixture through contact pad holders. Figure 2.6 shows the assembly of contact pad in the holder. Contact pads are placed into the V-groove in the holder. The friction between the contacts pads and the groove walls and set screws prevent the pads from rolling caused by the tangential force (F_T).

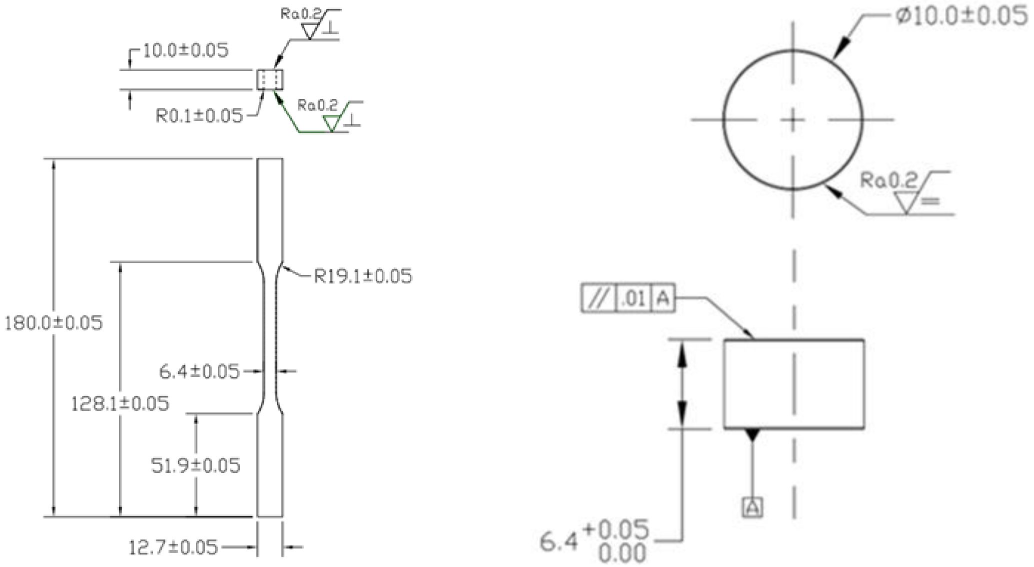

(a) (b)

Figure 2.5: Geometry and dimensions of (a) Specimen; and (b) Contact pad (all the length dimensions in mm and the surface roughness '*Ra*' is in µm).

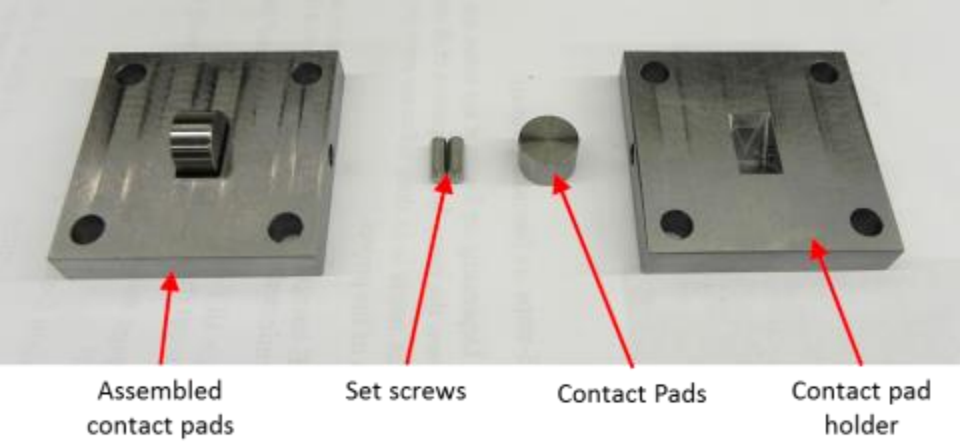

Figure 2.6: Assembly of contact pads in the contact pad holder.

2.3 Experimental Results

2.3.1 Fretting Fatigue Tests

Fretting fatigue tests were conducted under completely reversed constant-amplitude axial load control conditions (R = -1) at 5 Hz frequency. The amplitude of the axial bulk stress was varied from 100 MPa to 600 MPa while the normal force was held constant at 11 kN (peak Hertzian pressure of 3 GPa). The bulk stress (σ_0) is calculated by dividing the applied axial force (F_b) measured by the bottom load cell by the cross sectional area of the specimen under the contact region. Axial force applied by the actuator was controlled throughout the test. The force at the top of the specimen, actuator displacement and the applied normal load were recorded. Table Table 2.1 shows the summary of the experimental conditions and corresponding fretting fatigue lives. F_T is the amplitude of the tangential load between the specimen and contact pad during the 1000th cycles while F_N is the average contact force during the same period of time. The stiffness of the test rig defines the variation of $\mathrm{F_T}$ with respect to the change in bulk stress. The linear relationship between $\mathrm{F_T}$ and σ_0 evident in Table Table 2.1 states that the stiffness of the test rig was same for all the tests and the only parameter varied during the test was the applied bulk stress. McVeigh and Farris [86] showed that maximum fretting stress ($\sigma_{fretting}$) at the trailing edge of the contact can be approximately expressed as;

$$\sigma_{fretting} = \sigma_0 + 2p_h\sqrt{\frac{\mu F_T}{F_N}} \tag{2.2}$$

Figure 2.7 illustrates the fretting stress vs. life for AISI 4140 against Ti-6-4. As expected, it can be seen that for the fixed contact pressure, as the σ $_{\text{fretting}}$ increases fretting fatigue life decreases.

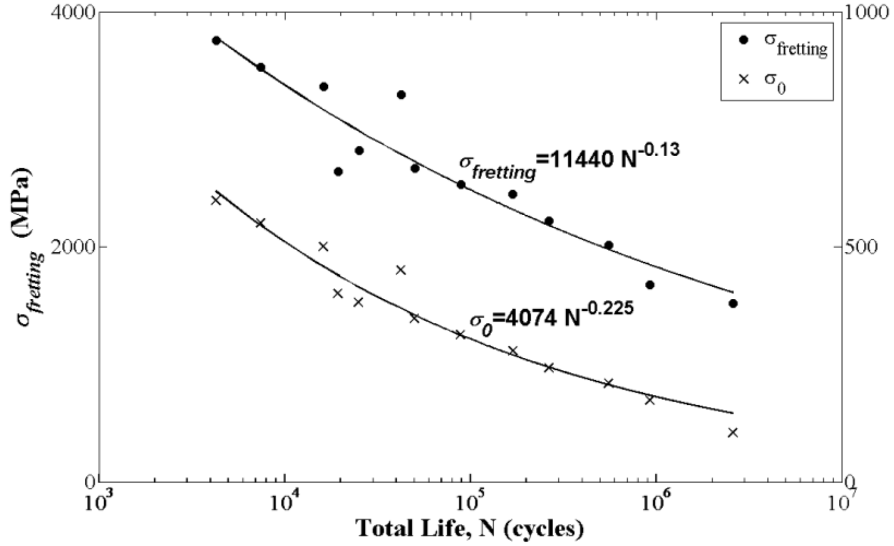

Figure 2.7: Fretting and bulk stress vs. life.

All the tests were continued until complete fracture or until the specimen could not carry the applied load. In every test, the crack nucleated at the edge of the contact on the actuator side of the specimen, (i.e. trailing edge of the contact). This is consistent with the observations in previous fretting fatigue experimental studies (Szolwinski and Farris [45]) and with the analytical solution for fretting stresses (Szolwinski and Farris [87]). Figure 2.8 illustrates the location of the crack with respect to the contact region for the test #9. In this case, the test was stopped just before the final fracture. As expected in fretting fatigue the crack initiated at an angle of 45° relative to the surface. Once the crack grows out of the fretting loading range, it turns nearly perpendicular to the contact surface. In this stage crack growth is driven by the bulk axial stresses. These observations are in agreement with the previous study [45]. A crack usually formed at both contact pads, but one became dominant by propagating faster than the other. The dominant crack could initiate at either fretting pad, so we can conclude that there was no loading imbalance on the specimen.

Top view of the fretting scar. Front view of the crack.

Figure 2.8: Fretting wear scar and crack for test #9. The arrow shows the loading direction. Left side was attached to the actuator while the right side was stationary.

Figure 2.9 shows the axial force measured by the upper and lower load cells, displacement of the actuator measured by the LVDT of the MTS and normal load applied to achieve the Hertzian contact pressure vs. time for the 1000th cycle of test #7 (Table Table 2.1). The normal force is stable until crack initiation. The tangential load, F_T, and displacement vary in phase with the applied lower force. The maximum displacement in the positive (tensile) direction increases as the crack grows in the specimen. This is because as the crack grows the effective area carrying the load decreases reducing the stiffness of the specimen, thus at the tensile peak axial load, the crack opens wider causing a larger deformation. When the crack has initiated there is significantly less material to support the same normal load. This causes plastic deformation near the contact region and the contact pads indent into the specimen. Since normal force is applied using a displacement-controlled mechanism, the normal force measured by the load cell decreases. The MTS machine was set up such that it would automatically stop if the normal load drops by 10% of the desired normal load. Both of these phenomena were used to estimate the crack initiation life. Earlier microscopic cracks did not affect the normal forces and displacement significantly, so crack initiation is defined as when a crack grows long enough to affect the measured normal force and displacement. Figure 2.10 shows the evolution of the displacement during a fretting test. The displacement starts to increase at around 34,000 cycles (estimated crack initiation life for this test). Table Table 2.1 shows that crack initiation life is around 90%

of the total fretting fatigue life for all the tests. Szolwinski and Farris [45], Namjoshi et al. [88] also made similar estimates.

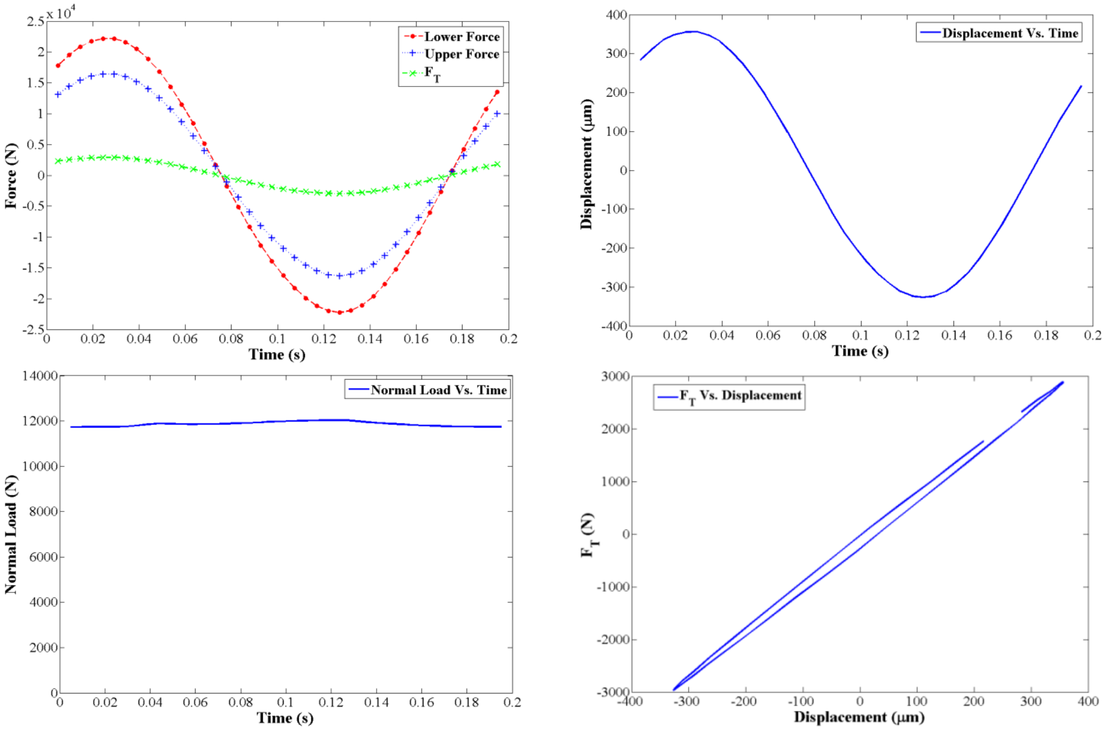

Figure 2.9: Measured experimental data for 1000th cycle for test #7.

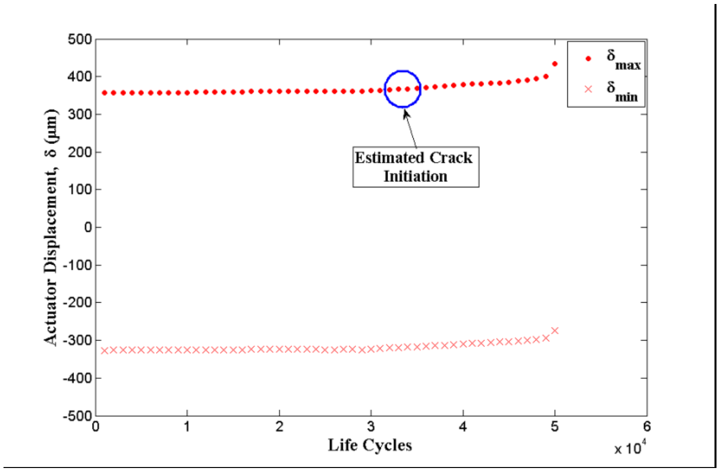

Figure 2.10: Displacement vs. Life cycles for test #7 and determination of estimated crack initiation.

For test condition 7, crack growth was monitored with a camera. Figure 2.11 shows pictures of the crack at various cycle numbers. A horizontal line was drawn along the length of the crack from start to the end (solid lines in Figure 2.11). Another horizontal line was drawn along the width of the specimen (dashed line in Figure 2.11). The length of the dashed line in the picture is 10 mm (the actual width of the specimen) and it is used to calibrate the solid line. The first visible crack initiated around 33,420 cycles with a length of 765 microns which is close to the estimated initiation life of 34,000 cycles. The experimental crack length vs. the number of elapsed life cycles is shown in Figure 2.12. The crack growth rate increases as the crack length increases as expected for fretting fatigue.

Table 2.1: Fretting fatigue experimental results.

	Bulk Stress (MPa)	Hertzian pressure (GPa)	F_N (N)	F_T (N)	F_T / F_N	Initiation Life (Cycles)	Total Life (Cycles)	$\sigma_{fretting}$ (MPa)
1	598	2.93	10313	4993	0.48	3785	4288	3756
2	550	2.97	11733	4905	0.42	6530	7472	3525
3	500	2.94	11027	4367	0.40	15000	16268	3366
4	450	3.00	11187	4192	0.37	40900	42470	3295
5	400	2.83	10360	2700	0.26	18170	19482	2638
6	382	2.99	11720	3242	0.28	23100	25130	2819
7	348	2.84	10525	2929	0.28	43620	50350	2668
8	313	2.89	10708	2633	0.25	83200	88880	2533
9	278	3.01	10447	2263	0.22	150000	169957	2448
10	243	2.88	10514	2064	0.20	239000	266000	2220
11	209	2.90	10727	1736	0.16	520000	557000	2016
12	174	2.99	11121	1170	0.11	861000	927000	1676
13	104	3.01	11307	1037	0.09	2532000	2594000	1516

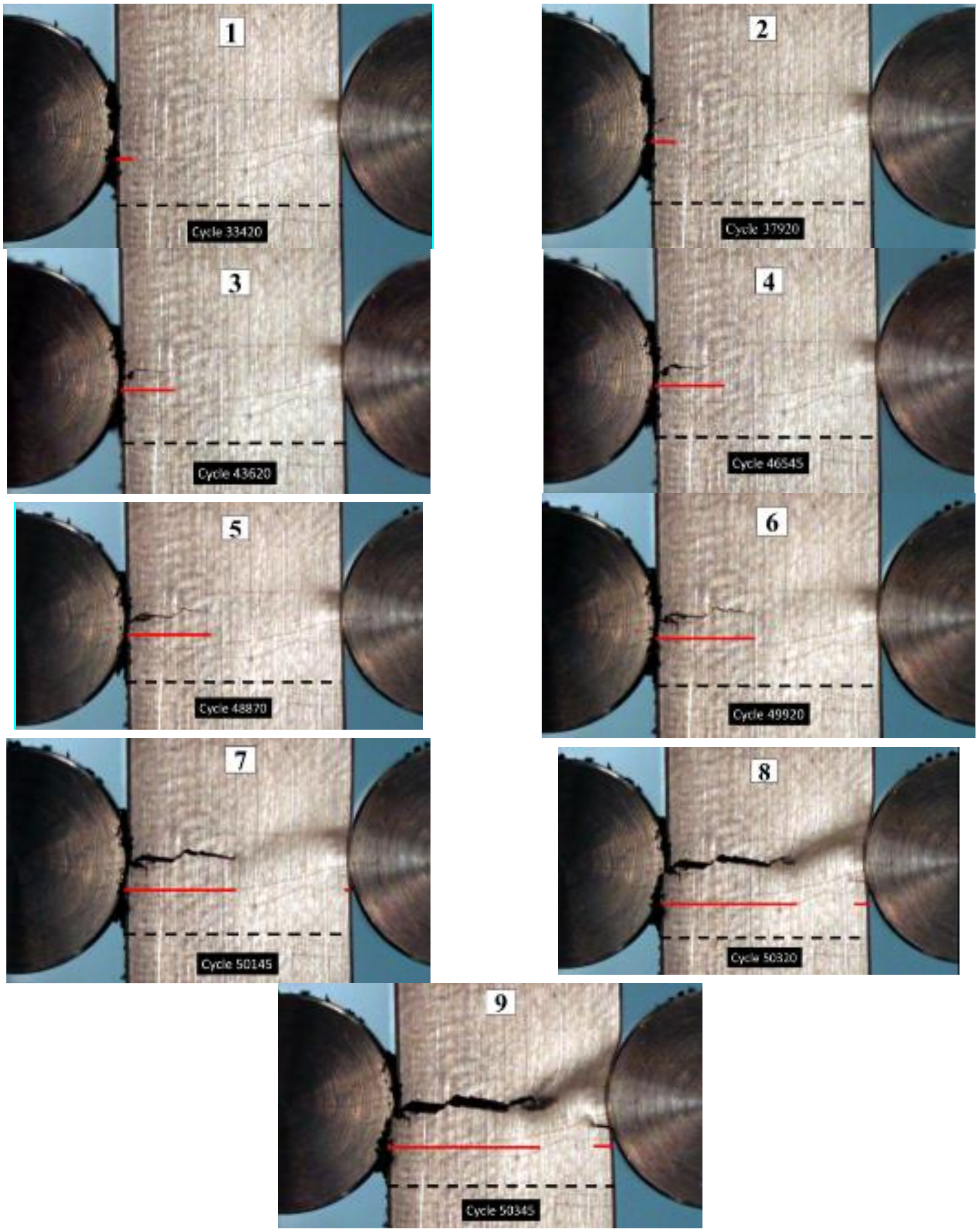

Figure 2.11: Pictures of the crack growth taken as the test is running for test #7 (Solid line denotes the effective crack length).

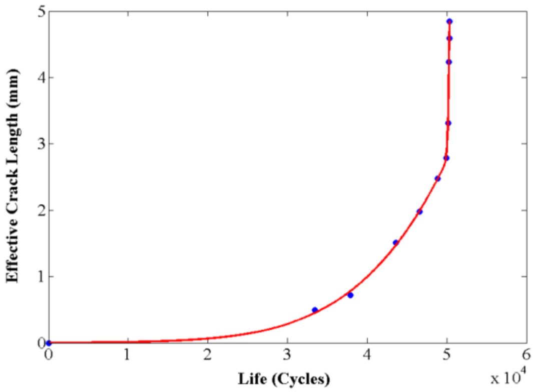

Figure 2.12: Crack length vs. life cycles for test #7 based on measured effective crack length using pictures in Figure 2.11.

2.3.2 Coefficient of Friction Measurement

Many researchers (Iyer and Mall [76], Lykins et al. [89]) have used the coefficient of friction (CoF) in the gross slip regime for numerical modelling of friction during fretting fatigue. In this study, a fretting test was performed in the gross slip regime to determine the CoF for the current experimental configuration. The specimen was only held with the bottom grip (the top end of specimen was free), but in other aspects the test was carried out similar to the fretting fatigue tests. Completely-reversed sinusoidal displacement at a frequency of 1 Hz was applied to the specimen. The force and the displacement of the actuator were recorded. In this configuration the force on the actuator and the friction force between the specimen and contact pads are the same. At the beginning of each test, displacement amplitude was increased until gross slip condition was achieved. Figure 2.13 illustrates the fretting loop at different cycles for contact stress of 585 MPa and displacement amplitude of 150 microns. It resembles the fretting loop commonly reported by many researchers (Mulvihill et al. [90]) for reciprocating sliding. It can be noted that the friction force varies during sliding and it increases more rapidly as sliding proceeds. Mulvihill et al. [90] have proposed that this variation is due to wear-scar interaction. Therefore the values of the friction force and normal force at the start of the gross slip were used to determine CoF. The experimental data and calculations required for coefficient of friction measurement are presented in Table Table 2.2. The CoF of 0.6 was used in this study.

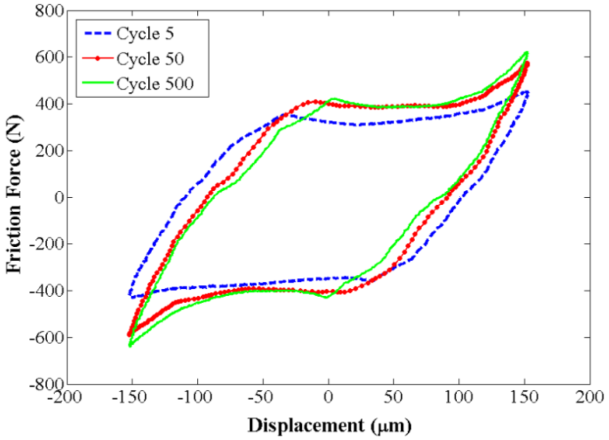

Figure 2.13: Fretting wear test at gross slip (displacement amplitude = 150 μm).

Table 2.2: Coefficient of friction calculations.

Disp. Amp. (μm)	Normal force (N)	Contact stress (MPa)	Friction force (N)	COF
150	392	567.2	216	0.6

2.4 Fretting Fatigue Damage Model

2.4.1 Finite Element Modeling

An ABAQUS finite element model was developed to investigate fretting fatigue and corroborate with the experimental results. The finite element model was used to determine the stress, strain and displacement distributions during a fretting cycle. The geometry of the contacting bodies with boundary and loading conditions applied are shown in Figure 2.14. The cylinder-on-flat contact configuration of the fretting fatigue test rig can be represented by a two-dimensional FE model. Making use of the symmetry of contact between the specimen and two pads, only one contact pad and half of the specimen are modeled under plane strain conditions. The theoretically infinite domain is truncated to fifteen and ten times the Hertzian half width (a) in the horizontal and vertical direction respectively. The domain was meshed with constant strain triangular elements and the "master-slave" algorithm was used for contact modeling in ABAQUS. The Lagrange Multiplier method was used for friction calculations using a friction coefficient of 0.60 as determined from the experiments. The left and the right edges of the upper body are constrained to zero displacement in x-direction (normal to the surface). This boundary condition assumes the infinite stiffness of the test fixture holding the contact pads. The bottom edge of the lower body is constrained in the y-direction (perpendicular to the surface). This boundary condition corresponds to the symmetry of the experimental domain. The loads are applied to the model in two steps. The uniform pressure corresponding to the normal load (F_N) is applied on the top surface of the upper body. In the second step, one cycle of a sinusoidal bulk stress is applied with the amplitude, (σ_0) selected to match the experimental loading. The approach described by Talemi and Wahab [91] was used to model the tangential force (F_T) measured during the experiments. The sinusoidal reaction stress with amplitude "$\sigma_{reaction}$" is applied on the left edge of the lower body in phase with the bulk stress such that the frictional force generated between the lower and upper body would match the experimental tangential force. The experimental results illustrated in Figure 2.15 show that the ratio of tangential force to normal force (F_T/F_N) varies linearly with the applied bulk stress (σ_0). The numerical reaction stress was calculated based on this relationship and the applied loads:

$$\sigma_{reaction} = \sigma_o - \frac{\left(\frac{F_T}{F_N}\right)_{line\,fit} * F_N}{A_s} \tag{2.3}$$

where, A_s is the cross-sectional area of the flat specimen geometry used in the model as shown in the Figure 2.14.

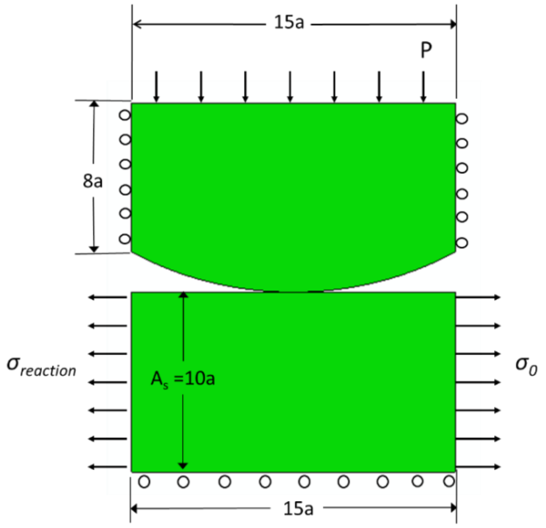

Figure 2.14: The geometry of the two-dimensional finite element model showing the applied boundary and loading conditions (a = 365 μm).

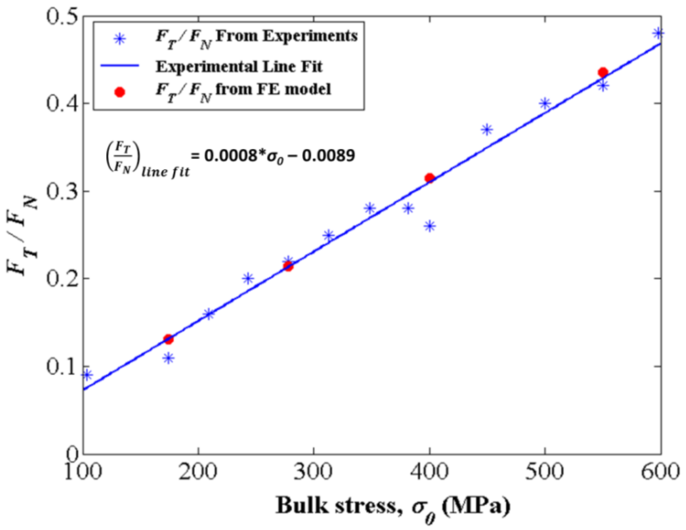

Figure 2.15: Comparison of F_T/F_N obtained from experiments and FE model.

2.4.2 Voronoi Tessellation

A single phase polycrystalline material consists of micron level grains of random size and shape which can be represented by Voronoi tessellation to a good degree of accuracy as shown by Mücklich et al. [92], Espinosa and Zavattieri [93] and Jalalahmadi and Sadeghi [29]. In the present study geometric disorder and randomness of material microstructure topology is simulated using Voronoi tessellation to account for the variability in fretting fatigue life. The Voronoi cells and their boundaries resulting from a random tessellation represent the grains and grain boundaries respectively in the real microstructure. This approach has been used in different numerical models to investigate the scatter in uniaxial fatigue (Warhadpande et al. [94], Bomidi et al. [95]), rolling contact fatigue (Raje et al. [96], Jalalahmadi and Sadeghi [30], Slack and Sadeghi [97]) and in fretting fatigue (Slack et al. [85]). In this approach, a set of seed points are randomly placed in the domain. Then, the domain was divided into regions around each seed point such that each region consists of the points which are closer to the seed point than any other seed point in the domain. The set of points which are equally close to more than one seed point form the boundary between the regions corresponding to those seed points. This process results in the domain divided into convex polygons known as Voronoi cells. The generated cells have different number of sides with a median of 6. By distributing the seed points randomly in the domain, distinct simulation domains can be generated. The minimum distance between two seed points can be specified to match the grain size of the relevant material. The random Voronoi microstructure was generated in MATLAB and the cells were meshed with constant strain triangular elements using Triangle software [98]. Figure 2.16 shows a randomly generated domain with red lines denoting the boundaries of the Voronoi cells (grains). The randomly located and oriented Voronoi cell boundaries are considered to be "critical planes" on which the damage occurs. From our experiments, it is clear that only the tensile specimen become damaged during the fretting fatigue and damage near the contact region is the most significant for fretting fatigue life. Therefore, in order to save the computation time, Voronoi tessellation is used only for the tensile specimen in the contact region. The rest of the domain is meshed using Triangle software [98].

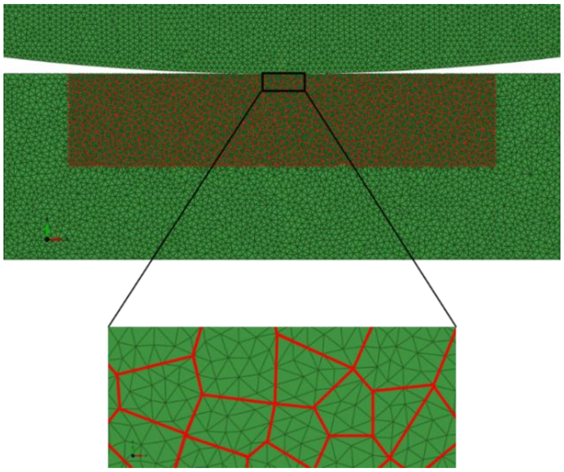

Figure 2.16: Finite element mesh using the random Voronoi cells at the contact region. The red lines represent the voronoi cell boundaries.

2.4.3 Model Validation

In order to validate the finite element model developed for this investigation, the contact half width and peak Hertzian pressure obtained from FE model were compared to analytical solution. The material properties and loading conditions used in the simulations are listed in the Tables Table 2.3 and Table 2.4, respectively. Both bodies were assumed to be elastic. According to Hertzian theory, contact half width and maximum contact pressure (P_h) for the loading conditions used in this analysis are 365 μm and 3.0 GPa. The finite element model used in this analysis resulted in half contact width of 368 microns and P_h=3.02 GPa, an error of about 1%. The tangential load (F_T) was calculated from the force on the left and right edges of the upper body (contact pad) at the tensile peak of the bulk stress cycle.

This reaction force is equal to frictional force between the specimen and contact pad. Figure 2.15 illustrates the comparison between F_T/F_N calculated from the model and the results obtained from the experiments for different values of bulk stresses. This figure demonstrates that there is good correlation between FE model and experimental results; this indicates that FE model obeys the force equilibrium and is working as expected. Further, to validate the stress distribution obtained from the FE model, shear stress distribution on the contact surface was compared with the analytical solution reported in Hills and Nowell [99]. Figure 2.17 depicts the shear stress distribution for loading condition 3 in Table Table 2.4 obtained from the current FE model and the analytical solution. Szolwinski and Farris [87] have used Westergaard stress functions to provide the analytical solution for subsurface stresses due to fretting loading (i.e. normal load, F_N and tangential load, F_T) without considering the bulk stress. The analytical solution for distribution of the tangential stress (σ_{11}) just below the surface was obtained for loading condition 3 in Table Table 2.4 by adding the bulk stress to the stress distribution calculated using the analytical solution given in [87]. Figure 2.17 compares the normalized surface tangential stress obtained from the analytical solution and our finite element model. The shear and tangential stress distribution from FE model correlate well with the analytical solution.

Table 2.3: Material properties used in the analysis.

Material 1 (tensile specimen)	AISI 4140
Undamaged elasticity modulus for material 1, E_1	205 GPa
Poisson’s ratio for material 1, v_1	0.29
Material 2 (cylindrical contact cad)	Ti-6Al-4V
Elasticity modulus for material 2, E_2	113.8 GPa
Poisson’s ratio for material 2, v_2	0.342
Coefficient of friction	0.6
Damage rate law coefficient for material 1, σ_r	16061 MPa
Damage rate law exponent for material 1, m	7.5
Critical damage for material 1, D_{crit}	0.12

Table 2.4: Loading conditions and predicted Weibull slope and strength parameters for fatigue damage model.

Loading condition	**Bulk stress σ_0 (MPa)**	**$\sigma_{reaction}$ (MPa)**	**F_T/F_N**	**P_h (GPa)**	**$\sigma_{fretting}$ (MPa)**	**Weibull slope**	**Weibull strength (cycles)**
1	174	113	0.13	3	1850	3.14	1,084,200
2	278	178	0.21	3	2426	3.36	140,810
3	400	253	0.31	3	2991	3.92	25,756
4	550	347	0.43	3	3602	5.96	6,048

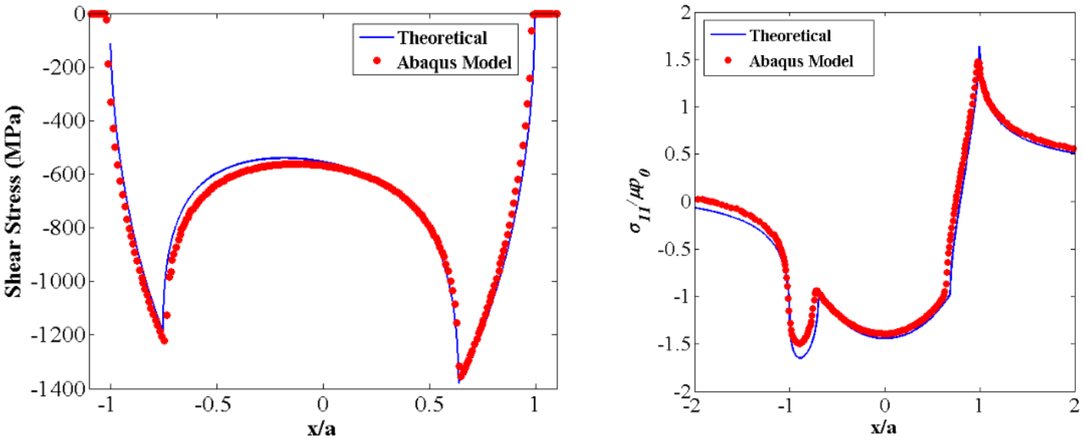

Figure 2.17: Comparison of shear stress distribution and normalized tangential stress, $\sigma_{11}/\mu p_0$ on the contact surface at the positive peak of the fretting cycle obtained using FE model and analytical solution for loading condition 3 in Table 4.

2.4.4 Fatigue Damage Model

Fatigue damage is associated with the progressive material deterioration due to the initiation and growth of micro-cracks and voids. Damage mechanics treats these microscopic failure mechanisms in an empirical fashion. Material degradation (damage) is recognized by introducing a thermodynamic state variable tensor *D* into the constitutive relations. This damage variable accounts for the micro-cracks and cavities in the representative volume element (RVE) of the material. If it is assumed that Poisson's ratio remains constant and damage is isotropic, *D* reduces to a scalar. *D* is defined by Kachanov [28] as,

$$D = \frac{A - \tilde{A}}{A} \tag{2.4}$$

Here, A is the apparent (undamaged) area and $\tilde{A}$ is the effective (actual) area which carries the load. This changes the effective stress at the representative volume element. Effective stress then becomes,

$$\tilde{\sigma} = \frac{F}{\tilde{A}} = \frac{\sigma}{(1-D)} \tag{2.5}$$

The value of D for undamaged material is 0. Applying Hooke's law, if E is the elasticity modulus for the undamaged material, elastic strain in the material is,

$$\varepsilon = \frac{\tilde{\sigma}}{E} = \frac{\sigma}{E(1-D)} \tag{2.6}$$

Defining elastic modulus of the damaged element to be,

$$\tilde{E} = E(1-D) \tag{2.7}$$

We can say that increase in the internal damage as the fatigue cycles progress, manifests as the reduction in the modulus of elasticity. Rearranging this equation, the damage variable can be calculated by

$$D = 1 - \frac{\tilde{E}}{E} \tag{2.8}$$

At rupture the crack occupies the entire surface of the RVE which corresponds to D=1. But in many cases, rupture occurs suddenly after the crack occupies a certain area in the RVE due to the decohesion of atoms in the remaining resisting area [100]. The value of D at the final rupture is defined as the critical value of damage variable D_{crit}, which depends upon the material and loading conditions. Equation (2.8) can be used to measure the value of the damage variable at rupture by variation of elasticity modulus test.

Many different constitutive equations for the evolution of damage variable at a material point have been formulated according to the damage mechanism for the phenomenon of interest. Lemaitre [100] has reviewed the different damage mechanisms and equations. For high cycle fatigue with brittle damage mechanism, the model proposed by Xiao et al. [101] is commonly used in the fatigue literature (for example, Warhadpande et. al. [94]).

$$\frac{dD}{dN} = \left[\frac{\Delta\sigma}{\sigma_r(1-D)}\right]^m \tag{2.9}$$

Here, $\Delta\sigma$ is the stress range that causes the damage, N is the cycle number, σ_r and m are the fatigue damage properties of the material undergoing cyclic loading. The value of σ_r, which is usually a function of mean stress, characterizes the ability of the material to resist accumulation of fatigue damage. The fatigue damage model which used damage mechanics for modeling fatigue was developed and used in investigations of various fatigue phenomena such as rolling contact fatigue by Raje et al. [96], Jalalahmadi and Sadeghi [30], Slack and Sadeghi [97] and uniaxial fatigue by Warhadpande et al. [94]. A similar approach has been used in this analysis for modeling fretting fatigue as described below.

In fatigue damage model, damage coupled material constitutive equations and damage evolution relations are solved simultaneously for each element. Therefore, after every stress cycle, stress-strain relationships have to be evaluated and accordingly damage and elastic modulus for each element need to be updated until final failure. However, it is computationally impractical to employ this iterative method after every loading cycle. Therefore, the standard 'jump-in cycles' approach developed by Lemaitre [100] is used here to make the solution computationally feasible. In this algorithm the stress response is assumed to remain unaltered over a finite number of cycles, ΔN^i, in a block i. During this block of cycles, damage for each element is also assumed to remain constant. Thus, damage evolution is piecewise linear with respect to the block of cycles. A constant damage increment ΔD over that number of cycles is prescribed for the element which has largest damage evolution rate. Current stress field in the domain is found for each block of cycles by using the material constitutive relations and damage obtained from the previous block of cycles. The current stress field is then used in the damage evolution law to update the damage for each element and find number of cycle in the current block.

In order to introduce randomness into the life predictions, the alternating normal stress (σ_{n_a}) acting along the Voronoi grain boundary during the fretting cycle is assumed to cause damage. The Voronoi cells are divided into triangles by connecting pairs of adjacent Voronoi edge vertices to the centroid of their Voronoi cell; these will be referred to as 'Voronoi triangles'. σ_{n_a} for a Voronoi triangular element is given by;

$$\sigma_{n_a} = \frac{\sigma_{n_{max}} - \sigma_{n_{min}}}{2} \tag{2.10}$$

$\sigma_{n_{max}}$ and $\sigma_{n_{min}}$ are the maximum and the minimum normal stresses acting on the Voronoi grain boundary during a fretting cycle. The values of the stress used to calculate the normal stresses (σ_n) for a Voronoi triangle are taken from the finite element model at the centroid of the Voronoi Triangle. Figure 2.18 depicts a single Voronoi cell divided into Voronoi Triangles and normal stresses along the grain boundaries.

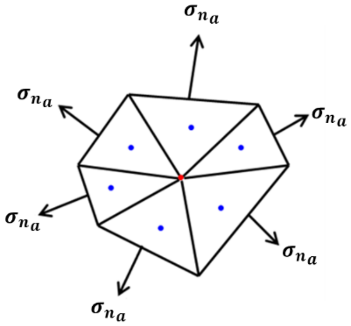

Figure 2.18: Voronoi grain divided into Voronoi Triangles and stresses resolved along the grain boundaries. The red dot denotes the centroid of the Voronoi grain while blue dots denote the centroids of the Voronoi Triangles.

The step by step procedure for damage evolution is given below:

(1) *The material domain is assumed to contain no initial flaw. Hence, the initial damage for each Voronoi Triangle is set to 0 and pristine elasticity modulus is assigned to each of the Voronoi Triangles.*

$$D_j^0 = 0, \qquad E_j^0 = E \qquad j = 1 \ldots n \; (Voronoi\ Triangles) \tag{2.11}$$

(2) *The stress field for a single fretting cycle is evaluated using ABAQUS for the current iteration, i. From this stress field, the alternating normal stress, σ_{n_a}, for Voronoi triangles is calculated. The damage evolution rate for each Voronoi Triangle j is calculated using the current alternating normal stress and state of damage for that Triangle,*

$$\left(\frac{dD}{dN}\right)_j^i = \left[\frac{\left(\sigma_{n_a}\right)_j^i}{\sigma_R(1 - D_j^i)}\right]^m \tag{2.12}$$

(3) *The maximum damage evolution rate in the domain is found. The number of cycles required for the damage of the Voronoi Triangle with maximum damage evolution rate to increase by ΔD is calculated,*

$$\Delta N^i = \frac{\Delta D}{\left(\frac{dD}{dN}\right)_{crit}^i} \tag{2.13}$$

where

$$\left(\frac{dD}{dN}\right)_{crit}^i = \underset{i}{Max}\left|\left(\frac{dD}{dN}\right)_j^i\right| \tag{2.14}$$

(4) *The total number of cycles (N) elapsed, damage and elasticity modulus for each Voronoi Triangle are updated.*

$$N^{i+1} = N^i + \Delta N^i \tag{2.15}$$

$$D_j^{i+1} = D_j^i + \left(\frac{dD}{dN}\right)_j^i \Delta N^i \tag{2.16}$$

$$E_k^{i+1} = E(1 - D_k^{i+1}) \tag{2.17}$$

(5) *This procedure is repeated until accumulated damage for any Voronoi Triangle reaches the critical value of damage* D_{crit}. *Therefore, the total number of cycles (N) at this stage represents the crack initiation life. Experimental observations show that crack initiation constitutes the majority of the total fretting fatigue life, so N is assumed to be the total fretting fatigue life.*

2.5 Analytical Results

2.5.1 Identification of Material Dependent Fatigue Damage Properties

As described earlier, the tensile specimen undergoes fatigue damage during the fretting fatigue and most of the fatigue life is spent for the crack initiation near the contact region. Therefore, in this study damage is evaluated only for the contact region of the tensile specimen. In this section, material dependent properties needed for the fatigue damage model are evaluated for AISI 4140, the material of the tensile specimen in our fretting experiments.

- **Method of Variation of Elasticity Modulus:** The critical damage at fracture can be found by measuring the reduction in the elasticity modulus of the material during a test. This procedure is described as the method of variation of elasticity modulus by Lemaitre [100]. Accurate strain measurements are important for these calculations so a strain gage was installed on in the constant cross sectional area region of the specimen. Figure 2.19 shows the mounted strain gauge. Test was performed in the displacement-controlled condition. In each cycle, displacement was gradually increased until plastic deformation occurs. Then, the displacement was decreased until the force (i.e. stress in the specimen) returns to zero. In the next cycle, displacement was increased further to create incrementally more plastic deformation. This procedure was repeated until the fracture. Figure 2.20 depicts the stress vs. strain plot for each cycle of the test. Elasticity modulus was calculated from the slope of the unloading curve. As expected, the elasticity modulus decreases as the plastic deformation increases (i.e. specimen is getting more damaged). Table Table 2.5 shows the decrease in the elasticity modulus as the damage increases. The critical damage value or damage at the time of fracture is 0.12. Warhadpande et al. [94] found the critical damage value of AISI 4142 to be was 0.11.

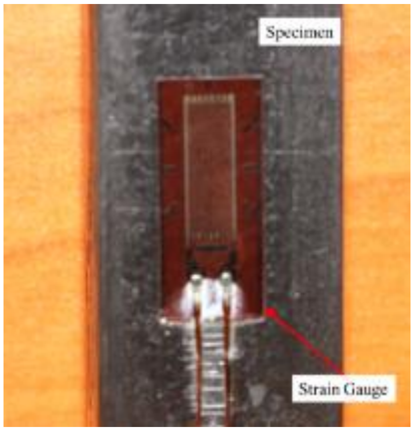

Figure 2.19: Strain gauge mounted on the tensile specimen for ‘Variation of Elasticity Modulus Test’.

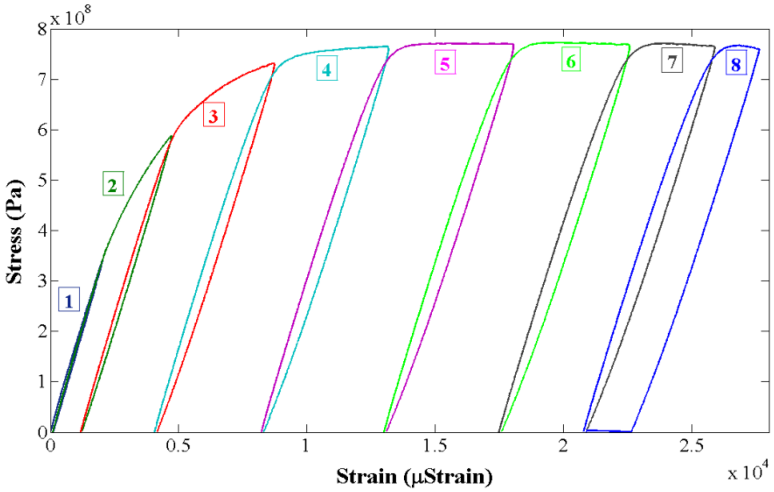

Figure 2.20: Stress vs. strain plot at various cycles for the variation of elasticity modulus test.

Table 2.5: Variation of Elasticity Modulus.

Cycle No.	*E (1-D)* (GPa)	*D*
1	176.0	0
2	167.1	0.051
3	160.6	0.088
4	157.3	0.106
5	155.8	0.115
6	155.2	0.119
7	154.5	0.123
8	154.5	0.122

- **Evaluation of resistance stress (σ_r) and damage exponent (*m*):** Figure 2.17 illustrates that there is a large stress concentration at the trailing edge of the contact (x/a ≈ 1) compared to the bulk stress (x/a > 1.5). Szolwinski and Farris [45] hypothesized that the peak in the tensile stress at the trailing edge ($\sigma_{fretting}$) drives crack initiation in fretting fatigue. In this analysis the critical stress component causing the damage is the fretting stress ($\sigma_{fretting}$) as defined in Equation (2.2). The damage evolution equation for fretting fatigue becomes

$$\frac{dD}{dN} = \left[\frac{\sigma_{fretting}}{\sigma_R(1-D)}\right]^m \tag{2.18}$$

The damage parameters σ_r and m were evaluated using the maximum fretting stress $\sigma_{fretting}$ and fretting fatigue life data from experiments. Figure 2.7 shows the plot of $\sigma_{fretting}$ against experimental total life. Applying a power law curve fit of the following form to the data:

$$\sigma_{fretting} = AN^b \tag{2.19}$$

Where

$$A = 11440\ MPa,\ \ b = -0.13 \tag{2.20}$$

Assuming that maximum fretting stress ($\sigma_{fretting}$) in the damage evolution rate equation (Equation (2.18)) is constant, we can separate the two variables *D* and *N*. Simple integration from undamaged state (*N*=0 and *D*=0) to fully damaged state ($N = N_f$ and $D = D_{crit}$) yields,

$$\int_0^{N_f} dN = \int_0^{D_{crit}} \left\{\frac{\sigma_R(1-D)}{\sigma_{fretting}}\right\}^m dD \tag{2.21}$$

or

$$N_f = \left(\frac{\sigma_R}{\sigma_{fretting}}\right)^m \left[\frac{1}{m+1} - \frac{(1-D_{crit})^{m+1}}{m+1}\right] \tag{2.22}$$

Rearranging this equation,

$$\sigma_{fretting} = \sigma_R \left[\frac{1}{m+1} - \frac{(1-D_{crit})^{m+1}}{m+1}\right]^{\frac{1}{m}} N_f^{-\frac{1}{m}} \tag{2.23}$$

Since Eqs. (2.19) and (2.23) are equivalent, comparing the exponents and coefficients gives

$$m = -\frac{1}{b}, \qquad \sigma_R = A\left[\frac{1}{-\frac{1}{b}+1} - \frac{(1-D_{crit})^{-\frac{1}{b}+1}}{-\frac{1}{b}+1}\right]^b \tag{2.24}$$

Substitution of the values for A and b results in

$$m = 7.5, \qquad \sigma_R = 16061\ MPa \tag{2.25}$$

2.5.2 Fretting Fatigue Life Predictions

After obtaining the material dependent parameters required for the fatigue damage model, 30 unique material domains were generated to analyze the scatter in the fretting fatigue lives. Voronoi cells with an average size of 10 microns were used to model the microstructural grains of AISI 4140. For each loading condition listed in Table Table 2.4, the fatigue damage model was run for all 30 randomly generated microstructure domains until the damage in one Voronoi Triangle in the domain reaches the critical value D_{crit}. Damage increment, ΔD of 0.02 was used in the jump-in cycle algorithm. The randomness in the microstructure topology of the domains causes variation in the magnitude of the largest alternating normal stress, σ_{n_a} experienced in each domain. However, for all the domains the element experiencing the largest alternating normal stress was located near the trailing edge of the contact. The fatigue life obtained from the model for each domain vs. maximum fretting stress ($\sigma_{fretting}$) is shown in Figure 2.21. The power law fit for the experimental data is also plotted on this figure. The fretting fatigue lives obtained from the fatigue damage model and their scatter follow the experimental data closely. Degree of scatter is quantified using two-parameter Weibull probability distribution. Weibull strength parameter indicates the number of cycles for which the probability of failure is 63.2%. Weibull slope denotes the amount of scatter present in the data. Smaller Weibull slopes indicate that there is more scatter in the data. Weibull plot is presented for all 4 loading conditions in Figure 2.22. Weibull slope and strength cycles obtained from the current analysis are also listed in Table Table 2.4. It can be observed that the scatter in the fretting fatigue lives increases with decreasing the bulk applied stress for the same contact pressure. As expected, the probability of survival also increases with decreasing bulk stress as shown by the variation of Weibull strength cycles.

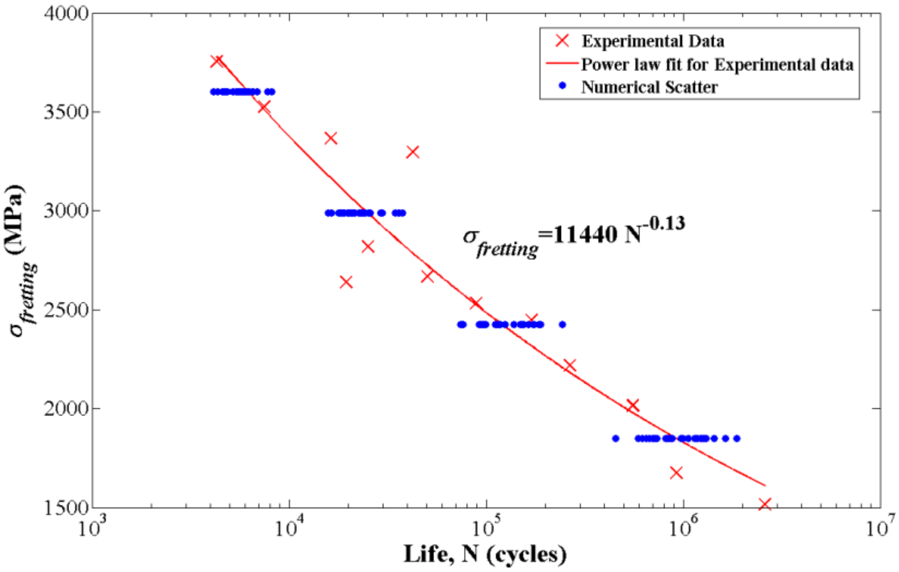

Figure 2.21: Comparison between the fretting fatigue lives obtained from the fatigue damage model for different loading conditions and experimental results.

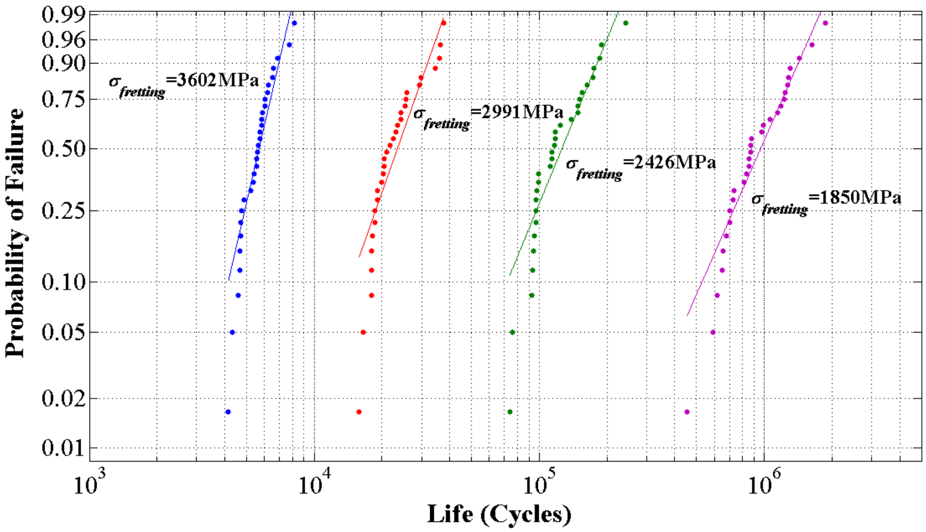

Figure 2.22: Weibull probability plot for fretting fatigue lives for different loading conditions.

2.6 Summary and Conclusions

This chapter presented the results of experimental investigation and a fatigue damage model for fretting fatigue. For the experimental investigation, a fretting fixture was designed, built and used with an MTS 810 machine simulating the fretting fatigue in a cylinder-on-flat configuration. For a fixed contact pressure, the fretting fatigue life decreased with increasing bulk stress. The observed crack nucleation at the trailing edge of the contact was consistent with the previous experimental investigations. In the analytical part of this work, a fatigue damage finite element model was proposed to replicate the fretting fatigue experiments and numerically estimate the fretting fatigue life. The model was tested with the same loading conditions as the experiments. The fretting fatigue lives predicted by the fatigue damage model are in good agreement with the experimental results. The fatigue damage model was further used to study the variability occurring due to the randomness in material microstructure. The predicted fatigue life data displayed a larger degree of scatter for the lower bulk stress when the contact pressure is fixed.

3. SUB-SURFACE INITIATED SPALLING IN LARGE ROLLING CONTACTS

3.1 Introduction

In REBs, the Hertzian loading results in a complex multi-axial stress distribution in the contact region (Hertz [102]). Several factors including material properties, surface profile, size effects, residual stresses, nonmetallic inclusions etc. need to be taken into account when investigating RCF ([103]–[106]). Several empirical and numerical models have been proposed to estimate the fatigue lives of REBs. Predictive methods described by Lundberg and Palmgren [11], Ioannides and Harris [12] are widely used as the basis for bearing life algorithms. A comprehensive review of RCF models has been compiled by Sadeghi, et al. [7]. An alternative modeling approach developed by [27-30] seeks to overcome the limitations of the previous models by incorporating microstructural features in fatigue life simulation. This approach utilizes Voronoi tessellations to account for geometric disorder and the randomness in the material microstructure topology. Unlike previous numerical models, this model captures both the initiation and propagation phases of RCF. Furthermore, it does not rely on the Weibull regression parameters obtained from full-scale bearing fatigue test data. Espinosa and Zavattieri [93]; Jalalahmadi and Sadeghi [29] showed that Voronoi tessellations represent the grain structure of the polycrystalline material and can be used to simulate its effect on the fatigue life. Since bearing materials are polycrystalline in nature, many researchers [[27], [30], [32], [97], [107]] have applied this approach in conjunction with continuum damage mechanics (Lemaitre [100]) to simulate rolling contact fatigue. They assumed a shear driven intergranular failure mechanism and used the model to obtain life estimates, spalling patterns and the scatter in the RCF lives.

Typically, these models deal with experimental scale bearings with half-contact width, *b*, around 100 μm. But many applications such as wind turbine have large bearings with half-contact widths in the order of 1 mm or more. Kim, et al. [108] studied the radial cracking in the large bearings subjected to significant tensile hoop stress. However, there are not many studies which investigate subsurface initiated spalling and try to predict fatigue lives for large bearings. The damage mechanics based Voronoi model [97] described earlier can be used to model large bearings but the computational expense renders it impractical. Therefore, this investigation presents a new innovative approach in which efficient computational strategies are implemented to make the RCF model tractable to study bearings with large half-contact width. The internal topology of the material microstructure is modeled using randomly generated Voronoi cells which represent grains in the material microstructure. However, simulation time for a contact rolling pass is significantly reduced by using the Delaunay triangle [98] approach to generate an FE mesh. A MATLAB code is used to transfer the stresses from Delaunay mesh to Voronoi cells. Material degradation due to fatigue loading is accounted using the continuum damage mechanics. Simulation time for an RCF investigation with the new microstructure model is further expedited by an integration algorithm that considers the strain energy released through damage formation and growth. The model uses a ‘kill element’ approach similar to Slack and Sadeghi [97] to simulate the initiation and propagation of fatigue damage. A remeshing tool was developed to refine the Delaunay mesh around the damaged element to capture accurate stress field. The results of the model are compared with the previous model predictions for validation. The model was then employed for large bearings with half-contact width of 200 μm, 400 μm and 1000 μm. The spalling patterns and the topological effect on fatigue life scatter obtained from the model show good agreement with experimental observations. The ratio of L_{10} lives for different half-contact widths compared well with the basic life rating for radial roller bearing as per ISO 281. Furthermore, the effect of random distribution of initial defects on the fatigue lives is also investigated. It was found that the larger bearings have lesser L_{10} lives if the density of initial defects is assumed to be the same.

3.2 Modeling Approach

3.2.1 Microstructure Topology Model

A polycrystalline material contains micron level grains of random sizes and shapes. Ito and Fuller [109] showed that these grains can be geometrically represented by Voronoi tessellation to a good degree of accuracy. Geometric representation of material microstructure by Voronoi tessellation has been widely employed in numerical investigations to account for the variability in fatigue life e.g. some researchers [94], [95] have adapted it for studying uniaxial fatigue; others [30], [31], [97] have used it for investigating RCF and Slack, et al. [85] applied it for analyzing fretting fatigue. In the Voronoi tessellation approach, a set of seed points are randomly placed in the Euclidian space. Around every seed point, a region is formed with the criterion that every point in a particular region is closer to the seed point of that region than any other seed point in the space. The set of points which are equidistant to two or more seed points define the boundary between the regions formed by corresponding seed points. This process divides the space into convex polygons called as Voronoi cells. The Voronoi cells have variable orientations and variable number of sides with a median of 6. Mucklich, et al. [92] illustrated that the real microstructure of a single-phase polycrystalline material and the one generated using Voronoi tessellation quantitatively correlate well. Further, the formation of Voronoi tessellation is similar to the process of solidification in the polycrystalline material. The seed points represent the various crystal nucleation sites within a liquefied material. As the material cools, the crystals grow by adding surrounding liquid atoms to the solidified crystal structure until the extremities of adjacent crystals impinge on one another [110]. Therefore, it can be assumed that the Voronoi cell and their boundaries represent the grains and grain boundaries, respectively. In this investigation, the minimum distance between two seed points was specified to match the measured average grain size in the bearing steel. It was hypothesized that fatigue life scatter is mainly caused by the randomness of the microstructure in the representative volume element (RVE), identified as the critically stressed region during a rolling pass. The dimensions for the microstructure topology region for line contact are given in Table 3.1 in terms of half-contact width, *b*. Distinct simulation domains were generated by randomly distributing the seed points in the RVE. Figure 3.1 depicts a random material microstructure generated using a Voronoi tessellation.

Table 3.1: Model dimensions.

Dimension	**Microstructure topology region**	**Simulation domain**
X (half-contact width)	*(-2b, 2b)*	*(-5b, 5b)*
Y (half-contact width)	*(0, -1b)*	*(0, -7b)*

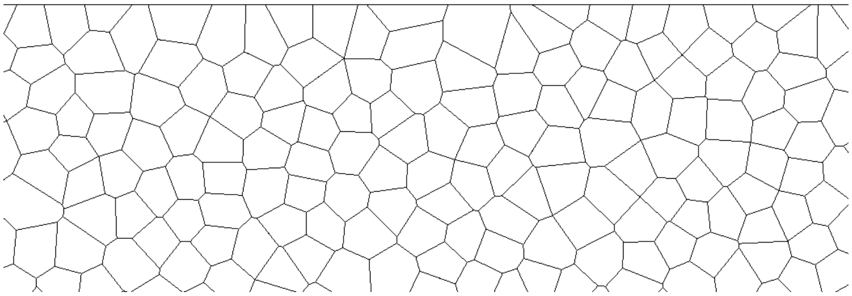

Figure 3.1: Random material microstructure generated using a Voronoi tessellation. The Voronoi cell boundaries represent the weak planes in the material microstructure.

3.2.2 Fatigue Damage Model

Material deterioration due to fatigue cycles manifests through the initiation and propagation of micro cracks and voids. The theory of continuum damage mechanics provides a framework to model these microscopic mechanisms of fatigue failure in an empirical fashion ([28], [111]). The effect of fatigue damage on the homogenized material response is captured by introducing a thermodynamic state variable, D into the material constitutive relations in the following form:

$$\sigma_{ij} = C_{ijkl}(I_{klmn} - D_{klmn})\epsilon_{mn} \tag{3.1}$$

Where, σ_{ij}, C_{ijkl}, D_{klmn}, ε_{mn} corresponds to the stress, stiffness, damage and strain tensors. However, assuming the isotropic damage and neglecting the effect of Poison's ratio on damage, the damage tensor reduces to a scalar quantity as follows:

$$\sigma = E(1 - D)\varepsilon \tag{3.2}$$

Where, E is the elasticity modulus for the undamaged material. D can range from *0* to *1* where a value of *0* means an undamaged or pristine material and *1* corresponds to a completely damaged material.

The effective elastic modulus of the damaged element is defined to be:

$$\tilde{E} = E(1 - D) \tag{3.3}$$

As the fatigue cycles progress, the internal damage manifests as the reduction in the effective modulus of elasticity.

The evolution of damage variable at a material point has been formulated by a rate law according to the damage mechanism for the phenomenon in interest. As mentioned in the Introduction section, reversal in shear stress is considered to be the critical stress component responsible for causing RCF (Littman [2], Lundberg and Palmgren [11].

Further, the presence of compressive hydrostatic component in the stress field makes the mode II crack growth dominate. To account for the randomness in material microstructure and introduce variability in fatigue life predictions of the model, it is assumed that grain boundaries constitute the "critical planes" along which the fatigue damage advances. Consequently, the action of the maximum shear stress reversal $\Delta\tau_{critical}$ along the Voronoi grain boundary is considered to be the damage causing stress (Figure 3.2). The damage evolution law for modeling RCF therefore becomes ([27], [30], [97], [107]) -

$$\frac{dD}{dN} = \left[\frac{\Delta\tau_{critical}}{\tau_r(1-D)}\right]^m \tag{3.4}$$

The fatigue damage parameters, τ_r and m are material properties that need to be determined experimentally. The value of τ_r, which is usually a function of mean stress, characterizes the ability of the material to resist accumulation of fatigue damage (Bolotin and Belousov [112]). However, during the rolling pass the shear stress undergoes a complete reversal so the mean stress is equal to 0. It was hypothesized that failure mechanism for torsional fatigue and rolling contact fatigue are equivalent, because, the mechanism for damage accumulation is similar for both types of fatigue phenomena. Then, damage parameters can be extracted from the stress-life (SN) relationship for the material in torsional fatigue [97]. Figure 3.3 illustrates the torsion SN curve for AISI 52100 bearing steel [113]. The results from [113] were used to obtain τ_r and m [97] -

$$m = 10.1, \qquad \tau_r = 6113\ MPa \tag{3.5}$$

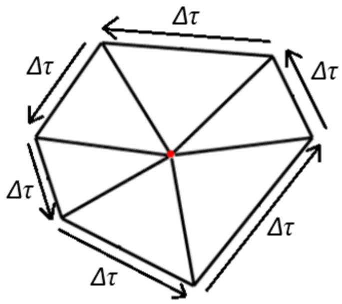

Figure 3.2: Voronoi cell divided into Voronoi elements and stresses resolved along the grain boundaries.

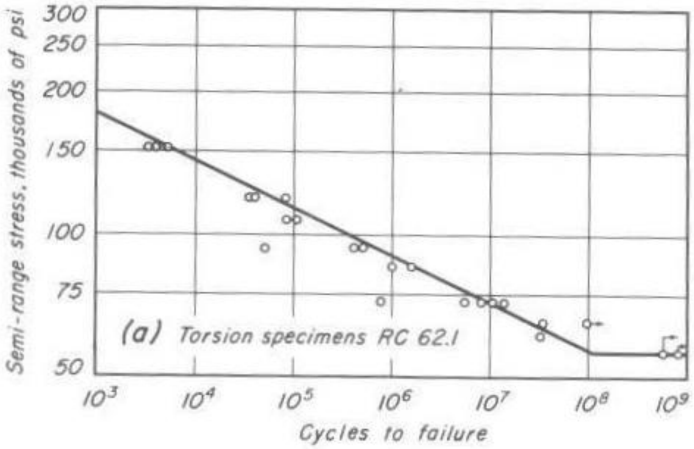

Figure 3.3: S-N curve for bearing steel AISI 52100 in completely reversed torsional fatigue (Styri [113]).

3.2.3 RCF Simulation

A finite element model was developed to simulate a rolling pass for a cylindrical roller bearing. The line contact between the roller and the raceway is modeled as a Hertzian loading on a semi-infinite half-space. Elastic plane strain conditions are assumed. The theoretically infinite domain was truncated to allow for reasonable computation time for the FE simulation as depicted in Figure 3.4. The dimensions for the half space model are listed in Table 3.1. The Hertzian pressure and friction force were applied as a surface traction using the ABAQUS user-defined subroutine, UTRACLOAD. Equation (3.6) defines the normal component of the surface traction as a function of maximum Hertzian pressure (p_{max}), the coordinate of the center of the Hertzian pressure distribution (x_c, y_c) and the half-contact width, b.

$$t_y(x) = p_{max}\sqrt{1-\left(\frac{(x-x_c)}{b}\right)^2} \tag{3.6}$$

The magnitude of the surface traction in shear direction is given by Equation (3.7) where μ_s is the coefficient of friction. The shear traction was applied in the direction of rolling.

$$t_x(x) = \mu_s|t_y(x)| \tag{3.7}$$

(x, y) is the coordinate where the pressure is evaluated. By varying x_c the surface traction was translated over the half-space in a sequence of 41 discrete steps from $-2.5b$ to $2.5b$ in the rolling direction.

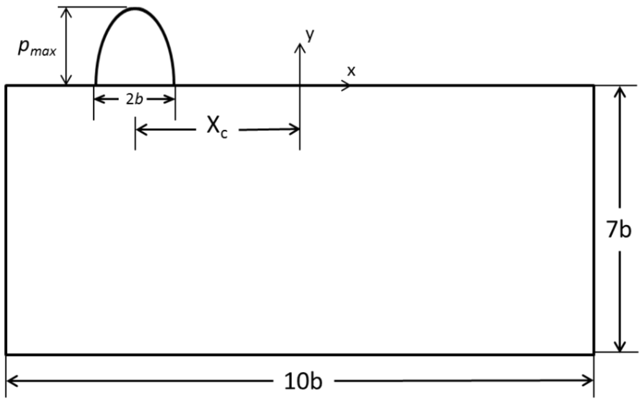

Figure 3.4: Computational domain used in FE simulation.

In the earlier investigations based on Voronoi tessellation (Jalalamadi and Sadeghi [29]), the mesh for the FE model was generated using a two-step process. The RVE is first discretized into Voronoi cells using the process described in section 2.1. In the second step, the Voronoi cells are divided into finer triangular elements by connecting pairs of adjacent vertices to the centroid of the cell. The FE mesh generated using this procedure will be referred to as 'Voronoi mesh' from here on. Figure 3.2 illustrates a Voronoi cell divided into finer triangular elements. It can be noted that the size of the RVE increase with the half-contact width. However, the size of the Voronoi cells remains the same irrespective of the half-contact width since Voronoi cells correspond to the grains in the material microstructure of the bearing steel. This results in a huge increase in the number of elements in the Voronoi mesh for larger domains. Figure 3.5(a) compares the number of elements in the Voronoi mesh for b = 100 µm and b = 400 µm. Therefore it is not computationally practical to use Voronoi mesh for modeling large bearings with half-contact width of much greater than 100 µm.

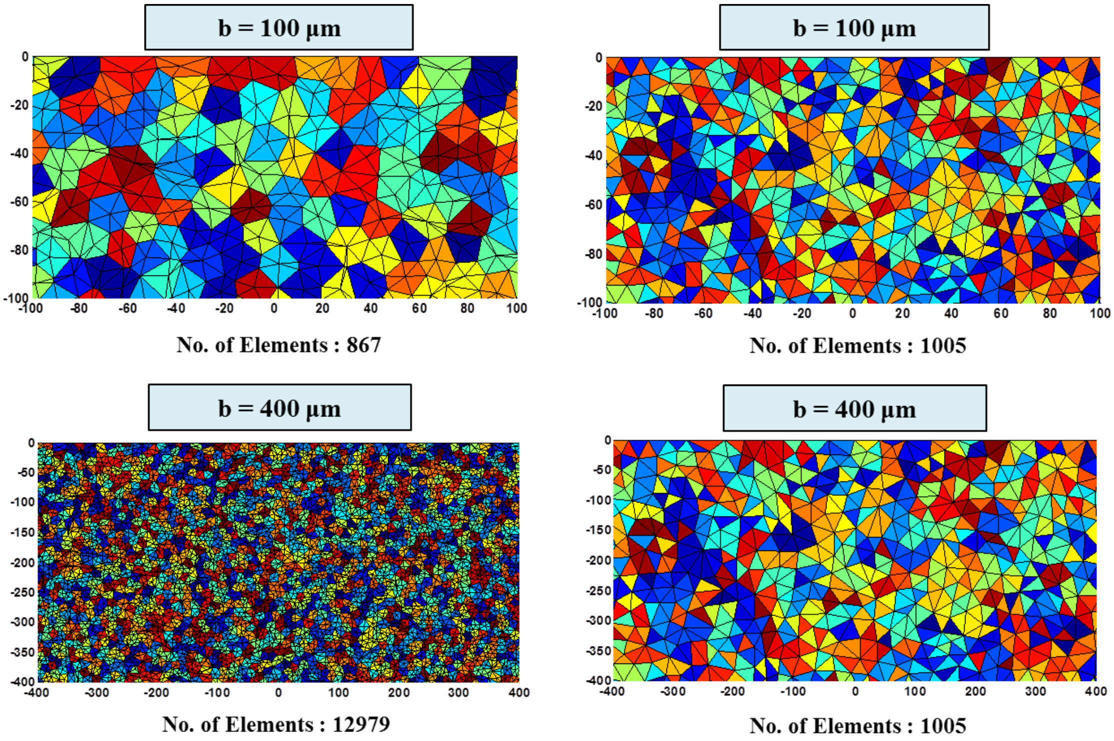

(a) (b)

Figure 3.5: Comparison of number of elements in the (a) Voronoi mesh and (b) Delaunay mesh for b = 100 µm and b = 400 µm.

In the current investigation, the problem associated with large number of element and significant computational effort was resolved by meshing the simulation domain with Delaunay triangles. Open source software, Triangle [98], was used for this purpose. This mesh is referred to as 'Delaunay mesh' in the current study. A finer mesh is used in the RVE while the mesh becomes progressively courser away from the contact region. The advantage of the Delaunay mesh is that it can be scaled according to the half-contact width so that the number of elements in the simulation domain remains the same as shown in Figure 3.5(b). Therefore, the time taken by ABAQUS to solve for the stress solution for a single load pass is the same regardless of the physical size of the model. This translates to significant computational benefits over the earlier investigations using Voronoi meshes throughout the RVE, especially for large-size bearings. However, this necessitates another step where Delaunay mesh needs to be coupled with the Voronoi tessellation based fatigue damage model. Figure 3.6 illustrates the flow chart for this procedure.

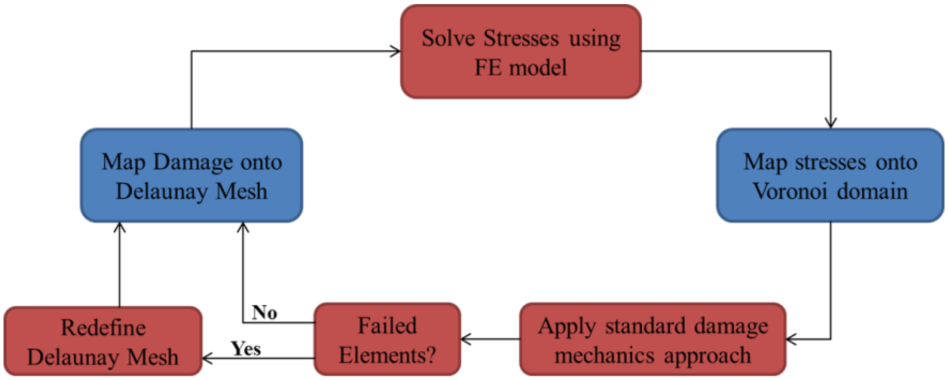

Figure 3.6: Flow chart for the procedure to couple Delaunay mesh with fatigue damage model.

3.2.4 Stress Mapping Procedure

Fatigue damage model involves applying damage evolution (Equation (3.4)) and constitutive relationships (Equation (3.3)) to each element in the Voronoi mesh within the material domain repeatedly until failure. Please note that Voronoi mesh represents the random material microstructure. Therefore, the fatigue damage model requires knowledge of the maximum shear stress reversal $\Delta\tau_{critical}$ along each Voronoi grain boundary. However, Delaunay mesh is used in FE simulations to obtain the state of stress after every load pass. In order to incorporate the Delaunay mesh in the fatigue damage model, a stress mapping procedure was developed. Figure 3.7 demonstrates the state of stress for the Delaunay mesh obtained from the FE simulation and mapped stresses on the Voronoi mesh. The Delaunay mesh consisting of constant strain triangles (CST elements) is used in ABAQUS to solve for the stress solution during a load pass (Figure 3.7(a)). Stress mapping procedure maps this stress solution onto the Voronoi mesh (Figure 3.7(b)) using a MATLAB function ‘ScatteredInterpolant’. This function performs an interpolation on a 2D scattered data and returns a surface which can be evaluated at any query point. ABAQUS provides stresses at the centroids of the elements in the Delaunay mesh. This data is passed to the MATLAB function and stresses at the centroids of the elements in the Voronoi mesh are evaluated. $\Delta\tau_{critical}$ is then calculated for each Voronoi element by transforming the state of stress along the grain boundary.

(a) (b)

Figure 3.7: State of stress for the (a) Delaunay mesh obtained from FE simulation and stresses mapped onto the (b) Voronoi mesh.

3.2.5 Numerical Implementation of Fatigue Damage Model

Since high cycle RCF life is in the range of billions of cycles, it is computationally impractical to employ fatigue damage model after every loading cycle. Therefore, the standard ‘jump-in cycles’ (JIC) approach developed by Lemaitre [100] is used in the previous RCF investigations ([27], [30], [97]) to make the solution tractable. In this approach, the stress-strain response is assumed to remain unaltered over a finite number of cycles, ΔN^i, in a block i. During this block of cycles, damage for each element is also assumed to remain constant. Thus, damage evolution is piecewise linear with respect to the block of cycles. A constant damage increment ΔD over that number of cycles is prescribed for the element which has largest damage evolution rate per cycle. However, as D approaches 1, damage evolution rate approaches infinity as evident in Equation (3.4). This causes ΔN^i to be less than 1, consequentially slows down the standard JIC algorithm. To avoid this situation and expedite the fatigue damage simulation, a modified JIC algorithm developed by Weinzapfel and Sadeghi [107] is used in this investigation. This modification is motivated by following two principles (I) strain energy is released by the formation and growth of damage as fatigue progresses, (II) the strain energy released in each block of cycles should advance the total by some minimum fraction of the previous total.

The step by step procedure for damage evolution as per modified JIC approach is given below:

i. The number of elapsed cycles, N, and released strain energy are initialized to 0. The material domain is assumed to contain no initial flaw. Hence, the initial damage of each Voronoi element is set to 0. Similarly, initial damage of 0 and pristine elasticity modulus is assigned to each of the Delaunay element.

$$\begin{aligned} &N^i = 0 \qquad && \varphi_D = 0 && \\ &D_j^0 = 0 && && j = 1 \ldots n_V \text{ (Voronoi elements)} \\ &D_k^0 = 0 && E_k^0 = E && k = 1 \ldots n_D \text{ (Delaunay elements)} \end{aligned} \tag{3.8}$$

ii. Alternating shear stress along the Voronoi grain boundary $(\Delta\tau_{critical})_j^i$ for the current loading cycle is evaluated by stress mapping procedure. The damage evolution rate for each Voronoi element j is then calculated using the current alternating shear stress and state of damage for that element.

$$\left(\frac{dD}{dN}\right)_j^i = \left[\frac{(\Delta\tau_{critical})_j^i}{\tau_r(1 - D_j^i)}\right]^m \tag{3.9}$$

iii. The maximum damage evolution rate in the domain is determined and number of cycles in the current block is computed as

$$\Delta N_D^i = \frac{\Delta D}{\left(\frac{dD}{dN}\right)_{crit}^i} \qquad \textit{Where, } \left(\frac{dD}{dN}\right)_{crit}^i = \underset{i}{Max}\left(\frac{dD}{dN}\right)_j^i \tag{3.10}$$

iv. In addition, the maximum damage strain energy release rates (Y) for Voronoi elements are calculated by Equation (3.11). The damage strain energy rate is defined as variation in the sum of the shear strain energy and volume dilatation energy due to an infinitesimal increase of damage at constant stress [111].

$$Y_j^i = \frac{(\sigma_{eq,j}^i)^2 R_{v,j}^i V_j}{2E\left(1 - D_j^i\right)^2} \qquad \textit{Where, } R_{v,j}^i = \tfrac{2}{3}(i + \nu) + 3(1 - 2\nu)\left(\frac{\sigma_H}{\sigma_{eq}}\right)^2 \tag{3.11}$$

Vj is the volume of the element; σ_H and σ_{eq} are measured at the step during the loading cycle where σ_{eq} is maximum.

v. The strain energy released during the current block of cycles $(\Delta\varphi_D^i)$ is calculated. State of the damage in each element is updated

$$\begin{gathered} \Delta\varphi_D^i = \sum Y_j^i \left(\frac{dD}{dN}\right)_j^i \Delta N_D^i \\ D_j^{i+1} = D_j^i + \left(\frac{dD}{dN}\right)_j^i \Delta N_D^i \end{gathered} \tag{3.12}$$

vi. The ratio of increment in strain energy to the total strain energy released thus far is compared to a desired minimum ratio. If the ratio is less than the threshold, then the number of cycles in the current block is supplemented by a number of cycle,

$$\Delta N_{\phi}^{i} = \begin{Bmatrix} 0, & \dfrac{\Delta\varphi_D^i}{\varphi_D} \geq f \\ \left(\dfrac{f\varphi_D}{\Delta\varphi_D^i} - 1\right)\Delta N_D^i, & \dfrac{\Delta\varphi_D^i}{\varphi_D} < f \end{Bmatrix} \tag{3.13}$$

$$\Delta N^i = \Delta N_D^i + \Delta N_{\varphi}^i$$

The value for the threshold ratio, *f*, must be chosen wisely. If *f* is set to 0, then the modified JIC algorithm is exactly same as the standard JIC algorithm, however it causes large errors in the solution if *f* is chosen to be arbitrary large number. [32], [107] have performed a detailed study on the effect of *f* on the RCF simulation.

vii. The state of damage and strain energy release are updated according to the revised number of cycles in the current block

$$\begin{aligned} \Delta\varphi_D^i &= \Delta\varphi_D^i + \sum Y_j^i \left(\frac{dD}{dN}\right)_j^i \Delta N_{\phi}^i \\ D_j^{i+1} &= D_j^{i+1} + \left(\frac{dD}{dN}\right)_j^i \Delta N_{\phi}^i \end{aligned} \tag{3.14}$$

viii. Finally, the total number of cycles elapsed (*N*) and total released strain energy (φ_D) are updated.

$$\begin{aligned} \varphi_D &= \varphi_D + \Delta\varphi_D^i \\ N &= N + \Delta N^i \end{aligned} \tag{3.15}$$

ix. The state of damage is mapped back onto the Delaunay mesh using the procedure similar to stress mapping. The state of damage on the Voronoi mesh (b) and the mapped state of damage on Delaunay mesh (a) is depicted in Figure 3.8.

$$\begin{aligned} & D_j^{i+1} \overset{map}{\Longrightarrow} D_k^{i+1} && \textit{j = 1 ... n}_V\textit{ (Voronoi elements)} \\ & E_k^{i+1} = E(1 - D_k^{i+1}) && \textit{k = 1 ... n}_D\textit{ (Delaunay elements)} \end{aligned} \tag{3.16}$$

In the present investigation, a kill element approach developed by Slack and Sadeghi [97] has been used for damage propagation. In this formulation, the simulation will continue with the completely damaged elements, i.e. state of damage equal to critical damage value, until another element fails. Therefore, the damaged elements will have zero stiffness and act as voids in the simulation domain. This method allows damage to propagate continuously through the material microstructure, whereas the node release procedure assumes damage to be localized at the grain boundaries. The simulation ends when the damage propagates to the surface and forms a spall.

(a) (b)

Figure 3.8: State of damage for the Voronoi mesh (b) obtained by modified JIC algorithm and damage mapped onto the Delaunay mesh (a).

3.2.6 Dynamic Remeshing Tool

Due to the difference in the number of elements in the Voronoi and Delaunay meshes, there could be a loss of information while communicating the stresses and the damage states between the two meshes. For this reason, a remeshing procedure was developed to redefine the Delaunay mesh in order to compute the stresses accurately in the critically damaged region. This remeshing procedure involves identifying Voronoi elements around the critically damaged elements after every load pass. Elements having centroids within a 15 μm radius from the centroid of a failed element are found. These elements are imported directly into the FE mesh, while the remainder of the domain is meshed using Delaunay triangles. This process guarantee that the exact damaged areas of the Voronoi cell microstructure are analyzed in the FEA solution, and that the resulting stresses are communicated precisely back to the Voronoi mesh in the critical regions where damage is rapidly evolving. Figure 3.9 demonstrates the remeshing process where critically damaged elements are depicted in black color, while the surrounding elements are colored in red. These elements also appear in the FE mesh (Figure 3.9(a)) and the remainder of the domain comprising of Delaunay triangles are shown in white. The progression of Delaunay mesh at various stages of the simulation is depicted in Figure 3.10. The damaged elements depicted in black color form the spall.

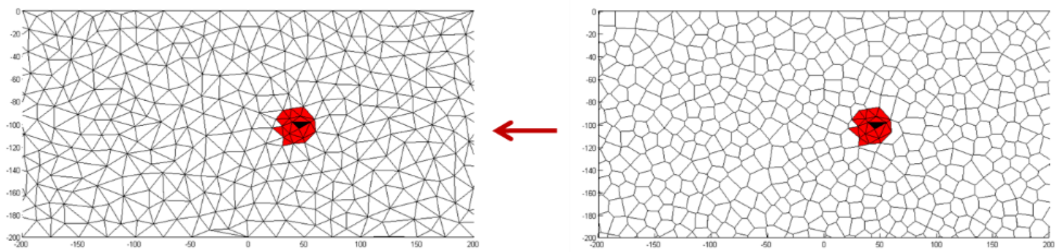
(a) (b)

Figure 3.9: Remeshing procedure: (a) Delaunay mesh, (b) Voronoi mesh. Critically damaged Voronoi elements are colored black and Voronoi elements surrounding the critically damaged elements are colored red.

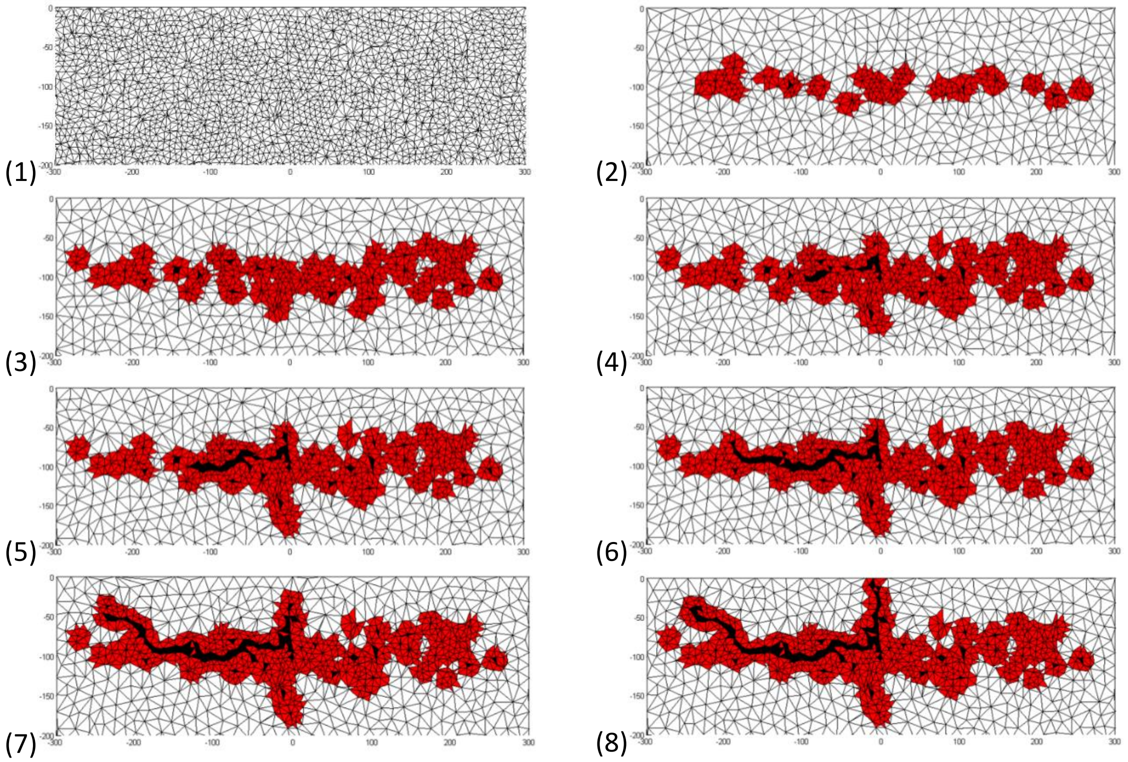

Figure 3.10: Progression of the Delaunay mesh at various stages of simulation (*b* = 200 μm). The spall pattern is shown in black color. The Voronoi mesh is depicted in (1).

3.3 Results and Discussion

This section describes results obtained from the new modeling approach for simulating sub-surface initiated spalling in cylindrical roller bearings of varying sizes. Typical dimensions of contact region between rollers and raceway can be of the order of a hundred to a few thousand microns depending on the size of the bearing. Therefore the RCF model was used to compare spall patterns and fatigue lives for domains of contact width ranging from 50 to 1000 μm. The grain diameters, d_g, for bearing steel are in the order of 10 μm. This grain size was used during Voronoi tessellation procedure to generate 35 random microstructure domains for each contact width to study the influence of subsurface microstructure topology on fatigue lives. Table 3.2 summarizes the material and damage parameters used for this study. The material properties are assumed to be isotropic and homogenous. Maximum Hertzian pressure of 2.0 GPa and coefficient of friction of 0.05 are prescribed in Equation (3.6) and Equation (3.7) to define applied traction. A constant damage increment (ΔD) and threshold strain energy ratio, f, used in modified JIC algorithm are 0.25 and 0.015 respectively.

Table 3.2: Material properties used in the simulation.

Material	AISI 52100
Undamaged elasticity modulus, E	200 GPa
Poisson's ratio, v	0.3
Material grain diameter, d_g	10 μm
Maximum Hertzian pressure, p_{max}	2 GPa
Surface coefficient of friction, μ_s	0.05
Damage rate law coefficient, τ_r	6113 MPa
Damage rate law exponent, m	10.1
Critical damage value, D_{crit}	1

3.3.1 Fatigue Life Predictions and Spall Patterns

The validity of the model is first assessed by comparing the results for b = 100 μm with previous 2D RCF models based on Damage mechanics and Voronoi tessellation. A Weibull cumulative distribution function is commonly used to characterize the scatter of fatigue lives in roller element bearings. The slope of the line for 2-parameter Weibull distribution provides the measure for the scatter present in the life data. Smaller Weibull slopes indicate more scatter in the data. L_{10} life describes the number of load cycles that 90% members of the population can expect to survive. Table 3.3 presents the comparison of Weibull slopes and L_{10} lives for initiation and final lives obtained from the current model and Slack and Sadeghi [97]. It can be observed that the results are in good agreement with the previous results. Please note that these slopes represent the scatter in fatigue lives due to the variability in stresses acting on the grain boundaries or weak planes alone. In this study, the initiation life was defined as the life cycles at which the first damage occurs in the domain i.e. when the damage value of the first element reaches 1. The initiation phase constitutes an average of 86.9% of the total life. This is also in accordance with the general observation that the initiation phase dominates the high cycle fatigue [95].

Table 3.3: Comparison of results obtained with current model to previous model by Slack and Sadeghi [97] for half-contact width of 100 μm.

	Initiation lives	**Final lives**		
	Weibull slope	**Weibull slope**	**L_{10} life**	**Avg. % initiation**
Ref. [97]	7.15	12.54	1.61E+07	85.9
Current model	5.16	8.38	1.58E+07	86.9

Figure 3.11 depicts the Weibull probability results for (a) the initiation lives and (b) final lives for different contact sizes. Table 3.4 lists the Weibull slopes and L_{10} lives for the same. Two important inferences can be made using these results: (I) the Weibull slopes systematically increase as contact size increases, i.e. the scatter in fatigue lives decreases for larger bearings (II) the L_{10} lives for larger contact size are higher. The first phenomenon can be explained as following: as the bearing size becomes larger, the number of Voronoi grains/weak planes in the critically stressed region (around $0.5b$ below the surface) also increase. Therefore, probabilistically, larger domains have much better chance of having at least one Voronoi cell which has the orientation that causes higher critical stress during initiation. This causes the initiation life to be more deterministic, increasing the Weibull slopes. This also explains why crack propagation life is less for larger contacts than for smaller contacts, which is evident by the increase in the ‘average % initiation’ with the contact size (See Table 3.4).

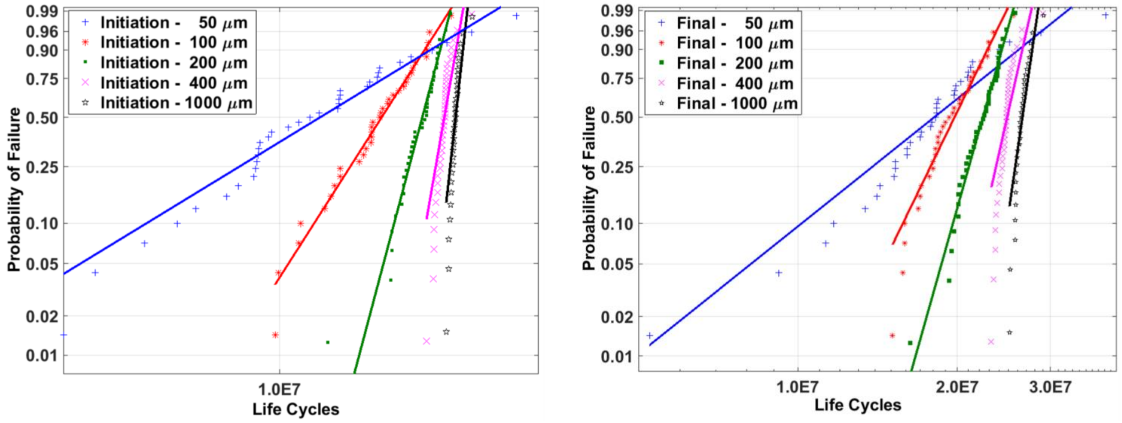

(a) (b)

Figure 3.11: Weibull probability plots for (a) initiation and (b) final lives for different contact sizes.

Table 3.4: Predicted Weibull slopes and L10 lives for different contact sizes.

	Initiation lives		**Final lives**		
***b* (µm)**	**Weibull slope**	**L_{10} life**	**Weibull slope**	**L_{10} life**	**Avg. % ini**
50	2.01	4.86E+06	3.26	1.02E+07	71.0
100	5.16	1.21E+07	8.38	1.58E+07	86.9
200	12.39	1.87E+07	14.47	1.96E+07	96.5
400	18.87	2.21E+07	18.14	2.23E+07	98.3
1000	29.99	2.44E+07	28.08	2.46E+07	98.0

To substantiate the second observation (II), the relationship between half-contact width (*b*) and basic life rating (L_{10} life) is formulated for cylindrical roller bearing according to the ISO 281 standard [9]. To derive this formulation, basic Hertzian relationships for line contact need to be considered. Maximum Hertzian pressure P_{max} and half-contact width, (*b*), for two cylinders in contact carrying a load *F* is given by

$$p_{max} = \frac{2F}{\pi b L} \tag{3.17a}$$

$$b = \sqrt{\frac{2FD'}{\pi L E'}} \qquad \rightarrow \qquad F = \frac{b^2 \pi L E'}{2D'} \tag{3.17b}$$

$$E' = \frac{1-\nu_1^2}{E_1} + \frac{1-\nu_1^2}{E_1} \quad \& \quad D' = \frac{2r_1 r_2}{r_1 + r_2} \tag{3.17c}$$

Where, *L* is the length of the cylinders; *D'* is the equivalent diameter and *E'* is the equivalent stiffness. Substituting *F* from Equation (3.17a)b) into Equation (3.17a) and simplifying yields

$$p_{max} = \frac{E'b}{D'} \tag{3.18}$$

From Equation (3.17a) and Equation (3.18), it can be deduced that for fixed p_{max}, the half-contact width, b, is directly proportional to applied load F and equivalent diameter D'. Hence,

$$b \propto F \tag{3.19a}$$

$$b \propto D' \tag{3.19b}$$

Now, the basic life rating for roller bearing as per ISO 281 is given by

$$L_{10} = \left(\frac{C_r}{P_r}\right)^{10/3} \tag{3.20a}$$

$$C_r = b_m f_c \left(i\, L_{we} \cos\alpha\right)^{7/9} Z^{3/4}\, D_{we}{}^{29/27} \tag{3.20b}$$

$$f_c\ is\ a\ function\ of \left(\frac{D_{we}\cos\alpha}{D_{pw}}\right) \tag{3.20c}$$

Considering radial roller bearings of equal breadth but different diameters such that the radial dimensions of all components are scaled equally, D_{we} (rolling element diameter) is the only factor in Equation (3.20a) which changes with the bearing size. f_c is a function of the ratio of component diameters expressed in Equation (3.20a), b_m is bearing type factor, i is number of rows of rollers, L_{we} is length of roller and Z is number of rollers. Further, for radial roller bearing contact angle $\alpha = 0^o$. If the bearing is subjected to radial load only, P_r is equal to the applied load F. From Equation (3.19a), we know that the bearing size is directly proportional to half-contact width, b. Therefore, P_r and C_r can be expressed in terms of half-contact width, b as follows:

$$C_r \propto D_{we}^{29/27} \quad \rightarrow \quad C_r \propto b^{29/27} \tag{3.21a}$$

$$P_r = F \quad \rightarrow \quad P_r \propto b \tag{3.21b}$$

Using these relationships in Equation (3.20a), relationship between L_{10} life and b can be determined

$$L_{10} = \left(\frac{C_r}{P_r}\right)^{10/3} \quad \rightarrow \quad \mathrm{L}_{10} \propto \left(\frac{b^{\frac{29}{27}}}{b}\right)^{10/3} \quad \rightarrow \quad \boldsymbol{L_{10} \propto b^{20/81}} \tag{3.22}$$

Therefore, if the size factor f_s is defined as the ratio of two contact widths, the ratio of corresponding L_{10} lives for same type of radial roller bearing can be expressed as

$$\frac{L_{10}(b_2)}{L_{10}\,(b_1)} = \left(\frac{b_2}{b_1}\right)^{20/81} = f_s^{20/81} \tag{3.23}$$

It is evident from Equation (3.23) that, if contact pressure is fixed, a longer L_{10} life is expected for the larger bearing with the same breadth i.e. larger contact size. In Figure 3.12, the ratio of L_{10} lives calculated using Equation (3.23) is plotted against the size factor, f_s. The ratios obtained from the model are shown with square markers. For this purpose, b = 100 µm is considered to be the base contact width. It can be seen that there is a good correlation between the model results and basic life rating for radial roller bearing as per ISO 281.

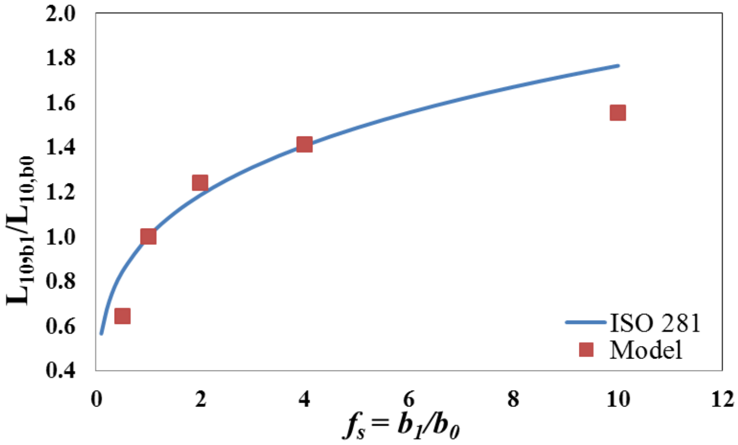

Figure 3.12: Relationship between L_{10} lives and size factor f_s from the model results and Equation (3.23) derived from ISO 281.

Figure 3.13 depicts the typical spall patterns for different contact sized obtained from the model. It was observed that spalls initiate at around a depth of *0.5b* from the surface for all cases. This is expected since this is the region where maximum shear stress reversal ($\Delta\tau_{critical}$) occurs. After initiation, the damage propagates parallel to the surface before turning upwards and propagating towards the surface at steep angle (>45^{o}) in the direction of applied friction. Further, the width of the spall increases with increase in the contact size. The simulation was stopped when first crack reached to the surface. However, most experimentally observed spalls show multiple cracks reaching the surface as shown in Figure 3.14 (Tallian [114] and Lou, et al. [5]). Therefore, the simulation was continued for few more loading cycles after the first crack reaches the surface for a couple of domains with b = 400 µm. The resulting spall patterns as depicted in Figure 3.15 show good resemblance to the experimental results.

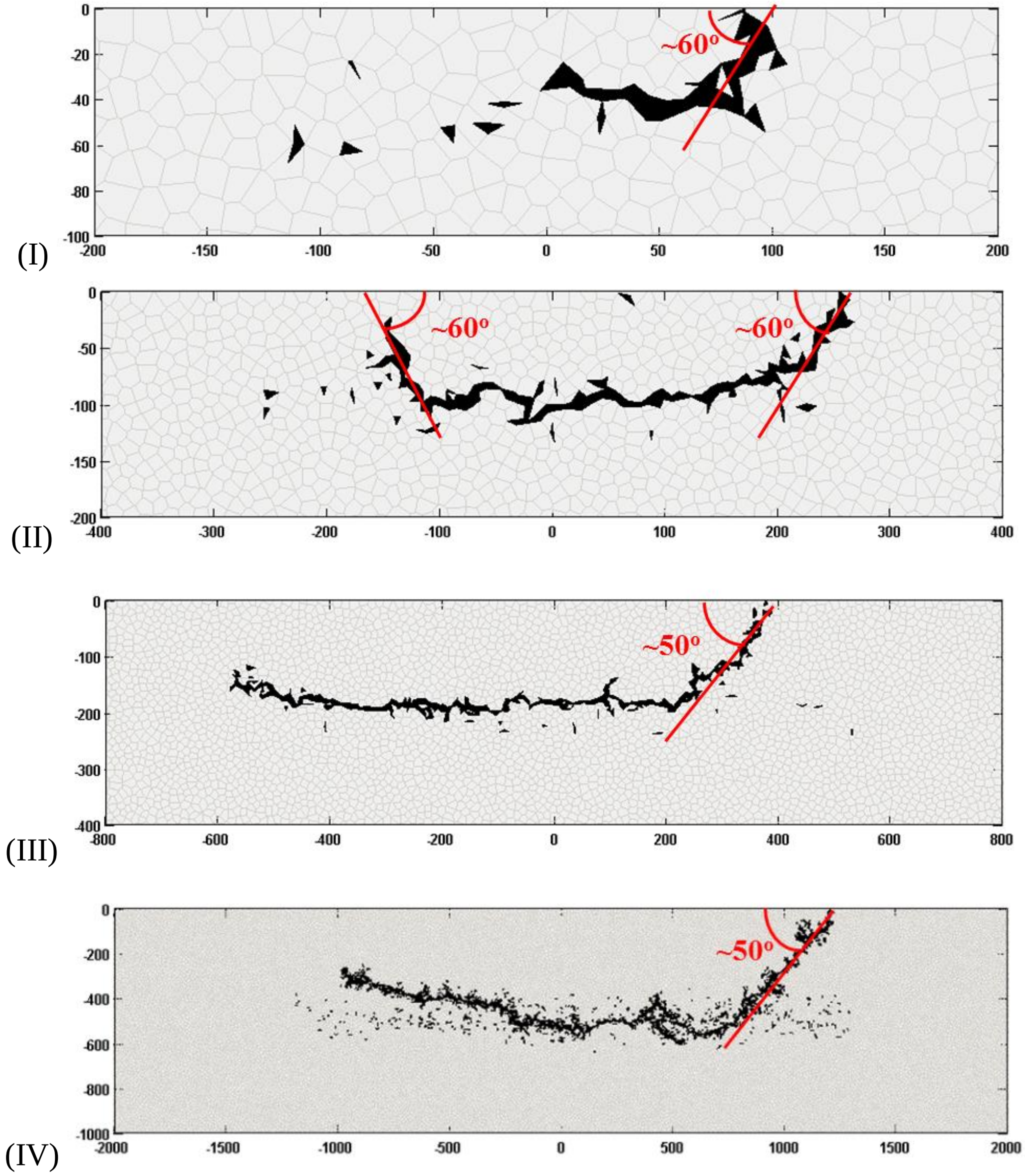

Figure 3.13: Typical spall patterns obtained from the model for different contact sizes (I) b = 100 µm (II) b = 200 µm (III) b = 400 µm (IV) b = 1000 µm

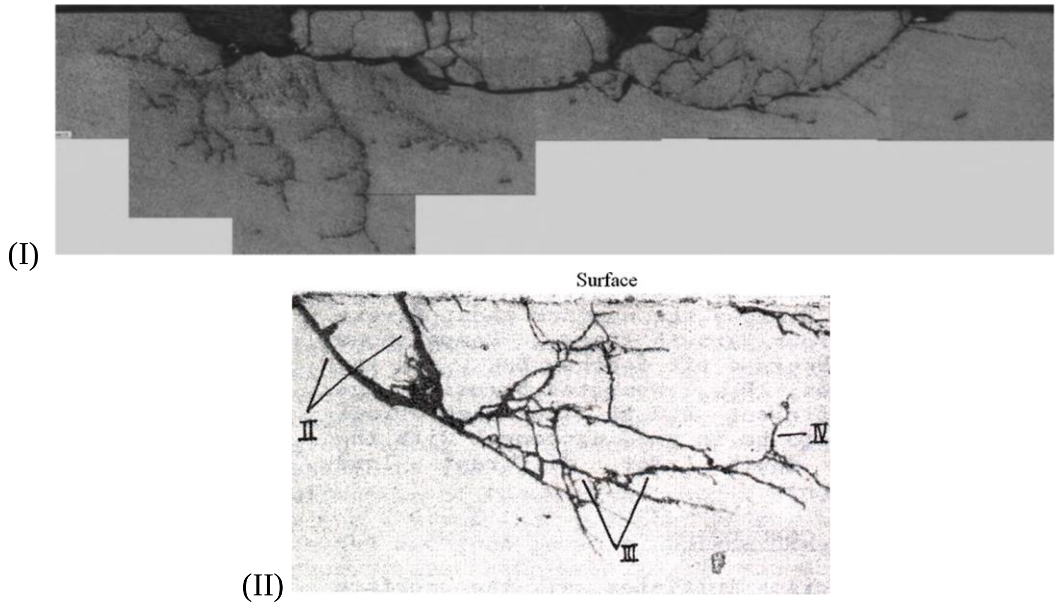

Figure 3.14: Experimentally observed spall patterns (I) Tallian [114]; (II) Lou, et al. [5]

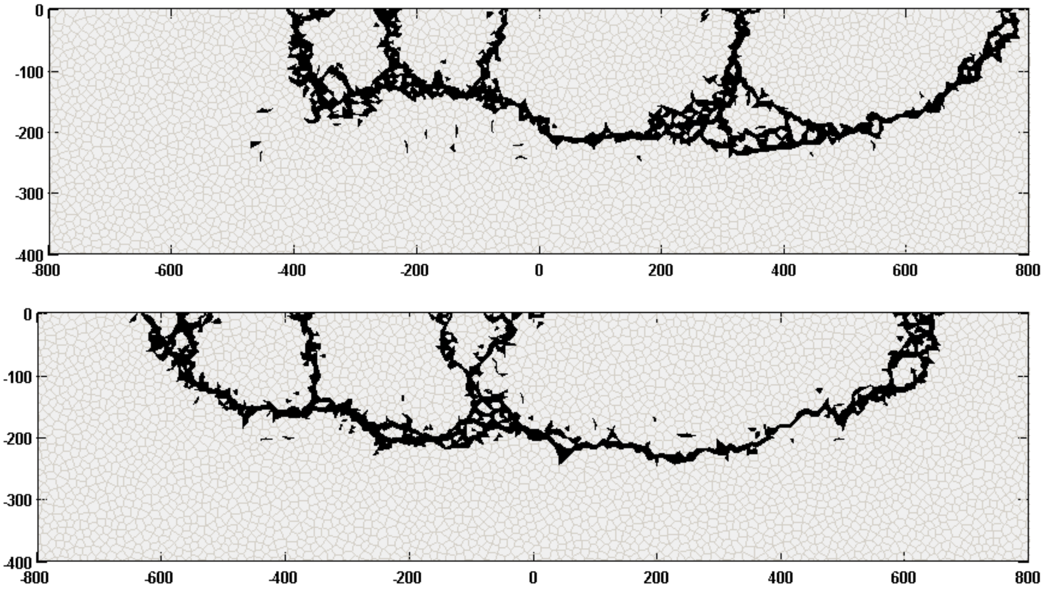

Figure 3.15: Spalls obtained from the model by continuing the simulation after the first crack reaches the surface. (*b* = 400 µm)

3.3.2 Effect of Material Flaws

It can be noted that the scatter in the fatigue lives observed in the model results is considerably less than what is generally observed in the experiments. Harris and Barnsby

[115] state that fatigue data for AISI 52100 steel follow a range of Weibull slopes between 0.51 and 5.7. Possible reason for high Weibull slopes could lay in the assumption that the material domain is homogeneous and free of voids and inclusions. Rolling contact fatigue is strongly influenced by the steel cleanliness [116]. Cracks are often found to initiate around the interfaces of the inclusions, voids and other inhomogeneities in the material. These material defects are randomly distributed within the material, which consequently reduces the fatigue lives and increases their scatter. Ai [116] has investigated the effect of steel cleanliness on the bearing fatigue life. In this section, the model was expanded to incorporate a distribution of initial internal voids and its effect on the RCF life is explored. Two types of initial voids, small and large, are investigated using an approach similar to Slack and Sadeghi [97]. Small void was introduced by setting the elasticity modulus of a Voronoi element equal to zero and large void was modeled by setting the elasticity modulus of all the Voronoi elements within a Voronoi cell equal to zero. Figure 3.16 illustrates the types of initial voids investigated in this study. The sizes of the initial voids correspond well with the experimentally observed range for inclusions in bearing steel [117]. The initial voids were placed within the bounds of microstructure topology region i.e. $-2b < x < 2b$ and $-1b < y < 0$. However, they were not allowed to occur on the surface.


(a) (b)

Figure 3.16: Types of initial voids randomly placed in the microstructure topology region (a) small void and (b) large void. Elasticity modulus of elements colored in red is set to 0.

Simulations were performed for 35 random microstructure domains of size b=100 µm with 1 randomly placed initial void. Figure 3.17 displays the Weibull probability plots for final lives obtained from the model for pristine, small void and large void cases. Table 3.5 presents the Weibull slopes and L_{10} lives for the results shown in Figure 3.17. It is evident that the presence of initial voids results in significant increase in the scatter in the fatigue.

Further, it also causes considerable reduction in L_{10} lives with larger void resulting in more reduction than small void. The average percentage of life spent during initiation also decreases going from pristine to large void. These observations are in accordance with the expectation since larger initial voids results in a bigger stress concentration. The typical spall patterns for small and large initial void are depicted in Figure 3.18. The initial void is colored in red and failed elements that form the spall are colored in black. In majority of the cases the spalls initiated from the initial voids, however if the void occurred farther from the critically stressed region, it did not give rise to the spall. These results are in agreement with the results from the previous RCF models [97].

Table 3.5: Comparison of scatter and fatigue lives for different simulation conditions for domains with half-contact width of 100 μm.

Simulation condition	**Final lives**	
	Weibull slope	**L_{10} life (cycles)**
Pristine	8.38	1.58E+07
1 small initial void	2.82	6.32E+06
1 large initial void	1.44	1.10E+06

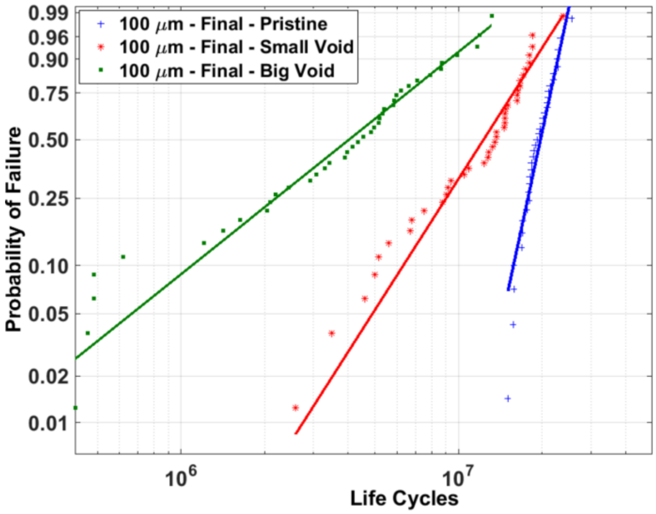

Figure 3.17: Weibull probability plots for final lives for different simulation condition (*b* = 100 μm).

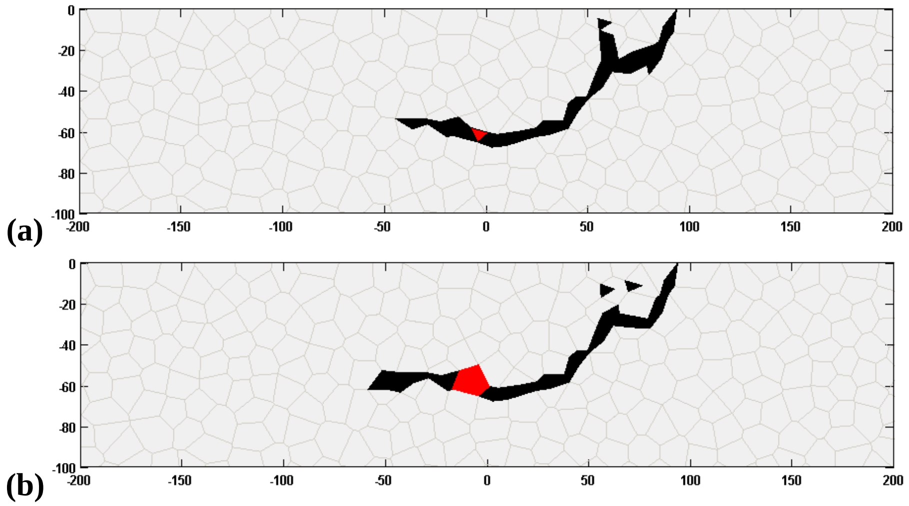

Figure 3.18: Typical spall pattern for randomly placed (a) small and (b) large initial void for b = 100µm. The initial void is colored in red.

The effect of initial voids on the fatigue of different sized bearings was also investigated. The procedure to introduce the small and large voids is the same as before. Therefore, the size of the voids does not change for different contact widths. However, to keep the initial void density the same, the number of initial voids was increased for larger contact width according to the area of the microstructure topology region. Since the area is proportional to the square of the half-contact width, b; 1, 4 and 25 initial voids are placed randomly in the microstructure topology region for $b = 200$, 400 and 1000 µm respectively. Simulations were carried out for 35 microstructure domains for each contact width and with small and large voids. Figure 3.19 presents examples of spalls obtained from the model for different simulation conditions. Figure 3.20 illustrates the Weibull probability plots for the fatigue life data for simulation with initial voids obtained from the model. The summary of the results of the simulations is presented in Table 3.6. It is worth noting that the Weibull slopes for the final lives are within the experimentally observed range after the effect of initial defects is taken into account. Furthermore, for both types of initial voids, the L_{10} lives decreased with increase in the contact size as expected and commonly observed in the applications. This can be explained as follows. The number of initial defects and number of Voronoi cells in the critically stressed region rises as the bearing size increases. Consequently, the probability of an initial defect occurring at the critically stressed region also increases, resulting in the reduction in the fatigue lives.

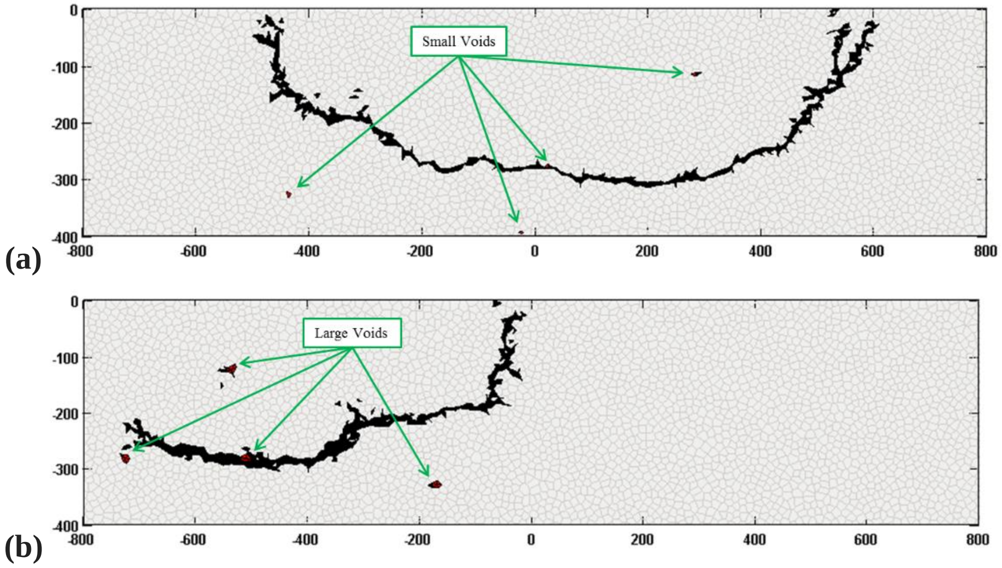

Figure 3.19: Examples of spalls obtained for different simulation condition. (a) 4 small initial voids randomly placed in the domain with b = 400μm (b) 4 large initial voids randomly placed in the domain with b = 400μm The initial void is colored in red.

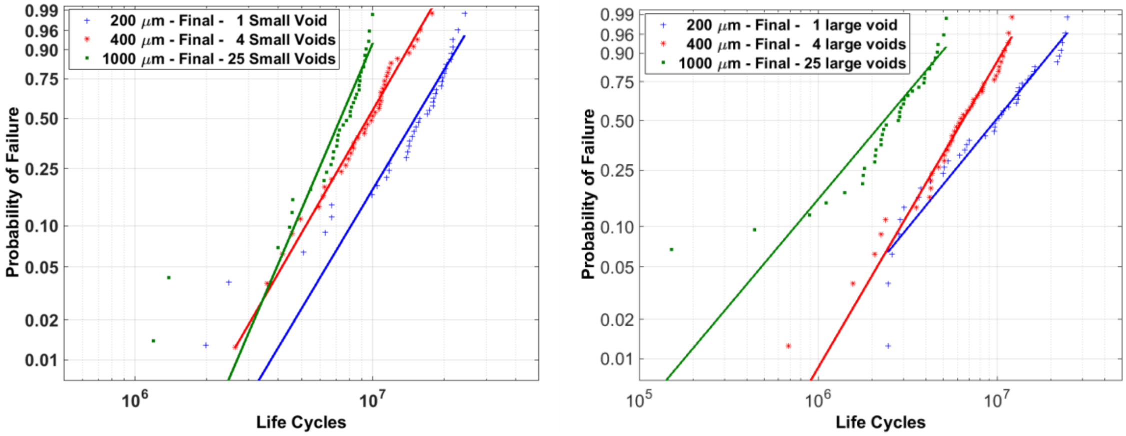

(a) (b)

Figure 3.20: Weibull probability plots for final lives for different contact sizes having same initial void density (a) small voids and (b) large voids.

Table 3.6: Weibull slopes and L_{10} lives obtained for different contact sizes with same initial void density.

***b* (µm)**	**Initial voids**	**Final lives**	
		Weibull slope	**L_{10} life (cycles)**
200	1 small	3.03	8.11E+06
200	1 large	1.69	3.27E+06
400	4 small	3.12	5.22E+06
400	4 large	2.37	2.88E+06
1000	25 small	4.22	4.67E+06
1000	25 large	1.65	7.38E+05

3.4 Summary and Conclusions

This chapter presented a computationally efficient modeling approach for investigating subsurface initiated spalling and attempts to predict the variability in rolling contact fatigue lives for large rolling element bearings. The model incorporates damage mechanics constitutive relations in a finite element model to capture progressive damage for rolling contact fatigue of AISI 52100. Randomly generated Voronoi tessellations were used to study the variability occurring due to the randomness in material microstructure. However, this approach decoupled the Voronoi mesh from the FE solution. Instead, Delaunay triangulation was used to generate the FE mesh. A mapping procedure was developed to communicate the state of stress and damage between FE mesh and Voronoi tessellations. A remeshing tool was developed to refine the mesh as the fatigue damage advances. Use of a Delaunay mesh significantly reduced the simulation time compared to the previous approach as demonstrated in Table 3.7. The new approach showed 50% improvement in the computational time for contact size of 200 µm. The new approach required 15 hours on an average to complete the simulation for one domain while the previous approach took more than 30 hours for the same simulation. For 400 and 1000 µm domains, the simulation conducted using previous approach was allowed to run for 200 hours, yet did not finish. However, when the new approach was implemented the simulations concluded between 25 to 80 hours on the average for contact sizes of 400 and 1000 µm, respectively. To summarize, the new model enabled simulation of RCF for contacts up to an order of magnitude larger than previously possible with similar models. For equivalent contact pressures and bearing width, the simulated RCF lives were shown to increase for bearings of larger diameter and these results were substantiated by calculations of the basic rating life per ISO 281. Additionally, the shapes of the spalls obtained from the model were found to resemble those commonly observed in experiments. When initial flaws were included in the model, the scatter in the fatigue lives was within the experimentally observed range and L_{10} lives decreased with increasing contact size as expected.

Table 3.7: Comparison between average computational times taken by previous and new approach to complete one simulation domain.

Half-contact width, b (μm)	**Time in hrs.**	
	Previous approach	**New approach**
100	3	3
200	30	15
400	>200	25
1000	>200	80

4. ROLING CONTACT FATGUE IN CASE CARBURIZED STEELS

4.1 Introduction

Bearing manufacturers have used various techniques to increase the working life of REBs, of which one of the ways is to limit the RCF related bearing damage. Hardened steels are commonly used in high-performance ball and rolling element bearings. The hardening of steel is usually achieved by some type of heat treatment, which either hardens the part throughout its thickness or generates a hardened exterior that progressively tapers into a softer core beneath the surface. The first type of material is called “through hardened” and the second “case hardened.”

Many researchers (Bhatacharya et al. [118], Widmark and Melander [119], Scott [120], Zwirlein and Schlicht [121]) have studied the effect of hardness on the rolling contact fatigue life. There is a general trend of increase in fatigue life with increasing hardness [122]. However, most of this research focused on experimental investigation of the effect of hardness on RCF lives. There are not many analytical models to simulate the material hardness and describe its effect on the RCF life. The current model was used to simulate rolling contact fatigue of case carburized bearing steel with different case depths and investigate the effect of hardening process on RCF lives. Based on the results of the micro-indentation tests, the variation of hardness with depth was assumed to be bilinear for the case carburized steel. The effect of the carburizing process was incorporated by changing the yield strength of the material linearly with the hardness and including the residual stress distribution in the model. Thus, Mises based plasticity model with kinematic hardening was implemented in the FE model to incorporate material plasticity. The geometric disorder and randomness in the material microstructure was simulated using Voronoi tessellation to account for the variability in rolling contact fatigue life. Material degradation due to fatigue damage was modeled using continuum damage mechanics. Equivalence between torsion and rolling contact fatigue was utilized to determine the damage parameters in the elastic and plastic damage law. The damage evolution laws were modified to include the effect of residual stress. Experimental torsion SN results for through-hardened AISI 52100 with yield strength of 2GPa was used to assume SN plots for the materials having other yield strength values.

The FE model developed for this investigation was used to carry out simulations of rolling contact fatigue of case carburized and through hardened bearing steel under various operating conditions. Since, the location of the initial damage in rolling contact depends on the half-width of the contact (*b*), all the dimensions in this study are normalized with *b*, which was fixed at 100 μm. To assess the effect of plastic deformation, the Hertzian pressure was varied from 2 to 3.5 GPa for all cases. First, the effect of hardness variation was analyzed without including the effect of the residual stress. Then, the effect of residual stress distributions was studied with constant yield strength throughout the depth. In the end, the combined effect of hardness variation and residual stress distribution for the case carburized steel was investigated. From the results of the model, an equation for RCF life considering hardness and residual stress distribution was derived. The model was used to determine the optimum case depth for the case carburized materials. The results suggest that the RCF lives are maximum for the materials with a case-depth of 6.2b at low loads and 7.6b for high loads.

4.2 Modeling Approach

4.2.1 Microstructure Topology Model

Fatigue experiments demonstrate a high degree of variability in lives even under identical loading and environmental conditions. Miller [22] showed that the scatter in fatigue lives can be explained by considering the effect of the heterogeneous microscale features such as grain size and orientation, distribution of initial defects and material inclusions on early crack growth. In RCF, the localized nature of the contact stresses enhances the effects of the material microstructure on the fatigue life and results in the scatter in the fatigue lives of otherwise identical bearing. A single phase polycrystalline material contains micron level grains of random sizes and shapes. Mücklich et al. [92], Espinosa and Zavattieri [93]; Jalalahmadi and Sadeghi [29] showed that Voronoi tessellations can be used to represent the grain structure of the polycrystalline material to a good degree of accuracy and can be used to simulate its effect on the fatigue life. Thus, this approach has been widely applied in numerical investigation ([27], [30], [33], [97], [107]) to account for geometric disorder and the randomness in the material microstructure topology. It assumes that the Voronoi cells and their boundaries resulting from a random tessellation represent the grains and grain boundaries respectively in the real microstructure.

In the Voronoi tessellation procedure, a set of distinct nucleation or seed points are randomly placed in the Euclidian space. A region is formed around every seed point with the condition that it consists of points which are closer to the seed point of that region than any other seed point in the domain. The set of points which are equally close to more than one seed point define the boundary between the regions formed by corresponding seed points. This process results in a set of convex polygons referred to as Voronoi cells. The Voronoi cells have different number of sides with the most probable number of 6. The grain size in the generated microstructure can be controlled by specifying the minimum distance constraint between two nucleation points. The representative volume element (RVE) was identified as the critically stressed region during a rolling pass. It was hypothesized that the topological randomness in the RVE region has a major contribution to the fatigue life scatter. The microstructure topology region was restricted to the RVE to reduce the computational expense. The dimensions for the microstructure topology region are given in Table 4.1 in terms of half-contact width, *b*. Distinct simulation domains were generated by randomly distributing the seed points in the RVE. Figure 4.1(a) depicts a random material microstructure generated using a Voronoi tessellation. To generate the triangular mesh for the FE model, the Voronoi cells are divided into finer triangles by connecting pairs of adjacent Voronoi edge vertices to the centroid of their Voronoi cell. Figure 4.1(b) illustrates a Voronoi cell divided into finer triangular elements.

Table 4.1: Model dimensions.

Dimension	**Microstructure topology region**	**Simulation domain**
X (half-contact width)	*(-b, b)*	*(-5b, 5b)*
Y (half-contact width)	*(0, -1b)*	*(0, -7b)*

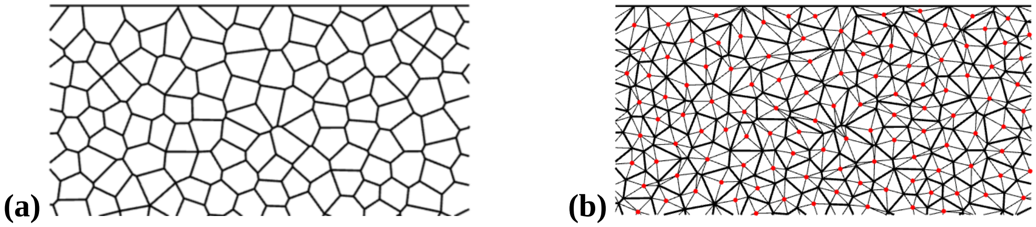

Figure 4.1: (a) Random material microstructure generated using a Voronoi tessellation. (b) Triangular FE elements generated by connecting the centroids (red dots) of the Voronoi cells to the edges.

4.2.2 Modeling Case Carburized Steel

Hardened steels are commonly used in high-performance ball and rolling element bearing applications. These materials are either hardened throughout the thickness of the part or they have a hardened exterior that progressively tapers into a softer core beneath the surface. The first type of material is called through-hardened and the second as case-hardened material. Case-hardening of steel is usually accomplished by the surface heat treatment method called carburization. Carburization of steel results in a material with gradients in microstructure and composition as a function of depth [123]. The affected region typically includes carbides surrounded by the steel matrix. The distribution of carbides varies with the depth; the region closer to surface has the higher density of carbides and it reduces with depth. Since carbide phase is much harder than surrounding steel matrix, their distribution results in a gradient in mechanical properties of the material. Klecka et al. [124] have extensively studied the relationship between the variations in mechanical properties and gradient in the subsurface microstructure of case-carburized steels. Depending on the type and time period of the carburization process, the gradient and the extent of the carburization i.e. depth of the affected region can vary.

A number of investigators (Branch et al.[125], Choi et al. [126]) have characterized the graded material properties of the hardened steel. Cahoon [127] investigated the relationship between hardness and yield and tensile strength of the steel. Pavlina and Tyne [128] have compiled hardness and strength values for different types of steel having wide range of compositions and microstructure from almost 20 years of experimental work. Using least-square regression analysis, they showed that there is a linear correlation between yield strength (S_y) and Vickers hardness (H_v).

$$S_y = -90.7 + 2.876 H_v \tag{4.1}$$

Where, yield strength is described in MPa and H_v has units of (Kg_f/mm^2).

To evaluate the variation of the hardness with depth due to the hardening process, Vickers hardness measurements were performed using micro-indentation tests at regular intervals on the cross-section of the case-carburized 8620 and through hardened 52100 steel components. 0.3 kgf of load was used for all tests. Figure 4.2 and Figure 4.3 demonstrate the measured variation of the hardness as a function of depth for through and case carburized material respectively. It can be noted that for through-hardened steel, the hardness is approximately constant throughout the depth; corresponding S_y calculated using Equation (4.1) is 2.4 GPa. On the other hand for case carburized steel, it closely follows a bilinear profile. Hardness is a maximum at the surface (S_y = 2.0 GPa) and it decreases linearly with depth in the carburized region and then it is approximately constant in the core region (S_y = 1.2 GPa). The distance from the surface where the carburized region ends is the case depth of that material. For this material, case depth is around 500μm. Klecka et al. [124] have also obtained similar type of distributions in their micro-indentation hardness measurements. In the current analysis, a constant hardness is assumed for through-hardened steel; while a bilinear hardness profile with different case-depths is assumed for the case carburized steel. The hardness profile of the steel is incorporated in the model by utilizing this linear relationship between hardness and yield stress. Therefore, the variation of yield strength with depth follows the same profile as hardness. For through-hardened material, the yield strength is set to 2 GPa throughout the depth. For better comparison, the maximum hardness at the surface of the case-carburized material is also set to 2 GPa whereas, the yield strength of the core material is assumed to be 1 GPa. Different case-depths change the slope of the decay of yield strength with depth. Figure 4.4 illustrates the different profiles of yield strength vs. depth studied in the current investigation. The depth has been non-dimensionalized by dividing with half Hertzian contact width, b. The finite elements in the simulation have been assigned the yield strength values depending on the y-coordinates of their centroids.

In addition to the hardness variation, case carburization introduces residual stresses (RS) in the material. Residual stresses play a decisive part in improving the rolling contact fatigue strength of the case carburized material [129]. Parrish and Harper [130] have surveyed around 70 RS distributions and results for carburized and hardened steels, where case depths were generally less than 1 mm. According to their results, the typical RS distribution is as shown in Figure 4.5. For majority of samples, the depth at which peak RS occurs was 20% of the case depth. The residual stress diminishes to zero at a depth equal to the case depth of the material. Figure 4.6 illustrates the RS distribution for different case depths used in this study. The value of RS at the surface and peak RS were fixed at -200 and -450 MPa respectively.

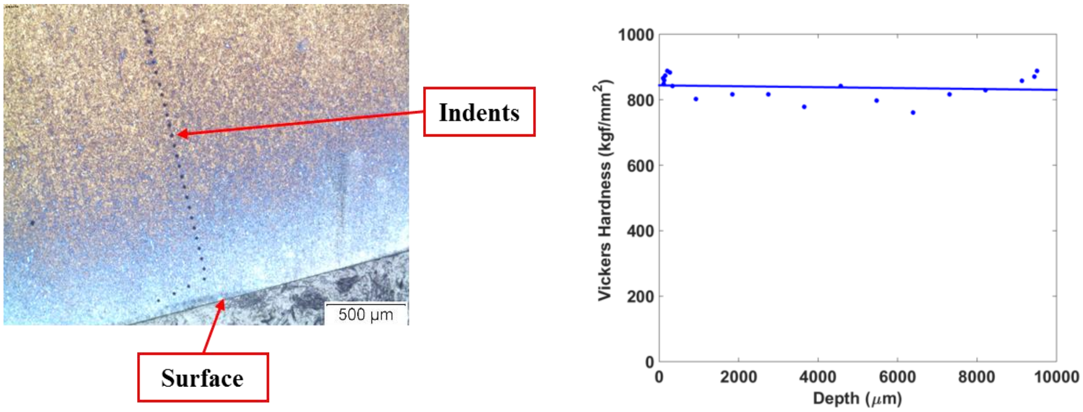

Figure 4.2: Vickers hardness measurements at different depths from the surface for a through hardened material.

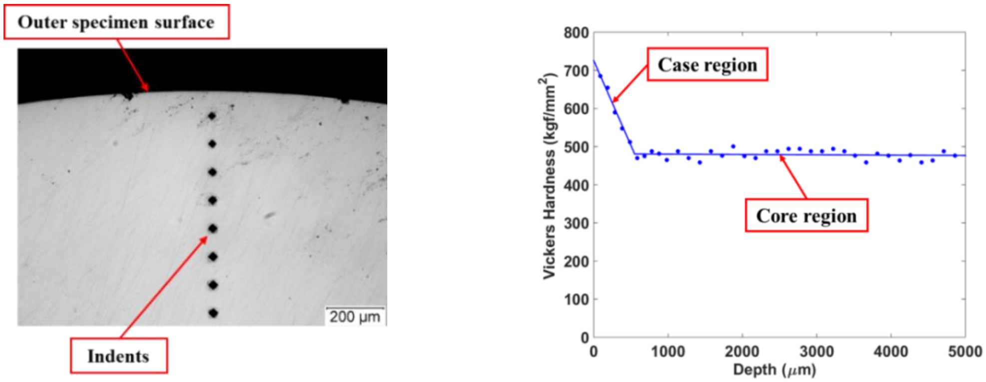

Figure 4.3: Vickers hardness measurements at different depths from the surface for a case carburized material.

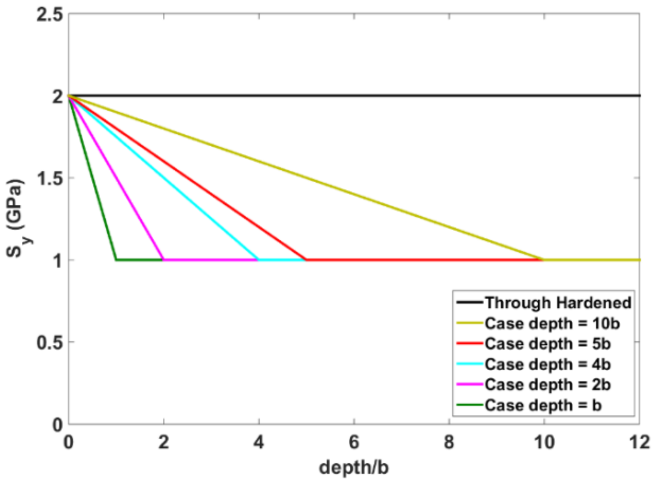

Figure 4.4: Profiles of yield strength vs. depth for case carburized steel with different case depths.

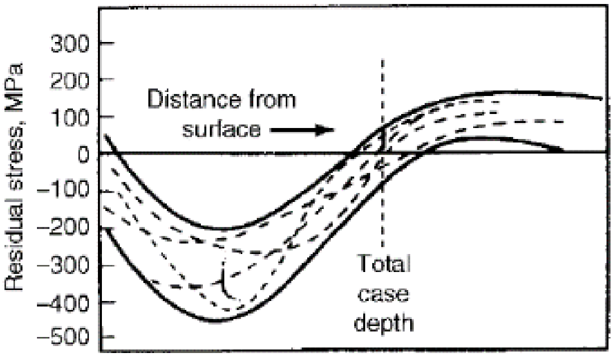

Figure 4.5: Typical residual stress distribution in case carburized steel [130].

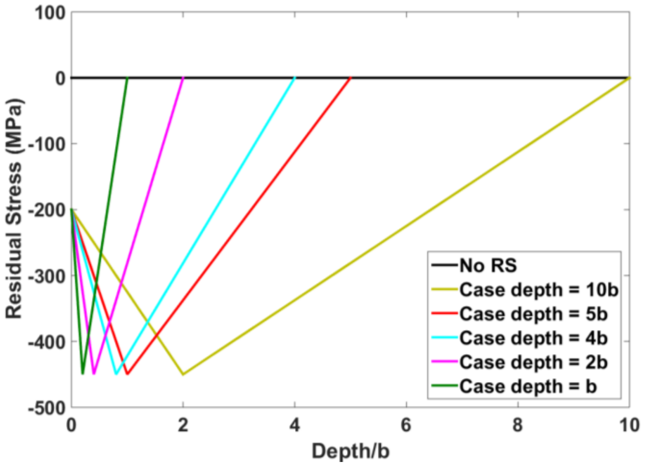

Figure 4.6: Profiles of residual stress vs. depth for case carburized steel with different case depths.

4.2.3 Simulation of a Rolling Pass

A finite element model was developed to simulate the line contact which usually arises between the roller and raceway in rolling element bearings. The line contact can be represented by a Hertzian loading on a semi-infinite half-space or explicitly modeled as two bodies in contact. In this analysis, the first approach has been used. Plane strain conditions are assumed. To allow for the reasonable computational time, the FEA domain is truncated as depicted in Figure 4.7. The dimensions for the half space model are listed in Table 4.1. The rolling pass is simulated by subjecting the half-space model to a sequence of surface tractions. The user subroutine UTRACLOAD is used to apply the Hertzian pressure as a non-uniform surface traction vectors. Equation (4.2) defines the normal component of the surface traction.

$$p_y(x) = P_{max}\sqrt{1-\left(\frac{(x-x_c)}{b}\right)^2} \tag{4.2}$$

Where, (x_c, y_c) is the coordinate of the center of the Hertzian pressure distribution; P_{max} is the magnitude of the pressure at the center; b is the half-contact width. The magnitude of the shear surface traction in the rolling direction is given by Equation(4.2) where μ_s is the coefficient of friction.

$$t_x(x) = \mu_s|p_y(x)| \tag{4.3}$$

In Equation (4.2) and Equation (4.2), (x, y) is the coordinate where the pressure is evaluated. A single rolling pass is modeled by sequentially applying pressure distribution defined by Equation (4.2) and Equation (4.2) over the half-space at 21 discrete locations from *-2.0b* to *2.0b* in the rolling direction. The discrete locations were uniformly spaced and were defined by changing the x-coordinate of the center, x_c. All displacements on the lower boundary of the model are fixed.

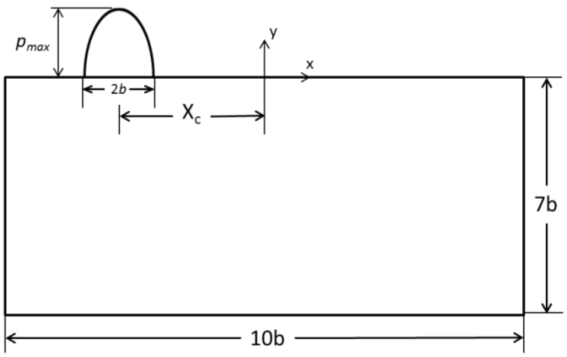

Figure 4.7: Computational domain used in FE simulation. The lower boundary of the domain is fixed in all directions.

4.2.4 Damage Coupled Elastic-plastic Constitutive Relations

An appropriate material model is required to correctly capture the stress-strain response of the rolling line contact. Due to the high localized compressive stress at the contact region, plastic deformation is often observed in rolling element bearings. Further, as described in section 2.2, hardening process affects the plastic response of the material. Therefore an elastic-plastic material model is needed to model the effect of hardness on rolling contact. AISI 52100 is the most widely used steel in rolling element bearings. Hahn et al. [131] suggested that the stress-strain response of AISI 52100 can be approximated as a linear elastic and linear kinematic hardening plastic (ELKP) material instead of the power law curve fit. This bi-linear representation simplifies the analysis by reducing the number of variables and enables us to emphasize on the effect of other parameters such as hardness and residual stress variation. Figure 4.8 shows a typical stress strain relationship for the ELKP material model. In the figure, E is the elasticity modulus; M is the linear hardening modulus. The details of the constitutive relationships for Mises plasticity model with linear kinematic hardening are provided in Warhadpande et al [33]. In this investigation, an extended ELKP material model is implemented to account for the material degradation due to cyclic loading (Warhadpande et al. [33] and Bomidi et al. [34]).

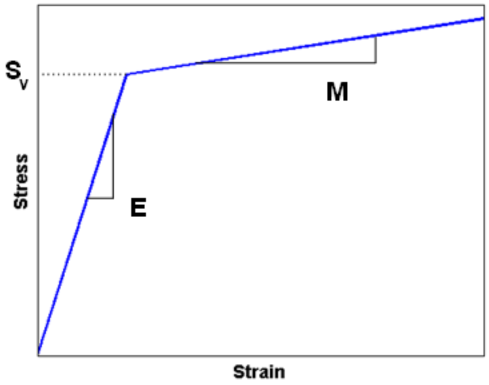

Figure 4.8: Typical stress-strain relationship for Linear Elastic-linear kinematic plastic (EKLP) material.

Damage due to cyclic loading is a process of material deterioration which manifests through the initiation and propagation of micro cracks and voids. The theory of continuum damage mechanics (Lemaitre [100], Kachanov [28]) has been widely used as a convenient framework to model these microscopic mechanisms of fatigue failure in an empirical fashion. The concept of damage mechanics defines a thermodynamic state variable, D to account for the progressive deterioration in material due to fatigue. For the most general elastic case, the damage variable is introduced into the material constitutive relations in the following form,

$$\sigma_{ij} = C_{ijkl}(I_{klmn} - D_{klmn})\epsilon_{mn} \tag{4.4}$$

Where, σ_{ij}, C_{ijkl}, D_{klmn}, ε_{mn} corresponds to the stress, stiffness, damage and strain tensors. It should be noted that, similar to stress and strain damage variable is also a tensor. However, under the assumption of isotropic damage and neglecting the effect of Poison's ratio on damage, the damage tensor reduces to a scalar quantity simplifying the Equation ((4.4) as follows:

$$\sigma = E(1 - D)\varepsilon \tag{4.5}$$

Where, E is the elasticity modulus for the undamaged material. In scalar case, the damage variable, D ranges from *0* for an undamaged or pristine material to *1* corresponding to completely damaged material. As the fatigue cycles progress, the internal damage manifests as the reduction in the effective modulus of elasticity. Thus, the above equations follow the effective stress concept in the damage mechanics; with the stress acting on the undamaged area satisfy the following constitutive relation:

$$\tilde{\sigma}_{ij} = \frac{\sigma_{ij}}{1-D} = C_{ijkl}\epsilon_{kl} \tag{4.6}$$

These principles of damage mechanics can also be applied to the elastic-plastic material behavior (Warhadpande et al. [33] and Bomidi et al. [34]). Thus, the damage variable was introduced in the Mises yield criterion for kinematic hardening. Accordingly, the yield function *f* was modified in the presence of damage as below:

$$f = (\tilde{\sigma} - \alpha)_{eq} - S_y \tag{4.7(a)}$$

$$(\tilde{\sigma} - \alpha)_{eq} = \sqrt{\frac{3}{2}\left(\frac{\sigma_{ij}^{D}}{1-D} - \alpha_{ij}\right)\left(\frac{\sigma_{ij}^{D}}{1-D} - \alpha_{ij}\right)} \tag{4.7(b)}$$

Where α is the backstress tensor which represents the center of the yield surface; S_y is the radius of the yield surface i.e. the yield strength; and σ^D is the deviatoric part of the stress tensor.

Similarly, the modified rate equations for plastic strain and kinematic hardening take the following form:

$$\dot{\epsilon}_{ij}^{p} = \dot{\lambda}\frac{\partial f}{\partial \sigma_{ij}} = \frac{\dot{\lambda}}{1-D}\left(\frac{\sigma_{ij}^{D}}{1-D} - \alpha_{ij}\right) \tag{4.8}$$

$$\dot{\alpha}_{ij} = -\hat{C}\dot{\lambda}\frac{\partial f}{\partial \alpha_{ij}} = \hat{C}\dot{\lambda}\left(\frac{\sigma_{ij}^{D}}{1-D} - \alpha_{ij}\right) \tag{4.9}$$

Here, $\dot{\lambda}$ is a plastic multiplier, and $\hat{C}$ is the scalar multiplier for hardening. A subroutine for user defined material (UMAT) is utilized in ABAQUS to implement this extended EKLP material model.

The evolution of damage variable at a material point is governed by a rate law according to the failure mechanism for the phenomenon in interest. For elastic material, the damage is only dependent on the state of stress. However, for elastic-plastic material undergoing yielding, then damage is dependent on the accumulated plastic strain as well as the state of stress. Therefore, the current model considers two different damage evolution laws in the constitutive damage modeling, each for high and low cycle fatigue. As mentioned earlier, in the case of rolling contact fatigue, the shear component of the state of stress is the one undergoing reversal during a rolling pass. Further, the presence of compressive normal stresses hinders crack opening and makes the mode II crack growth dominate. Therefore, the reversal in shear stress is considered to be the critical stress component that promotes the failure (Littman [2], Lundberg and Palmgren [11]). To account for the variability in fatigue life due to randomness in material microstructure, it is assumed that Voronoi grain boundaries are the "weak planes" along which the fatigue damage advances (Raje et al. [27], Jalalahmadi et al. [30], and Slack et al. [97]). Thus, in the current model the stress and the strain field are resolved along the grain boundary (Figure 4.9).

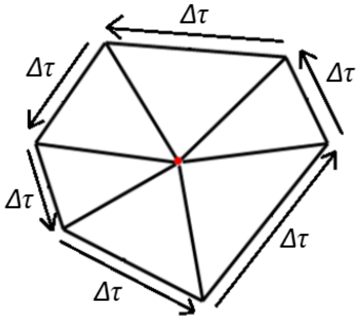

Figure 4.9: Voronoi cell divided into Voronoi elements and stresses resolved along the grain boundaries.

For the elastic case, the damage evolution law utilizes maximum shear stress reversal $\Delta\tau_{critical}$ along the Voronoi grain boundary as the damage causing stress. Shen et al. [132] derived the damage rate law to include the effect of the mean stress due to the presence of residual stresses. The damage evolution law for modeling RCF therefore becomes [30], [97], [132];

$$\frac{dD}{dN} = \left[\frac{\Delta\tau_{critical}}{\tau_{ro}\left(1-\frac{\sigma_m}{S_{us}}\right)(1-D)}\right]^m \tag{4.10}$$

The damage law for plastic case (Lamaitre [100]) considers maximum Von Mises stress ($\sigma_{\max}$) over a rolling pass and accumulated plastic strain over a fatigue cycle ($\dot{p}$) resolved along grain boundary.

$$\frac{dD}{dN} = \left[\frac{\sigma_{\max}^2}{2ES_0\left(1-\frac{\sigma_m}{S_{us}}\right)^2(1-D)^2}\right]^q \dot{p} \tag{4.11}$$

Here, E is the modulus of elasticity for pristine material. τ_{r0} and S_0 are the material parameters that characterizes the material's resistance to fatigue damage. σ_m represents the mean stress due to the presence of residual stresses and S_{us} is the ultimate strength in shear.

4.2.5 Evaluation of Damage Parameters

The elastic and plastic damage rate laws given in Equations (4.10) and (4.11) introduced two new material parameters each. These parameters need to be determined experimentally. In this study, these parameters are extracted from the torsional fatigue stress-life (SN) data. The choice of torsion fatigue experiments is valid because the mechanism for damage accumulation for both torsion fatigue and rolling contact fatigue is shear stress driven. Thus, it can be presumed that failure mechanisms for both phenomena are equivalent. Figure 4.10 illustrates the torsion SN results for bearing steel JIS SUJ2 (AISI 52100 variant) from [133]. Applying power law fit, fatigue strength coefficient (τ_f') and fatigue strength exponent (b) for the Basquin's law can be obtained. Note that there is no mean stress due to residual stress for this torsion SN curve.

$$\begin{aligned} \Delta\tau &= \tau_f' {N_f}^{b} \\ \tau_f' &= 2.39\ GPa\ and\ b = -0.09 \end{aligned} \tag{4.12}$$

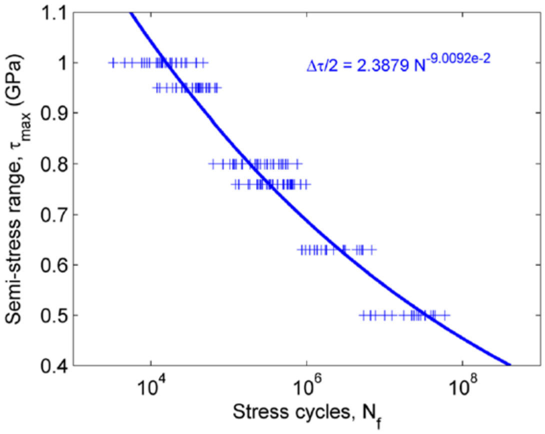

Figure 4.10: Experimental S-N data for through hardened bearing steel JIS SUJ2 (AISI 52100 variant) in completely reversed torsional fatigue [133] and power law fit to the data.

Integrating the elastic damage rate law (Equation 4.10) from undamaged state (N=0 and D=0) to fully damaged state ($N = N_f$ and $D = 1$) and with no mean stress due to residual stress:

$$N_f = \frac{1}{m+1}\left(\frac{\tau_{r0}}{\Delta\tau}\right)^{m} \rightarrow \Delta\tau = \frac{\tau_{r0}}{(m+1)^{1/m}} N_f^{-\frac{1}{m}} \tag{4.13}$$

Since Equation (4.12) and (4.13) are equivalent, we can obtain the elastic damage parameters in terms of Basquin's parameters.

$$m = -\frac{1}{b} \quad and\ \tau_r = 2\tau_f'\left(1-\frac{1}{b}\right)^{-b} \tag{4.14}$$

Similar procedure was used to evaluate the plastic damage parameters, S_0 and q (Lemaitre [100]). Integrating the plastic damage rate law (Equation (4.11) and with no mean stress due to residual stress:

$$\sigma_{max} = \sqrt{3}\left(\frac{\Delta\tau}{2}\right) = \frac{(2ES_0)^{\frac{1}{2}}}{\left(2(2q+1)\Delta\epsilon_p\right)^{1/2q}} N_f^{-1/2q} \tag{4.15}$$

Equating Equation (4.12) and (4.15), we obtain;

$$\sqrt{3}\left(\tau_f' N_f{}^{b}\right) = \frac{(2ES_0)^{\frac{1}{2}}}{\left(2(2q+1)\Delta\epsilon_p\right)^{1/2q}} N_f^{-1/2q} \tag{4.16}$$

Here, $\Delta\epsilon_p$ is the range of plastic strain corresponding to σ_{max} through the cyclic stress-strain behavior over one fatigue cycle. $\Delta\epsilon_p$ can be expressed in term of σ_{max} and yield strength S_y by considering the hardening modulus M (Figure 4.11):

$$\Delta\epsilon_p = 2\left(\frac{\sigma_{max} - S_y}{M}\right) \tag{4.17}$$

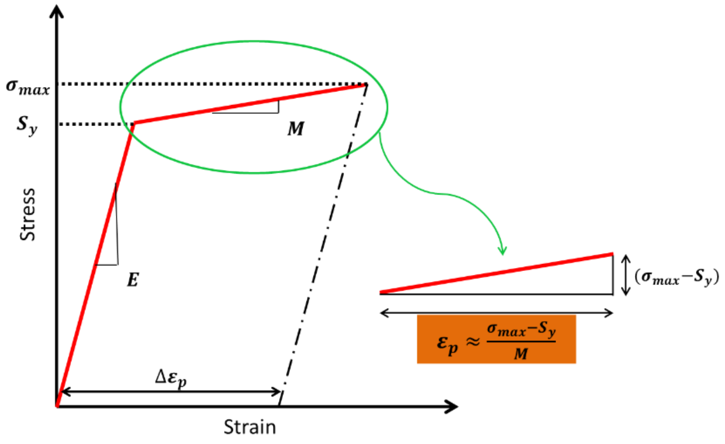

Figure 4.11: Equation to calculate accumulated plastic strain $\boldsymbol{\Delta\epsilon_p}$ during low cycle fatigue.

Since, plastic strain is observed in the fatigue process during low cycle fatigue regime; two different values for N_f $(N_1 = 10\ and\ N_2 = 1000)$ were selected from this portion of SN curve. Substituting in Equation (4.16),

$$\sqrt{3}\left(\tau_f' {N_1}^b\right) = \frac{(2ES_0)^{\frac{1}{2}}}{\left(2(2q+1)\Delta\epsilon_{p1}\right)^{1/2q}}\ N_1^{-1/2q} \tag{4.18(a)}$$

$$\sqrt{3}\left(\tau_f' {N_2}^b\right) = \frac{(2ES_0)^{\frac{1}{2}}}{\left(2(2q+1)\Delta\epsilon_{p2}\right)^{1/2q}}\ N_2^{-1/2q} \tag{4.18(b)}$$

Dividing Equation (4.18(a)) by (4.18(b)) to eliminate *S₀* and rearranging the equation, we obtain

$$q = -\frac{ln\left(\frac{N_2\Delta\varepsilon_{p2}}{N_1\Delta\varepsilon_{p1}}\right)}{2b\ ln\left(\frac{N_2}{N_1}\right)} \tag{4.19}$$

The value of S_0 can be obtained by substituting q into either (4.18(a)) by (4.18(b)).

The material used for above experiments was through-hardened with yield strength of 2 GPa. As discussed earlier, the process of hardening causes changes in the yield strength of the material. Consequently, the SN behavior of the material would also get affected by the hardening process. In this study, it was assumed that for the same material i.e. with same chemical composition fatigue strength coefficient (τ_f') change linearly with hardness and hence with yield strength (Equation (4.1)). However, the slope of the SN curve i.e. fatigue strength exponent (b) does not change with respect to the hardness.

$$\tau_f' \ \propto\ H_v\ \propto S_y \tag{4.20}$$

Figure 4.12 depicts the original SN curve [133] for $S_y = 2$ GPa along with the few other SN curves for yield strength varying from 2 GPa to 1 GPa generated using the above assumption. The damage parameters τ_{r0} and S_0 are dependent on the fatigue strength coefficient (τ_f'). Hence, τ_{r0} and S_0 also vary with respect to the yield strength. This variation is demonstrated in Figure 4.13. However, the exponents, m and q in the damage rate law depend only on the fatigue strength exponent (b). Therefore, they do not change with yield strength.

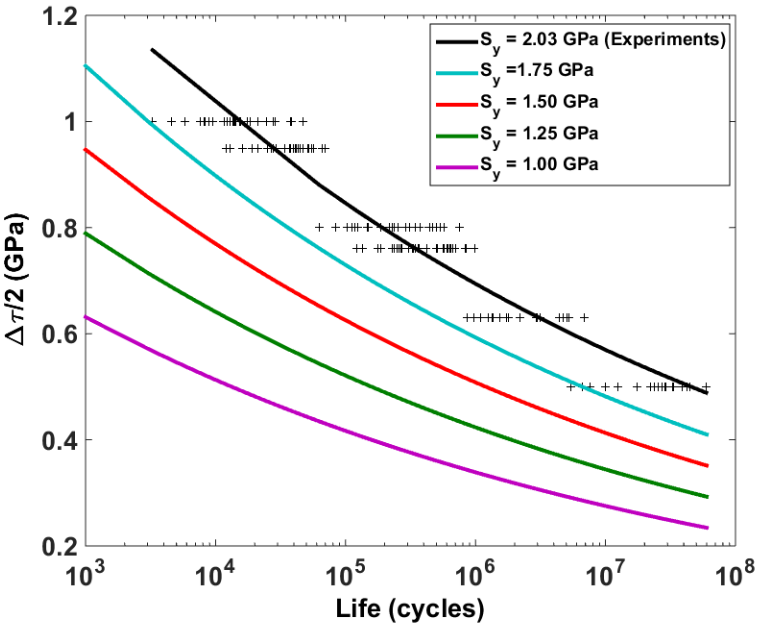

Figure 4.12: Analytically generated torsional SN curves for bearing steel with different yield strength values. The experimental SN curve from [133] is also shown for comparison.

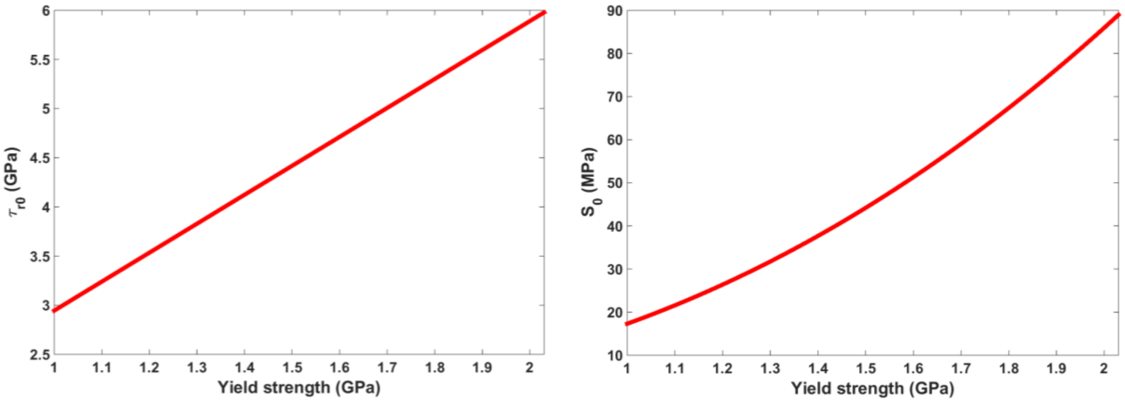

Figure 4.13: Variation of damage parameters τ_{r0} and S_0 with change in yield strength.

4.2.6 Numerical Implementation

To implement the damage mechanics based fatigue modeling, damage coupled material constitutive equations and damage evolution laws (Equation (4.4) - (4.11)) need to be solved simultaneously for each element to update its damage and the elasticity modulus. However, this iterative process cannot be employed after every load pass since evaluating the stress-strain relations using the finite element model becomes computationally impossible because of the large number of the fatigue cycles (more than billions for high cycle fatigue). Therefore, a solution strategy referred as the 'jump-in cycles' procedure developed by Lemaitre [100] was used in the previous and current RCF investigations [30], [97] to make the solution tractable. This approach assumes that the state of stress and the accumulated plastic strain histories for each element in the domain remains constant ΔN^i, in a block i. During this block of cycles, damage for each element is also assumed to remain constant. Thus, damage evolution is piecewise linear with respect to the block of cycles. Current stress field and accumulated plastic strain is found for each block of cycles by using the material constitutive relations and damage obtained from the previous block of cycles. Both damage evolution rates (Equations (4.10) and (4.11)) is concurrently evaluated for each element in the domain and the greater of the two is used to update the damage for that element. Note that, the yield strength (S_y) and mean stress due to residual stress (σ_m) values are assigned to each finite element as per its depth from the surface as described in section 2.2 (Figure 4.4 and Figure 4.6). Thus, the damage parameters τ_{r0} and S_0 also vary for different elements depending on the depth (Figure 4.13). A constant damage increment ΔD over that number of cycles is prescribed for the element which has largest damage evolution rate per cycle. The numbers of cycles in the current block are calculated by dividing ΔD by the maximum damage evolution rate. The step by step algorithm used in this investigation is provided by Warhadpande et al. [33]. Please note that the stress range and accumulated plastic strain is computed for the stabilized stress-strain loop. Once the damage for an element reaches 1 i.e. the critical damage value, the fatigue damage is assumed to be initiated. In this study, a kill element formulation developed by Slack and Sadeghi [97] has been used for damage propagation. In this formulation, the simulation continues with the completely damaged elements having state of damage equal to 1, until another element fails. Therefore, the completely damaged elements will have zero stiffness and act as voids in the simulation domain. This method allows damage to propagate continuously through the material microstructure. Moreover, in the kill element approach, the internal interfaces in the material do not come into direct contact. Thus, the internal interfaces are implicitly frictionless. The simulation ends when the damage propagates to the surface and forms a spall.

4.3 Results and Discussion

This section describes results obtained from the elastic-plastic finite element model for sub-surface initiated spalling in the cylindrical roller bearing made from through-hardened and case carburized bearing steel with different case depths. Table 4.2 summarizes the parameters and material properties used in this simulation. Typical size of the contact region between rollers and raceway of the cylindrical roller bearing can be of the order of a hundred microns depending on the bearing size. In this study, the half-width of contact was kept fixed at 100 µm for all cases. The grain diameters, d_g, in the order of 10µm are generally observed in bearing steels. Thus, average size of the Voronoi cells was controlled to be 10µm during Voronoi tessellation procedure to construct random microstructure domains to investigate variability in fatigue lives due to subsurface microstructure topology. Maximum Hertzian pressure, P_{max} was varied from 2.0 GPa to 3.5 GPa so that considerable portion of the material would undergo plastic deformation. The traction coefficient, μ_s in Equation (4.3), however was set at 0.05 which is a representative of lubricated rolling-sliding contact conditions. Experimental measurements using twin-disk test rig by Mihallidis et al. [134], [135] suggest that 0.05 is a reasonable traction coefficient for elastohydrodynamically lubricated bearing contacts. Further, many analytical investigations [33], [34], [97], [107] also use this value in their model. Klecka, et al. [124] has shown that the elastic modulus, (E) of the carburized material can vary +/- 20 GPa in the case region which they attributed to the high number of carbides and elevated carbon concentration in the matrix. Since, the variation in E is small compared to the variation in S_y and residual stress, the effect of carburization on elasticity modulus is neglected in this work.

Table 4.2: Material properties used in the simulation.

Undamaged elasticity modulus, E	200 GPa
Hardening modulus, M	10 GPa
Poisson's ratio, v	0.3
Material grain diameter, d_g	10 μm
Maximum Hertzian pressure, p_{max}	2.0-3.5 GPa
Contact half-width, b	100 μm
Surface coefficient of friction, μ_s	0.05
Critical damage value, D_{crit}	1

4.3.1 Effect of Hardness on Stress Solution

The effect of the hardening process on the sub-surface stress field for Hertzian loading conditions is examined in this section. For this purpose, Hertzian pressure profile was applied to center of top surface by setting the value of x_c to be 0 in Equation (4.2) and the sub-surface stresses along the center line of the contact were studied. Figure 4.14 illustrates the maximum in plane shear stress, τ_{xy}/P_{max} vs. non-dimensional depth for P_{max} = 2.0, 2.75 and 3.5 GPa. The maximum shear stress is defined as one-half of the maximum difference between two principal stresses.

Analyzing the maximum in-plane shear stress (τ_{xy}) plots in Figure 4.14, we can infer that as the case depth increases, the depth at which maximum τ_{xy} occurs also increases. The cause of this phenomenon is the presence of softer material near to the surface for lower case depths. However, when yielding does not occur, the shear stress profile coincides with the through hardened case irrespective of the case depth. This can be observed for P_{max} = 2.75 GPa, for which the plots for case depths more than 4b coincide with that of through hardened material.

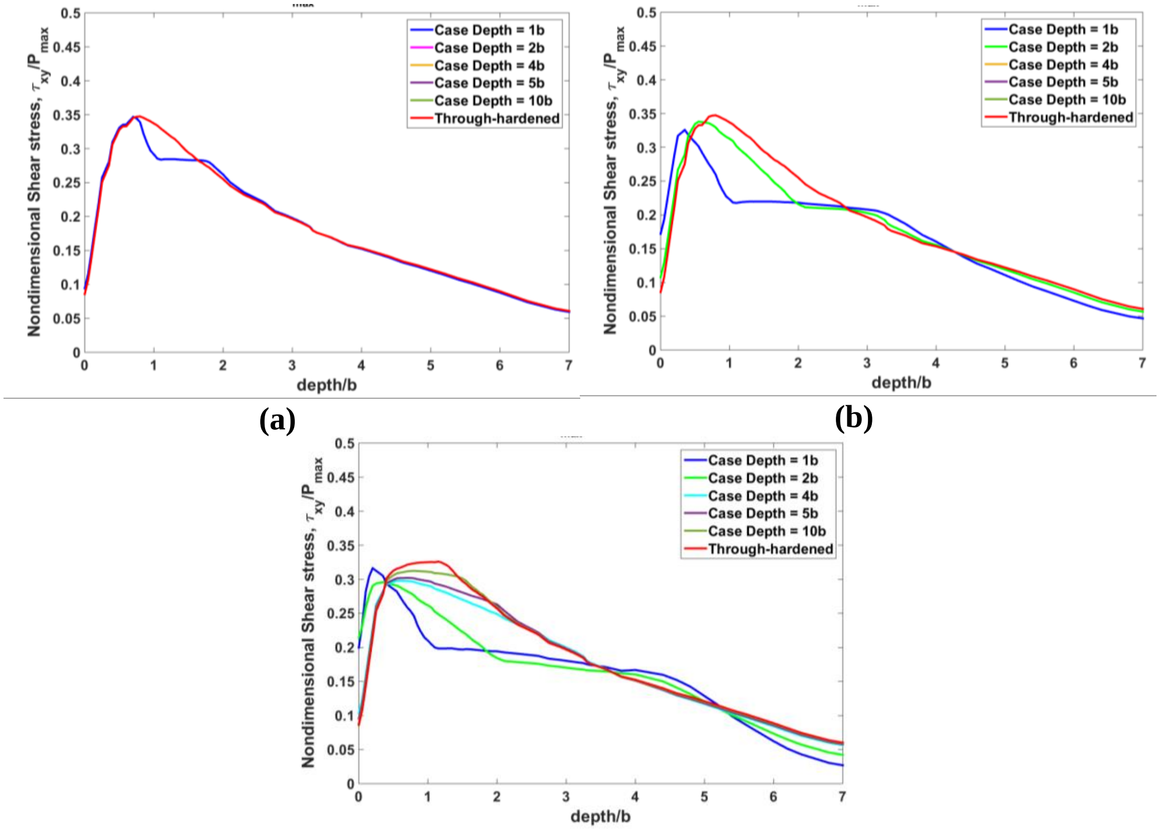

(a) **(b)**

(c)

Figure 4.14: Variation of non-dimensional shear stress with for (a) P_{max} = 2GPa, (b) P_{max} = 2.75GPa and (c) P_{max} = 3.5GPa.

4.3.2 Parametric Study

In this section, rolling contact fatigue lives obtained for different operating conditions are analyzed. 35 random material domains were simulated for each operating condition. A 2 parameter Weibull cumulative distribution function was used to determine the variability in the fatigue lives for different residual stress and yield strength. Two of the more important parameters obtained from the Weibull plots are the Weibull slope and L_{10} life. The slope of the line for Weibull distribution provides a measure for the scatter present in the fatigue life data. Smaller Weibull slopes indicate more scatter in the data. L_{10} life describes the probability of survival. It is the number of load cycles that 90% members of the population can be expected to survive.

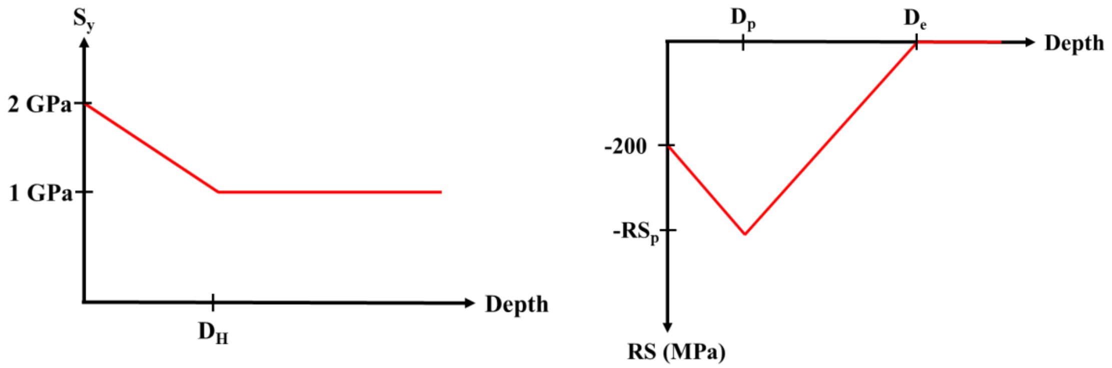

Figure 4.15: Yield strength and residual stress distribution as a function of depth.

Figure 4.15 illustrates the general trend for yield strength and residual stress distribution as a function of depth used in the parametric study. In the figure, D_H is the case hardness depth; D_p is the depth at which the peak residual stress occurs, while residual stress goes to 0 at depth D_e from the surface. RS_p is the value of peak compressive residual stress. Different scenarios were investigated to analyze the effects of these parameters. In scenario 1, the case hardness depth (D_H) was varied as illustrated in Figure 4.16(a) but without any residual stress in the material. Figure 4.17 depicts the Weibull probability results for various case depths at P_{max} = 2.0 and 3.5 GPa respectively. It can be noted that for a fixed load, as the case depth of the material increases the L_{10} life for RCF also increases. Through hardened material has the longest L_{10} life for all load levels. This is as expected from the model since the damage parameters τ_{r0} and S_0 increases with the fatigue strength coefficient (τ_f') which is evident in Figure 4.13. Further, τ_f' is directly proportional to the yield strength (Equation (4.21)). Since τ_{r0} and S_0 represents the fatigue resistance of the material, it can be concluded that highest yield strength corresponds to higher fatigue resistance. It can also be observed from Figure 4.4 that through-hardened steel has the highest yield strength at all depths compared to the case carburized steels. Therefore, through-hardened material will exhibit longer life as is the limiting criteria for fatigue.

For scenarios 2 through 5, the yield strength was kept constant at 2 GPa throughout the depth of the domain. Therefore, D_H is infinity, similar to the through hardened material. In scenario 2, the depth at which the peak residual stress occurs (D_p) is varied keeping other parameters fixed, as shown in Figure 4.16 (b). From the Weibull probability results depicted in the Figure 4.18, we can conclude that the residual stress distribution enhances the RCF life. Further, the fatigue life is proportional to the residual stress value at the critical depth. At low loads (P_{max} = 2 GPa), the elastic damage law is dominant and the main mode of failure. Therefore the critical depth occurs at 0.5b below the surface where shear stress reversal is the maximum. On the other hand, at high load (P_{max} =3.5 GPa), the fatigue life is governed by the plastic damage law. Since, Von-Mises stress is the maximum at a depth 0.7b below the surface, which is the critical depth for high loads. In both cases, the compressive residual stress at the critical depth was the highest for D_p of 40µm and it had the largest RCF life. In scenario 3, the value of peak residual stress (RS_p) was varied while D_p was kept fixed at 50µm (Figure 4.16 (c)). It can be observed in Figure 4.19 that as RS_p increased the fatigue life also increase. In scenario 4 as demonstrated in Figure 4.16 (d), D_e was varied but D_p was kept fixed at 100µm so that the residual stress at the critical depth would remain the same for all cases. As expected the fatigue life for all cases were the same (Figure 4.20). Scenarios 3 and 4 confirm that when the yield strength is not varied with depth, the fatigue life was governed by the residual stress value at the critical depth.

Scenario 5, illustrated in Figure 4.16 (e) resembles the residual stress distribution typically observed in case carburized steel. The peak residual stress occurred at 20% of the D_e. Weibull probability plots obtained from the model for this scenario are depicted in Figure 4.21. The scenario with residual stress depth (D_e) of 200 µm found to have largest RCF life at low load however at high load D_e of 400 µm had the largest life. This is because the critical depth for high load was deeper into the material. It can be noticed from the model results for parametric study that while the gradient in hardness (so the yield strength) in case carburized steel diminishes the fatigue strength, the presence of residual stress in the material enhances the fatigue life. The right balance between these two competing phenomena would yield the largest RCF life.

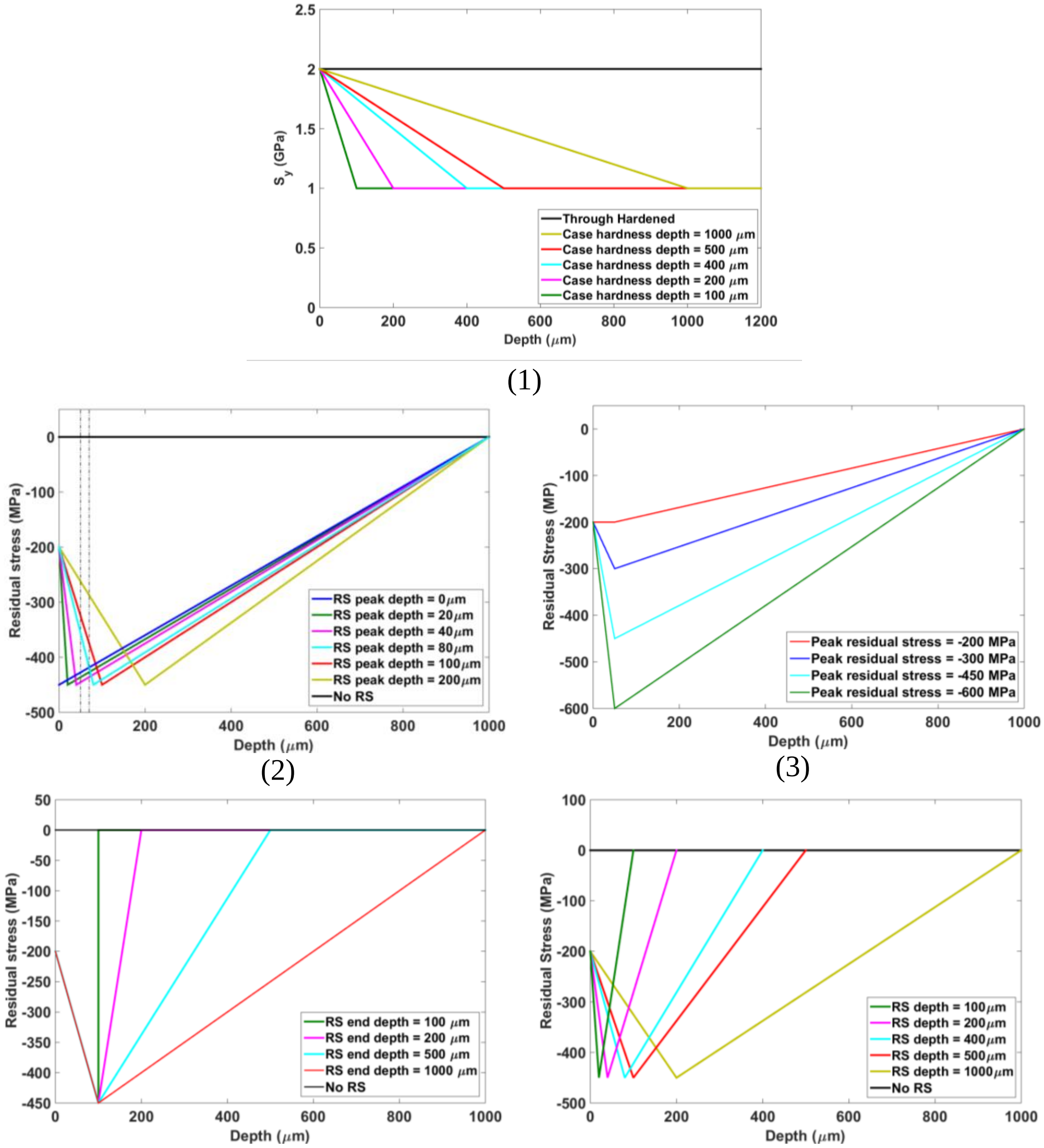

(1)

(2)

(3)

(4)

(5)

Figure 4.16: Different yield strength and residual stress profiles (scenarios) considered for parametric study.

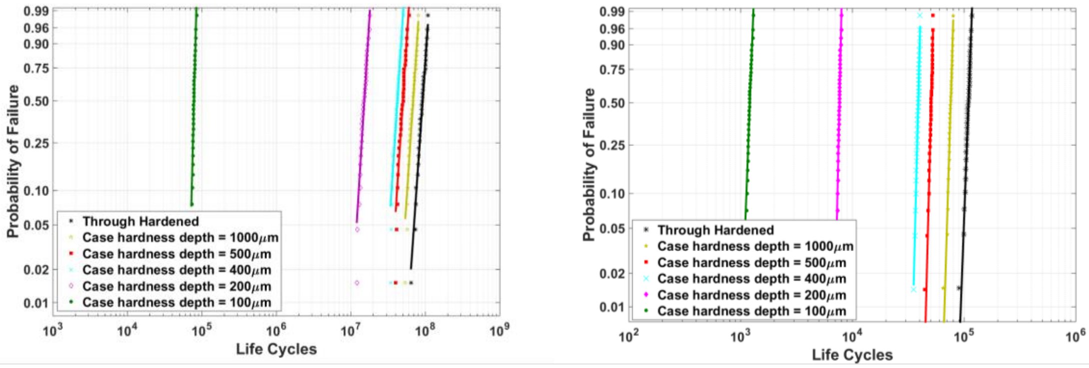

(a) (b)

Figure 4.17: Weibull probability plots for test scenario 1 at (a) P_{max} = 2.0 GPa and (b) P_{max} = 3.5 GPa.

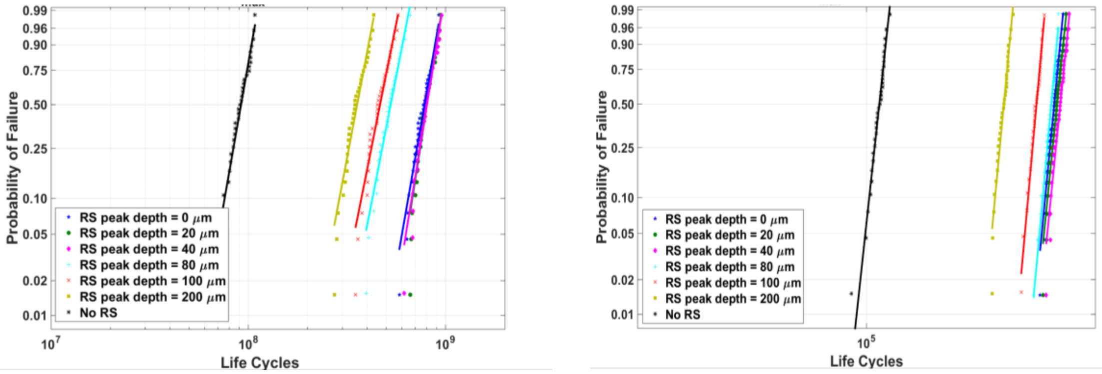

(a) (b)

Figure 4.18: Weibull probability plots for test scenario 2 at (a) P_{max} = 2.0 GPa and (b) P_{max} = 3.5 GPa.

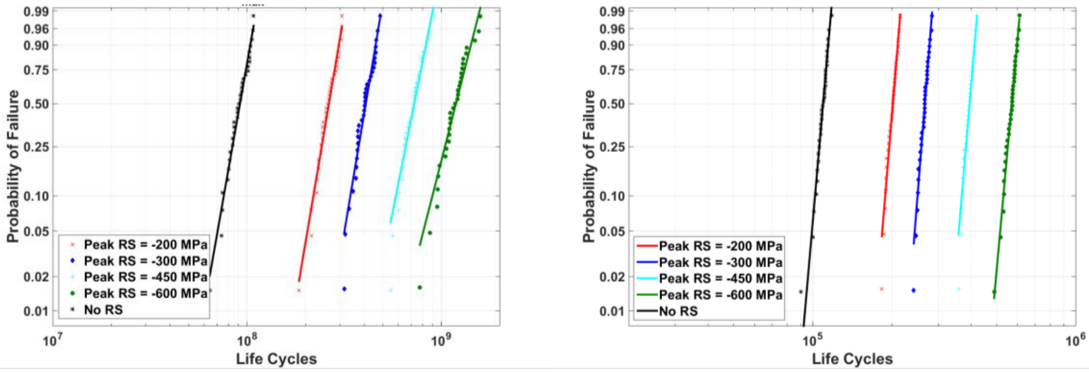

(a) (b)

Figure 4.19: Weibull probability plots for test scenario 3 at (a) P_{max} = 2.0 GPa and (b) P_{max} = 3.5 GPa.

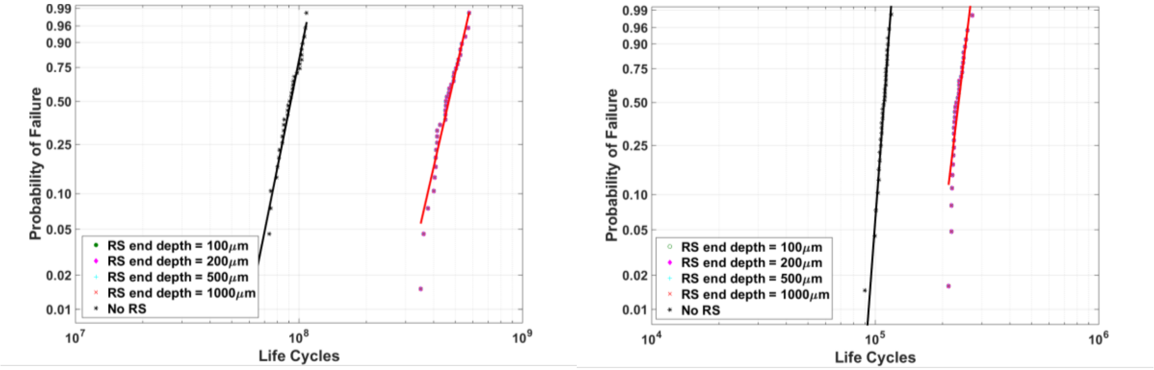

(a) (b)

Figure 4.20: Weibull probability plots for test scenario 4 at (a) P_{max} = 2.0 GPa and (b) P_{max} = 3.5 GPa.

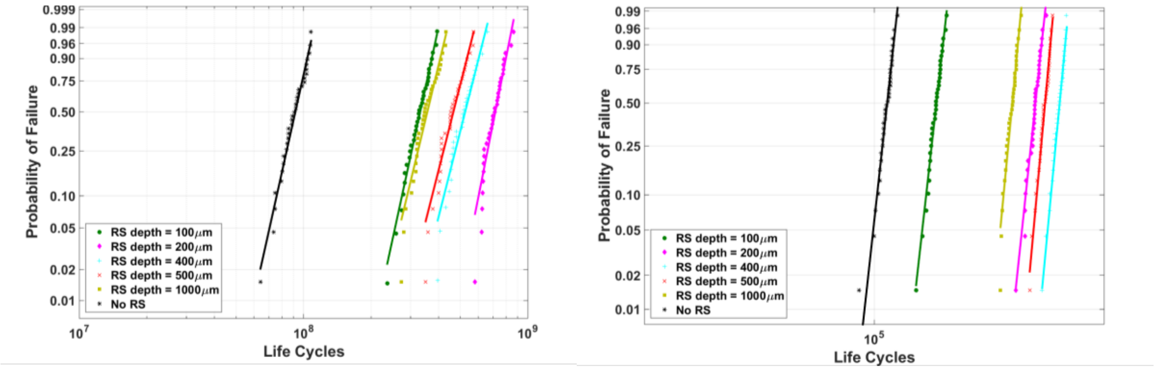

(a) (b)

Figure 4.21: Weibull probability plots for test scenario 5 at (a) P_{max} = 2.0 GPa and (b) P_{max} = 3.5 GPa.

To analyze the combined effect of yield strength and residual stress as it occurs in case carburized steel, the model was simulated with yield strength and residual stress profiles shown in Figure 4.4 and Figure 4.6 respectively. Figure 4.22 depicts the comparison of RCF lives for case carburized steel with case depths of 1b, 2b, 4b, 5b and 10b and the through hardened steel. The Weibull slopes and L_{10} lives obtained from the model are listed in Table 4.3. The combined effect of yield strength and residual stress leads to the largest RCF life for case depth of 4b at P_{max}= 2 GPa and 5b at P_{max}= 3.5 GPa.

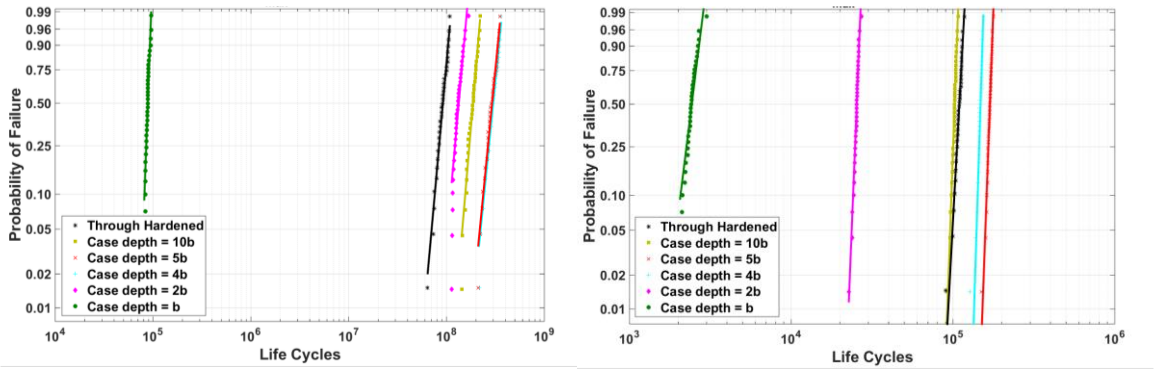

(a) (b)

Figure 4.22: Weibull probability plots for case carburized steel with different case depths at (a) P_{max} = 2.0 GPa and (b) P_{max} = 3.5GPa.

To quantify the effects of the different parameters on the RCF lives, a modifying factor β was defined as the ratio of L_{10} lives for the test case (L_{10c}) and through hardened steel (L_{10t}) at the same load level.

$$\beta = \left[\frac{L_{10c}}{L_{10t}}\right]_{P_{max}} \tag{4.21}$$

From the results of the parametric study, it is clear that modifying factor β is a function of case hardness depth (D_H) and the value of compressive residual stress at the critical depth, S_{RS}. Please note that S_{RS} has to be calculated from the parameters D_e, D_p, RS_p and the critical depth for the applied load. The case hardness depth can be normalized by the contact half-width (b) and residual stress can be normalized with applied maximum Hertzian pressure (P_{max}).

$$\beta = f\left(\frac{b}{D_H}\right) g\left(\frac{S_{RS}}{P_{max}}\right) \tag{4.22}$$

The modifying factor β was calculated from the L_{10} lives obtained from the model results of parametric study at all load levels. The function f is evaluated by curve fitting the modifying factor obtained from scenario 1, while function g is evaluated by the results of test scenarios 2 through 5. Figure 4.23 demonstrates the modifying factor against the normalized case hardness depth (D_H) and residual stress at critical depth (S_{RS}) with the curve fit equations. Therefore, from the parametric study we can derive the following equation for the modifying factor

$$\beta = \left(1.61\left(\frac{b}{D_H}\right)^2 - 2.58\left(\frac{b}{D_H}\right) + 0.98\right)\left(184.97\left(\frac{S_{RS}}{P_{max}}\right)^2 - 4.10\left(\frac{S_{RS}}{P_{max}}\right) + 1.17\right) \tag{4.23}$$

Table 4.3: Predicted Weibull slopes and L_{10} lives for case carburized steel.

	P_{max} (GPa)	Core Depth (μm)	Weibull Slope	L_{10} Life
Case carburized	2.00	1b	23.95	8.17E+04
Case carburized	2.00	2b	9.87	1.10E+08
Case carburized	2.00	4b	8.85	2.42E+08
Case carburized	2.00	5b	9.02	2.37E+08
Case carburized	2.00	10b	10.36	1.55E+08
Through Hardened	2.00	Infinity	9.83	7.58E+07
Case carburized	3.50	1b	11.7	2.07E+03
Case carburized	3.50	2b	36.22	2.41E+04
Case carburized	3.50	4b	45.99	1.42E+05
Case carburized	3.50	5b	40.04	1.61E+05
Case carburized	3.50	10b	40.2	9.77E+04
Through Hardened	3.50	Infinity	26.77	1.02E+05

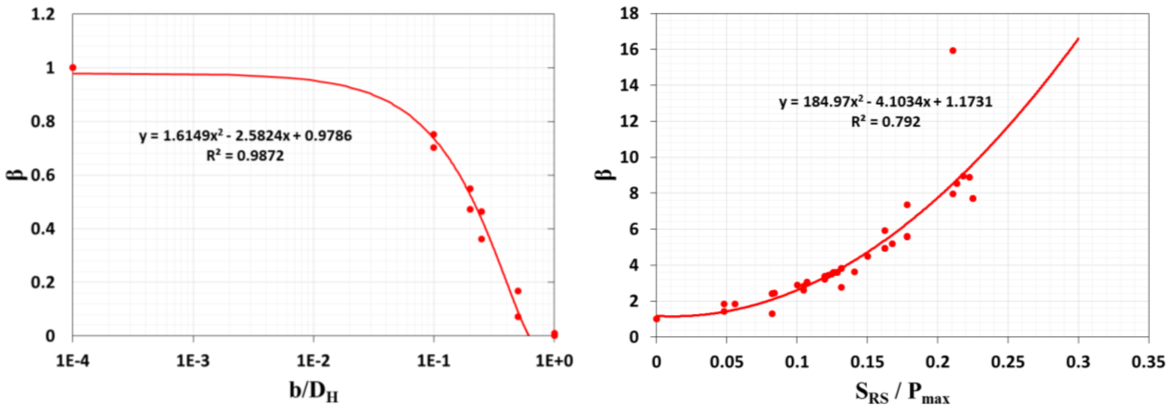

(a) (b)

Figure 4.23: The modifying factor $\boldsymbol{\beta}$ obtained from model results of parametric study plotted against (a) the normalized case hardness depth, (b) residual stress at critical depth (S_{RS}).

4.3.3 Effect of Case Carburization on RCF Lives

The optimized case depth for the case carburized steel which will provide largest RCF strength can be obtained from the Equation (4.23). From Figure 4.4 and Figure 4.6, we know that for case carburized material case hardness depth (D_H) is equal to the RS depth (D_e) and depth of peak residual *stress* (D_p) is 20% of RS depth (D_e). Substituting these relations and 450 MPa for peak compressive residual stress in Equation (4.23), the modifying factor (β) is plotted against case depth in Figure 4.24. The maximum β occurs at case depth of 6.2b for P_{max}= 2 GPa and 7.6b for P_{max}= 3.5 GPa.

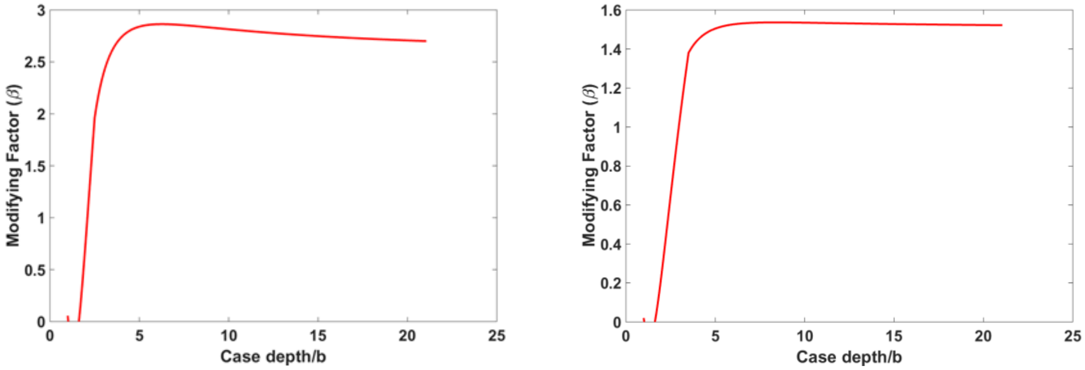

(a) **(b)**

Figure 4.24: Variation of modifying factor $\boldsymbol{\beta}$ with case depth of a case carburized steel as per Equation (4.23) for (a) P_{max} = 2 GPa and (b) P_{max} = 3.5 GPa.

4.3.4 Effect of Case Carburization on Spall Patterns

Figure 4.25 illustrate the typical spall patterns observed in the results obtained in this study at P_{max} = 2.75 GPa for different case depths. It can be stated from the figure that spalls initiated deeper in the domain for lower case depths and as the case depth increases the initiation occurred at around 0.5b below the surface, which is the location of maximum shear stress reversal for elastic material. Please note that the location of damage initiation depends on the combined effect of shear stress reversal ($\Delta\tau_{critical}$), Von Mises stress ($\sigma_{\max}$) and damage parameters τ_{r0} and S_0, which are all functions of depth. This is evident from the damage evolution laws of Equations (4.10) and (4.11). For low case depths, plastic damage rate law is dominant, and Equation (4.11) governs the damage initiation, while for higher case depths, material does not yield and initiation occurs according to maximum shear stress reversal.

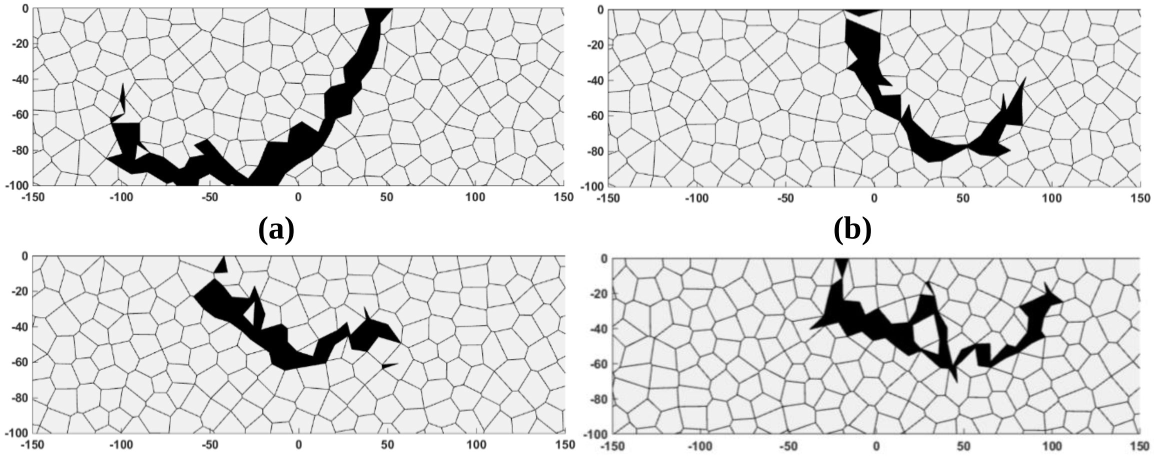

(a) **(b)**

(c) **(d)**

Figure 4.25: Typical spall patterns obtained from the model at P_{max} = 2.75 GPa for (a) Case depth = 2b, (b) Case depth = 4b, (c) Case depth = 10b, (d) Through Hardened.

4.3.5 Effect on Initial Flaws

Experimental fatigue data for steel shows significant amount of scatter, Weibull slopes in the range of 0.51 to 5.7 (Harris and Barnsby [115]). However, the Weibull slopes for RCF lives obtained from the model results are considerably higher. One possible reason for this discrepancy could be because the model assumes homogeneous material without any voids or inclusions. In fact, the steel cleanliness has a strong influence on rolling contact fatigue [116]. Analysis of fractured surface often finds that cracks initiate around the inhomogeneities in the material. The random distribution of these material defects leads to reduction in fatigue lives and increase in the scatter. Therefore, in this section the effect of distribution of initial internal voids on the RCF lives is explored. An initial void was introduced by setting the elasticity modulus of a random Voronoi element equal to zero. The random Voronoi element was selected from the microstructure topology region i.e. $-b < x < b$ and $-1b < y < 0$. Figure 4.26 illustrates an initial void and its random placement in the domain. The sizes of the initial voids correspond well with the experimentally observed range for inclusions in bearing steel [117]. Note that, initial voids were not allowed to occur on the surface as that signifies the end of the simulation.

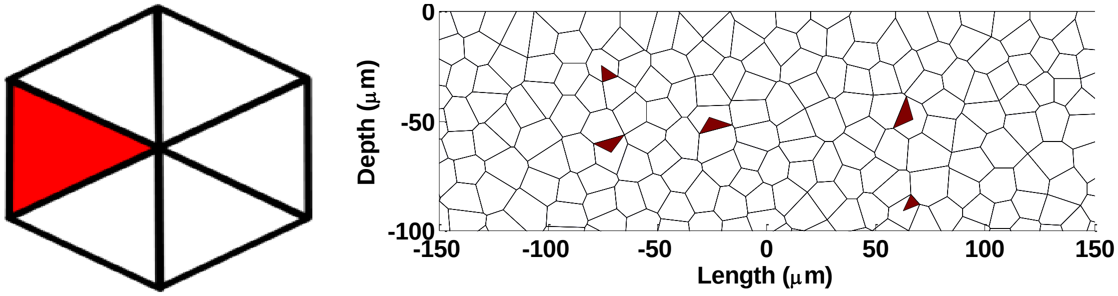

(a) (b)

Figure 4.26: (a) initial void. (b) Example of a material domain with randomly introduced 5 initial voids.

Simulations were performed for 35 random microstructure domains for through hardened material with 1, 2 and 5 randomly placed initial voids at loads P_{max} = 2.0, 2.75 and 3.5 GPa. Figure 4.27 (a) depicts the Weibull probability plots from the model results for pristine and with voids case for P_{max} = 2.0 GPa while Figure 4.27 (b) shows results for 1 initial void at different loads. The same results are reported in tabular format in Table 4.4. It is evident from the results that when material flaws are taken into account, model results show considerable scatter in the fatigue lives. As the number of voids increase, the L_{10} life for RCF decreases. Further, for the same no. of voids, as the pressure increases the L_{10} life decreases and fatigue lives become more deterministic.

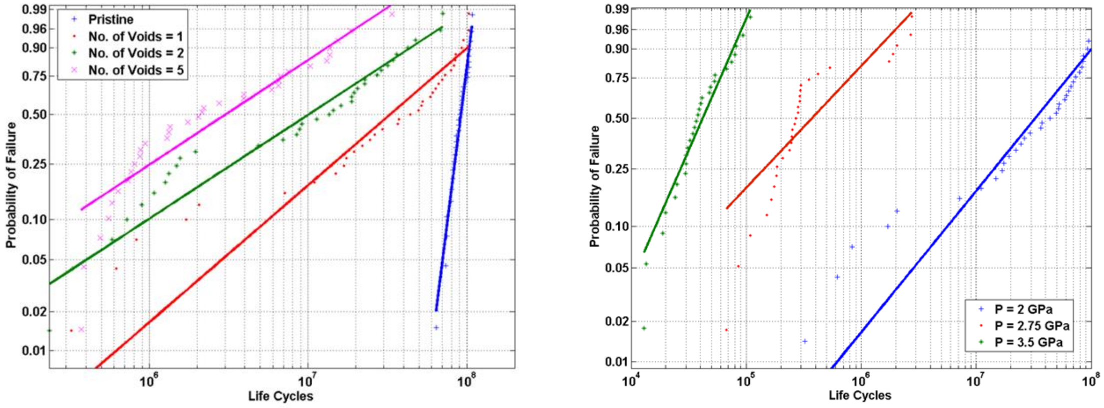

(a) (b)

Figure 4.27: Weibull plots for RCF lives for through hardened with initial voids. (a) P_{max} = 2 GPa, (b) Number of voids = 1.

The typical spall patterns from model results with initial voids are depicted in Figure 4.28 and Figure 4.29. The initial void is colored in red. It was observed that if the initial void occurs close to critically stressed region, spalls initiate at the void. As the load increases the damaged zone grows in size. These results are in accordance with the experimentally observed spalls.

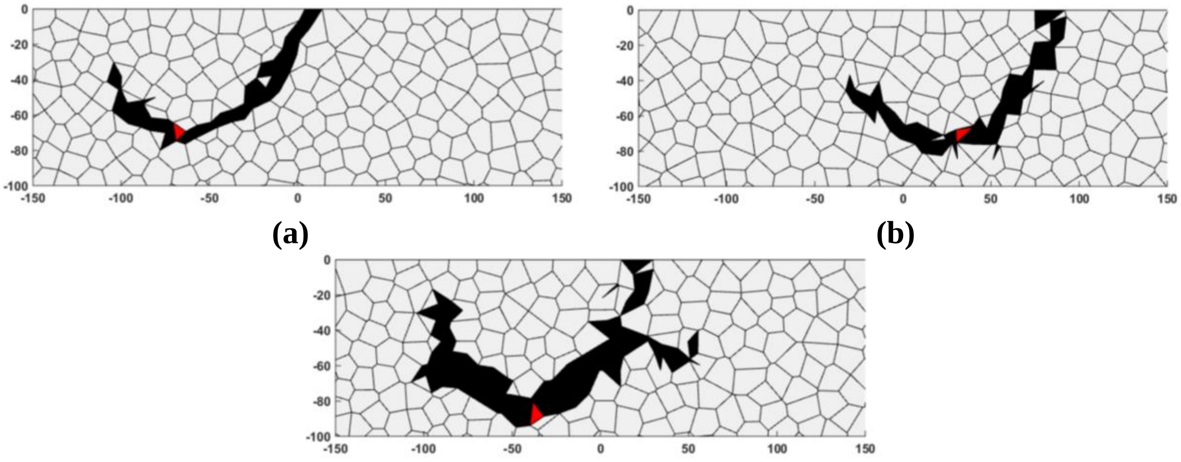

(a) **(b)**

(c)

Figure 4.28: Typical spall patterns obtained from the model for through hardened material with initial voids at (a) P_{max} = 2.0 GPa, (b) P_{max} = 2.75 GPa, (c) P_{max} = 3.5GPa.

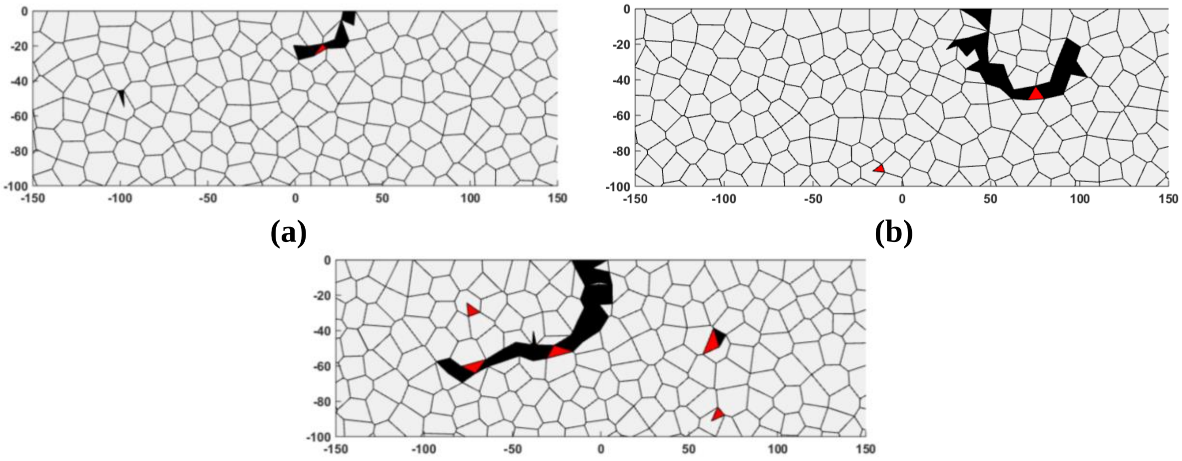

(a) **(b)**

(c)

Figure 4.29: Typical spall patterns for through hardened material at P_{max} = 2.0 GPa with (a) 1 void, (b) 2 voids and (c) 5 voids.

Table 4.4: Weibull plots and L10 lives obtained from the model results for through hardened material with initial voids.

	Pristine		**Voids = 1**		**Voids = 2**		**Voids = 5**	
	Slope	**L_{10} Life**	**Slope**	**L_{10} Life**	**Slope**	**L_{10} Life**	**Slope**	**L_{10} Life**
P_{max} = 2 GPa	9.82	7.58E+07	1.07	5.61E+06	0.81	9.80E+05	0.82	3.00E+05
P_{max} = 2.75 GPa	8.13	2.03E+06	0.92	4.81E+04	1.99	1.62E+04	3.96	7.57E+04
P_{max} = 3.5 GPa	26.39	1.02E+05	1.99	1.62E+04	4.24	1.99E+04	4.41	1.36E+04

4.4 Summary and Conclusions

This chapter presented a numerical model based on micro-indentation tests to study the effect of case carburizing on rolling contact fatigue lives rolling element bearings. In order to achieve the objectives, micro-indentation tests were performed to calculate Vicker's hardness at various depths along the cross-section. It was observed that hardness follows a bilinear profile for case-carburized 8620 steel. The hardness decreases linearly with the depth in the case carburized region and remains constant in the core region. Whereas for the through hardened steel the hardness (yield strength) was assumed constant throughout the depth. In the simulations, the hardness of the material was modeled by examining the change in mechanical properties of the material due to hardening. It was assumed that the hardening process only affects the plastic response of the material and there is a linear correlation between hardness and yield strength. The residual stress distribution typically observed in the case carburized material is also taken into account in the model. Damage mechanics constitutive relations for linear elastic kinematic plastic material were incorporated in the finite element model to capture progressive damage for rolling contact fatigue. Randomly generated Voronoi tessellations were used to study the variability occurring due to the randomness in material microstructure.

The model was utilized to study the effect of hardening process on sub-surface stress distribution for pristine material. Then parametric study was conducted by varying the parameters related to the yield strength and residual stress distribution in the case carburized steel. From the results of the parametric study an equation for the modifying factor to calculate the L_{10} lives of case carburized steels is derived. The optimized case depth for maximizing the RCF strength is 6.2b for P_{max}= 2 GPa and 7.6b for P_{max}= 3.5 GPa.

Additionally, the model resulted in spall patterns which resemble those commonly observed in experiments. The location of initial damage and the size of the damaged zone for different case depths were explained with the help from the sub-surface stress solutions. When the random distribution of initial flaws was considered in the model, the scatter in the fatigue lives fell within the experimentally observed range.

5. ROLLING CONTACT FATIGUE IN REFURBISHED CASE CARBURIZED BEARINGS

5.1 Introduction

Bearing manufacturers have used various techniques to increase the working life of REBs, of which one of the ways is to limit the RCF related bearing damage. Chapter 4 investigated hardened steels which are commonly used in high-performance ball and rolling element bearings. In addition to using heat-treated steels, bearing refurbishment has gained popularity as a means of extending the fatigue life of rolling element bearings since NASA published recommended procedures for bearing repair in the mid-1970s [136]. Between 60% and 80% of the cost of new bearings can be saved by using typical repaired bearings instead of replacing them [137]. Additionally, the lead times can be significantly reduced for custom bearings. Therefore, bearing repair procedures have been implemented in various applications including commercial and military aircraft and off-highway and construction equipment [136].

According to the NASA specifications [138], bearing repairs are categorized into four levels according to the extent of the damage to the bearing surfaces and the recommended replacement of the bearing components. Among the four repair categories, Level 3 shows significant improvement in the lives of REBs with minimal cost. It comprises removal of surface damage by grinding up to 0.015 inches off the inner and/or outer race and replacing the original rollers with larger-sized rollers that compensate for the material removal from the races [139]. In Level 3 repairs, the surface damage is usually caused by non-optimal operating conditions. This type of repair avoids bearing damages from surface-initiated pitting, which accounts for more than 90% of bearing damages observed in industry. The repaired bearings then generally fail because of the subsurface-initiated spalling mode of RCF, since in this mode the damage penetrates below the maximum allowable grinding depth. However, limited research and testing to determine the life of the repaired bearings after grinding and reassembling has restricted the widespread implementation of bearing restoration.

Testing has been conducted for specific industries and applications; therefore it cannot be generalized [140]. In terms of analytical modeling, Coy et al. [136] extended the Lundberg-Palmgren bearing life equation [*14*] to determine the fatigue life of the outer races of repaired bearings. Zaretsky and Branzai [141] modified the equation using maximum shear stress criteria and included the fatigue damage of the inner races as well as the rolling elements. Kotzalas and Eckels [140] considered the entire stress field for the contacting bodies and created an analytical model for refurbishment using the ISO 281:2007 standard [142]. However, these models are empirical in nature and use the Weibull probability distribution function to explain the fatigue life scatter without explaining the underlying physical mechanisms responsible for RCF. Further, they assume the Weibull parameters for refurbished bearings are based on the Weibull parameters of the original bearings. Experimental testing must be conducted to determine the Weibull parameters for RCF lives of refurbished bearings.

Recently, Paulson et al. [143] developed a finite element (FE) model for rolling contact fatigue in refurbished bearings. The model was based on a numerical model for RCF developed by Raje et al. [27], Jalalahmadi and Sadeghi [30] and Slack and Sadeghi [97]. The material removal from the surface by grinding was simulated by cutting the top layer of the microstructure domain. The initial damage that had occurred before the refurbishment was retained in the remaining microstructure. This accounted for the initial load passes undergone by the material. Using the model results, a population L10 life of the resurfaced bearings was proposed. However, the material considered by Paulson et al. [143] was through hardened steel, and the study did not take into account the plastic behavior of the material. Case carburized steels are characterized by a hardened exterior, gradients in the material properties as a function of depth, and residual stresses, so refurbishment of bearings made from case carburized steels requires greater care and more in-depth analysis. But there has been no analytical model developed to study refurbishing of case carburized bearings.

In this chapter, the RCF model for case carburized steel developed in Chapter 4 was modified to incorporate the procedure to simulate bearing refurbishing developed by Paulson et al. [143]. Similar to Chapter 4, material degradation due to fatigue damage was modeled using continuum damage mechanics. The effect of the carburizing process was incorporated by changing the yield strength of the material linearly with the hardness and including the residual stress distribution in the model. Thus, the von Mises plasticity-based model with kinematic hardening was implemented in the FE model to incorporate material plasticity. Equivalence between torsion and rolling contact fatigue was utilized to determine the damage parameters in the elastic and plastic damage law. The damage evolution laws were modified to include the effect of residual stress. The geometric disorder and randomness in the material microstructure was simulated using Voronoi tessellation to account for the variability in rolling contact fatigue life. The procedure to simulate the grinding of the material during the refurbishment process and the retention of the accumulated damage that had occurred before the refurbishment was implemented as per Paulson et al. [143]. However, the altered yield strength and residual stress distribution in the refurbished material due to the material removal from the surface during refurbishing were also taken into account.

The model was then used to investigate the effect of hardening on the RCF lives of the refurbished bearings under various operating conditions. To assess the effect of plastic deformation, the contact was subjected to Hertzian pressure of 2 and 3.5 GPa. The half-width of the contact (b) was fixed at 100 μm. The surface regrinding depth was varied from 0.125 to 0.75 times the contact half width. The effects of fatigue cycles prior to refurbishing were also investigated. From the simulation results, the RCF lives of refurbished bearings made from case carburized and through hardened bearing steel were compared. First, the effects of hardness and residual stress variation were analyzed separately. Then, the combined effect of hardness variation and residual stress distribution for the case carburized steel was investigated. The analytical results from the model suggest that the increase in RCF life due to refurbishing is more significant in through hardened material than in case carburized material. As expected, the absolute RCF life is significantly more for refurbished case carburized bearings due to the compressive residual stresses induced during regrinding of the bearing surface can have a beneficial impact on the fatigue performance of the refurbished bearing.

5.2 Modeling Approach

The modeling approach consisted of simulating rolling contact fatigue in pristine case carburized material first, and then simulating the refurbishing operation. Modeling rolling contact fatigue constitutes implementing the material properties of case carburized steel in the FE model, which simulates a rolling pass, and modifying the damage mechanics model, which simulates material degradation due to fatigue. In this section, the modeling approach is described in brief for completeness. For a detailed description, please refer to Chapter 4.

5.2.1 Material properties of case carburized steel

Case carburized steels are characterized by a hardened exterior that progressively tapers into a softer core beneath the surface. The distance from the surface where the carburized region ends is referred to as the "case depth". The carburized region includes a harder carbide phase surrounded by the steel matrix. The distribution of carbides gradually reduces with the depth, affecting the material properties of the material. The gradient and depth of the carburization vary depending on its type and time duration. Carburization causes gradients in the material microstructure and composition as a function of depth ([144], [145]). Pavlina and Tyne [128] showed that there is a linear correlation between yield strength (S_y) and Vickers hardness (H_v):

$$S_y = -90.7 + 2.876H_v \tag{5.1}$$

where yield strength is described in MPa and H_v in units of (Kg_f/mm^2).

Additionally, the carburization process introduces residual stresses (RS) in the case region of the material. Residual stresses are highly beneficial in improving the fatigue strength of the case carburized material [129]. Parrish and Harper [130] surveyed around 70 different carburized steels with case depths lower than 1 mm and their residual stress distributions. They found that the typical RS distribution in case carburized material follows the pattern depicted in Figure 4.5. For the majority of samples, the depth at which peak RS occurs was 20% of the case depth. The residual stress diminishes to zero at a depth equal to the case depth of the material.

As described in Chapter 4, the hardness of the material is not simulated directly. Instead, the linear relationship between hardness and yield stress as given by Equation (5.1) was used to account for the variation in hardness in the case carburized material. Therefore, the yield strength of the through hardened steel was set to 2 GPa throughout the depth, while a bilinear yield strength profile was assumed for the case carburized steel. The maximum hardness at the surface of the case carburized material was also set to 2 GPa, whereas the yield strength of the core material was assumed to be 1 GPa. The yield strength values for the finite elements were assigned depending on the y-coordinates of their centroids. A simplified piecewise linear profile was used to approximate the residual stress distribution for the case carburized material. The surface and peak values of RS were fixed at -200 and -450 MPa, respectively. Figure 5.1 illustrates the yield strength and RS distribution for the case carburized material with a case depth of 500 μm used in this study. Please note that there would be tensile residual stresses below the case region of the material for the residual stress distribution to be in equilibrium.

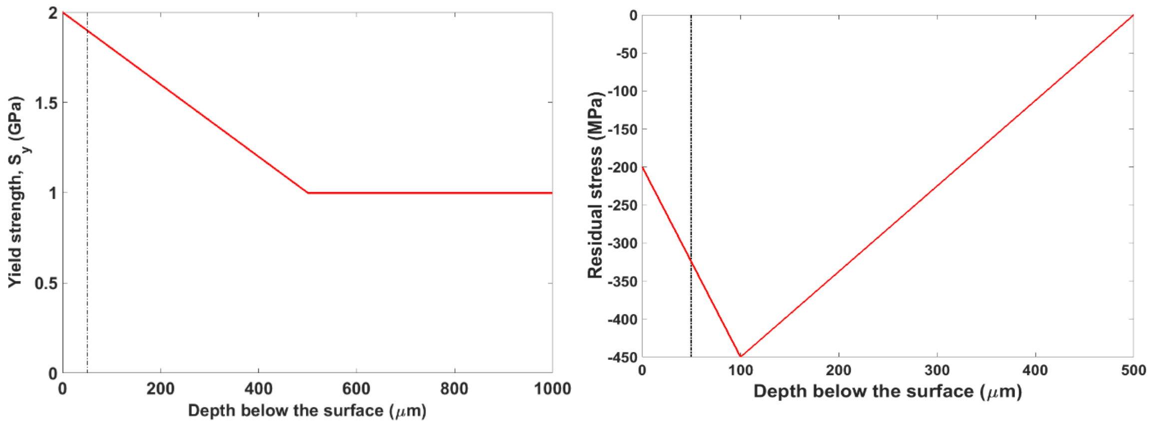

(a)

(b)

Figure 5.1: (a) Yield strength and (b) RS distribution for case carburized material with case depth of 500 μm.

5.2.2 Simulation of a rolling pass

An FE model used in this study to simulate the line contact arising between the roller and raceway in rolling element bearings was same as described in chapter 4. The rolling pass was simulated by subjecting the domain to a sequence of surface tractions at 21 discrete locations uniformly spaced from *-2.0b* to *2.0b* in the rolling direction. The user subroutine UTRACLOAD was used to apply the Hertzian pressure as non-uniform surface traction vectors. Equation (5.2) defines the normal and tangential component of the surface traction:

$$p_y(x) = P_{max} \sqrt{1 - \left(\frac{(x - x_c)}{b}\right)^2} \tag{5.2}$$

$$t_x(x) = \mu_s |p_y(x)|$$

Where (x_c, 0) is the coordinate of the center of the Hertzian pressure distribution, P_{max} is the maximum Hertzian pressure and (x, y) is the coordinate where the pressure is evaluated. μ_s is the coefficient of friction.

Similar to the model used in Chapter 4, Voronoi tessellation was utilized to account for geometric disorder and the randomness in the material microstructure topology. Voronoi tessellation is well accepted as an approach to model the topology of the prior austenitic grain structure of the bearing steel ([30], [33], [34], [97], [107]) i.e. the parent austenite grain structure before quenching, in contrast to the final microstructure of bearing steels which will be composed of martensite, ferrite and austenite. Mücklich et al. [92], Espinosa and Zavattieri [93] and Jalalahmadi and Sadeghi [29] have shown that Voronoi tessellations can be used to represent the grain structure of the polycrystalline material to a good degree of accuracy and can be used to simulate its effect on fatigue life. Experimental evidences show that fatigue failure in bearings can be intergranular or transgranular. The present work assumes that the austenite (prior) grain boundaries constitute weak planes in the material, and therefore fatigue cracks are predominantly intergranular.

In this analysis, the Voronoi cell size was chosen to be 10 μm, which is the common grain size for commercially used bearing steels ([27], [30]). Please note that for case carburized AISI 8620 steel, the microstructure consists of coarse grains in the core region and finer grains near to the surface. In the current investigation the gradient in grain size observed in the case carburized material is not taken into account.

RCF is characterized by highly localized multi-axial stress distribution in the contact region, which causes considerable plastic deformation at high loads. Furthermore, case carburization affects the yield strength of the material. Therefore, an elastic-plastic material model is needed to correctly capture the stress-strain response of the rolling line contact. The extended ELKP model described in Chapter 4 was implemented to define a material model for both pristine and refurbished material.

5.2.3 Fatigue damage model

The fatigue damage model for RCF in refurbished case carburized bearings is same as the RCF model for case carburized bearings described in Chapter 4. Material degradation from fatigue damage is modeled using continuum damage mechanics (CDM) which introduces a thermodynamic state variable, D, into the material constitutive relationship. For isotropic damage and neglecting the effect of Poisson's ratio on damage, the damage tensor reduces to a scalar quantity:

$$\sigma = E(1-D)\varepsilon \tag{5.3}$$

where E is the elasticity modulus for the undamaged material. The value of D is equal to 0 for the pristine material, while the value of 1 for D corresponds to completely damaged material. For elastic-plastic material behavior, the damage variable is introduced in the von Mises yield criterion for kinematic hardening (Warhadpande et al. [33] and Bomidi et al. [34]). Accordingly, the yield function *f* is modified as below:

$$f = (\tilde{\sigma} - \alpha)_{eq} - S_y \tag{5.4 (a)}$$

$$(\tilde{\sigma} - \alpha)_{eq} = \sqrt{\frac{3}{2}\left(\frac{\sigma_{ij}^{D}}{1-D} - \alpha_{ij}\right)\left(\frac{\sigma_{ij}^{D}}{1-D} - \alpha_{ij}\right)} \tag{5.4 (b)}$$

where α is the back-stress tensor representing the center of the yield surface; S_y is the radius of the yield surface (i.e., the yield strength); and σ^D is the deviatoric part of the stress tensor.

Similarly, plastic strain and kinematic hardening rate equations are modified as:

$$\dot{\epsilon}_{ij}^{p} = \dot{\lambda}\frac{\partial f}{\partial \sigma_{ij}} = \frac{\dot{\lambda}}{1-D}\left(\frac{\sigma_{ij}^{D}}{1-D} - \alpha_{ij}\right) \tag{5.5 (a)}$$

$$\dot{\alpha}_{ij} = -\hat{C}\dot{\lambda}\frac{\partial f}{\partial \alpha_{ij}} = \hat{C}\dot{\lambda}\left(\frac{\sigma_{ij}^{D}}{1-D} - \alpha_{ij}\right) \tag{5.5 (b)}$$

Here, $\dot{\lambda}$ is a plastic multiplier and $\hat{C}$ is the scalar multiplier for hardening.

The stress component that governs the damage evolution variable depends on the bearing damage mechanism for the phenomenon of interest. Shear stress reversal is considered to be the critical stress component that promotes RCF damage in the elastic regime. In the damage law-plastic case, maximum von Mises stress ($\sigma_{\max}$) and accumulated plastic strain over a rolling pass are considered the damage-causing stressors (Lamaitre [100]). The damage evolution laws for modeling RCF in case carburized steels are as follows:

$$\left(\frac{dD}{dN}\right)_{elastic} = \left[\frac{\Delta\tau_{critical}}{\tau_{ro}\left(1-\frac{\sigma_m}{S_{us}}\right)(1-D)}\right]^m \quad (5.6\ (a))$$

$$\left(\frac{dD}{dN}\right)_{plastic} = \left[\frac{\sigma_{\max}^2}{2ES_0\left(1-\frac{\sigma_m}{S_{us}}\right)^2(1-D)^2}\right]^q \dot{p} \quad (5.6\ (b))$$

Here, $\Delta\tau_{critical}$ *is the* maximum shear stress reversal and $\dot{p}$ is the accumulated plastic strain resolved along the grain boundary. τ_{r0} and S_0 are the material parameters that characterize the material's resistance to fatigue damage. σ_m represents the mean stress due to the presence of residual stresses and S_{us} is the ultimate strength in shear.

5.2.4 Evaluation of damage parameters and numerical implementation

As described in Chapter 4, it can be presumed that the bearing damage mechanisms for rolling contact fatigue and torsion fatigue are equivalent, and the material parameters in the elastic and plastic damage rate laws can be determined using the stress-life (S-N) data from torsion fatigue experiments. The detailed derivation of equations to calculate the damage parameters for case carburized steel from torsion SN curve is presented section 4.2.5. The variations of τ_{r0} and S_0 with the yield strength are demonstrated in Figure 5.2. Note that the exponents, m and q in the damage rate law depend only on the fatigue strength exponent (b). Therefore, they remain constant irrespective of the yield strength. Please refer to section 4.2.6 for the step-by-step procedure of numerical implementation of the fatigue damage model. 4.2.5

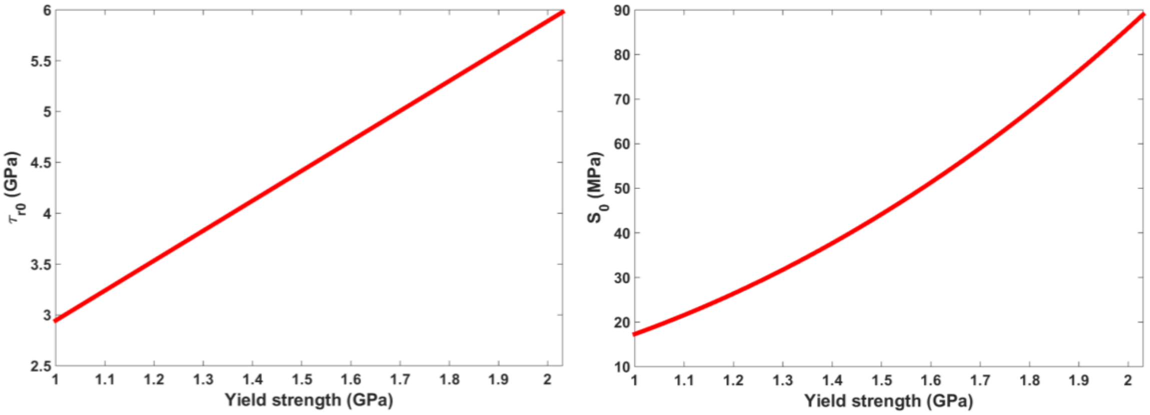

Figure 5.2: Variation of damage parameters τ_{r0} and S_0 with change in yield strength.

5.2.5 Simulating refurbishment

In this investigation, the procedure for simulating bearing resurfacing developed by Paulson et al. [143] was implemented. To find the fatigue life of the refurbished bearing, it is necessary to determine the state of the damage for all the elements in the domain prior to the refurbishment. In order to make this determination, the random Voronoi domain was subjected to rolling contact fatigue simulations using the fatigue damage model. The bearing damage criterion in this case is when the damage reaches the surface. The damage evolution curve for each element in the domain was evaluated from this simulation. Using this curve, the value of damage variable for the element once the bearing has been refurbished (N_{refurb}) can be interpolated. This process is demonstrated in Figure 5.3, where N_{crit} is the number of fatigue cycles undergone when the element damage reaches 1. If N_{refurb} is greater than N_{crit}, the damage value is equal to 1.

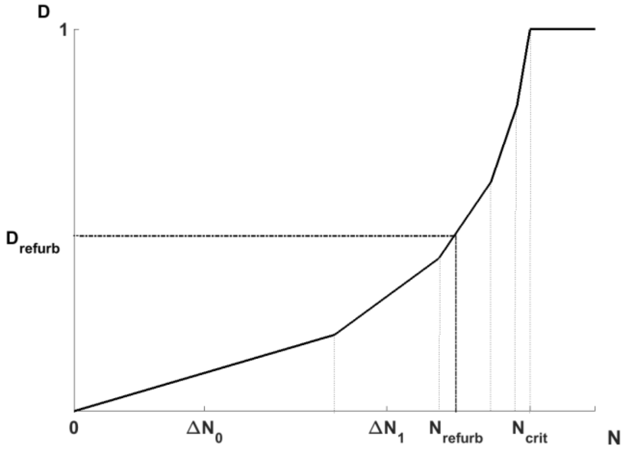

Figure 5.3: Damage evolution curve and interpolated damage at refurbishing cycle.

To simulate the grinding of the material during the refurbishment process, a line was passed through the domain at the desired depth. The Voronoi cells that were completely above this line were removed from the domain. As illustrated in Figure 5.4, the cutline forms the upper boundary of the Voronoi cells that intersect the cutline. New nodes are created at the point of intersection between the Voronoi cells and the cutline. As mentioned before, the yield strength and residual stresses vary with depth for case carburized steel. In order to simplify the problem, it was assumed that the grinding process does not alter the yield strength or residual stress distribution in the material remaining after refurbishing. It should be noted that this simplification is one of the limitations of the model and does not accurately represent reality.

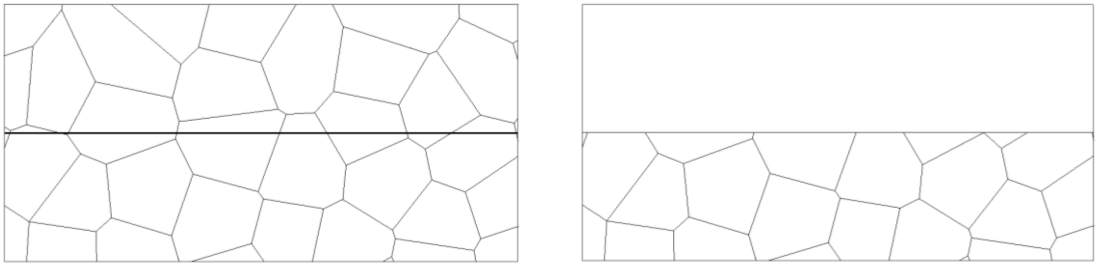
(a) **(b)**

Figure 5.4: (a) Original microstructure domain. (b) Microstructure domain after resurfacing.

Figure 5.5 depicts the distribution of yield strength and residual stress in the modified microstructure domain (resurfaced material) for different grinding depths. Once the refurbishing was simulated, RCF modeling was restarted with the modified domain and continued until the damage reached the surface. The accumulated damage retained to account for the fatigue damage before refurbishing acted as an initial condition for this simulation. The total life of the bearing was calculated by adding the life of the refurbished bearing and the life cycles experienced by the original bearing before refurbishing.

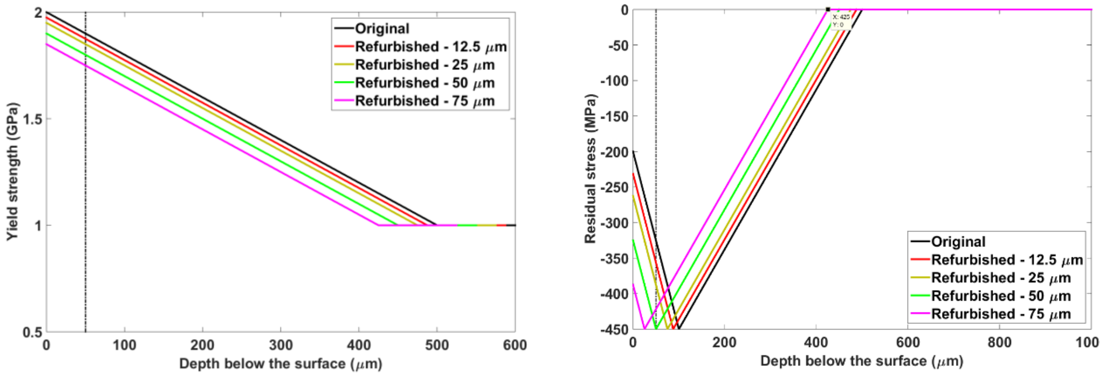

(a) **(b)**

Figure 5.5: Distribution of (a) yield strength and (b) residual stress vs. depth after resurfacing to different grinding depths.

5.3 Results and Discussion

This section describes the results obtained from the fatigue damage model for rolling contact fatigue of refurbished cylindrical roller bearings made from through-hardened and case carburized bearing steel. Fatigue cycles prior to the refurbishing and depths of grinding were varied to investigate their effects on the total fatigue life of the bearing.

In this study, the half-width of contact was kept fixed at 100 μm for all cases. Thirty-three random microstructure domains were constructed using the Voronoi tessellation procedure to investigate variability in fatigue lives due to subsurface microstructure topology. Maximum Hertzian pressure (P_{max}) was varied from 2.0 GPa to 3.5 GPa so the fatigue performance of the steels could be analyzed when a considerable portion of the material was undergoing plastic deformation. For all cases, the simulations were performed for 33 microstructure domains without refurbishing to obtain the L_{10} life. Microstructure domains were ground to 12.5, 25, 50 and 75 μm below the original surface. The selected running times prior to the refurbishing were 50% and 90% of the population L_{10} life cycles of the bearing without refurbishing ($L_{10/\mathrm{original}}$). Table 5.1: Material properties used in the simulationTable 4.2 summarizes the parameters and material properties used in this simulation. Please note that the elastic modulus (*E*) of the carburized material can vary +/- 20 GPa in the case region [124]. Since the variation in *E* is small compared to the variation in S_y and residual stress, the elasticity modulus of the pristine material is assumed to be uniform throughout the domain.

Table 5.1: Material properties used in the simulation.

Undamaged elasticity modulus, *E*	200 GPa
Hardening modulus, M	10 GPa
Poisson's ratio, *v*	0.3
Material grain diameter, d_g	10 µm
Maximum Hertzian pressure, p_{max}	2.0-3.5 GPa
Contact half-width, *b*	100 µm
Surface coefficient of friction, μ_s	0.05
Critical damage value, D_{crit}	1

5.3.1 Accumulated damage before refurbishing

Figure 5.6 depicts the accumulated damage before refurbishing at 50% and 90% of $L_{10/original}$ for different grinding depths for case carburized steel (case depth = 500 µm) at $P_{max} = 2$ GPa. It can be observed that for both cases, the damage is concentrated at 0.5b (50 µm) below the original surface. However, damage for the bearing refurbished at 90% of L_{10} life is considerably higher than the bearing refurbished at 50% of L_{10} life for all regrinding depths. This is expected because the bearing is experiencing more fatigue cycles. For the regrinding depths of 12.5 and 25 µm, the range of damage is nearly the same. Additionally, the elements with the most damage grew closer to the surface. In the case of the regrinding depths of 50 and 75 µm, the range of damage became significantly smaller since the most damaged elements occurring around 50 µm below the original surface were ground off. However, for regrinding depths of 50 µm, there is a possibility that the element with the most damage may occur just below the depth of 50 µm; consequently, it would remain in the resurfaced material. For those material domains, the damage would be very close to the surface and thus, regrinding depths >75 µm will minimize initiation and occurrence of RCF related surface damage.

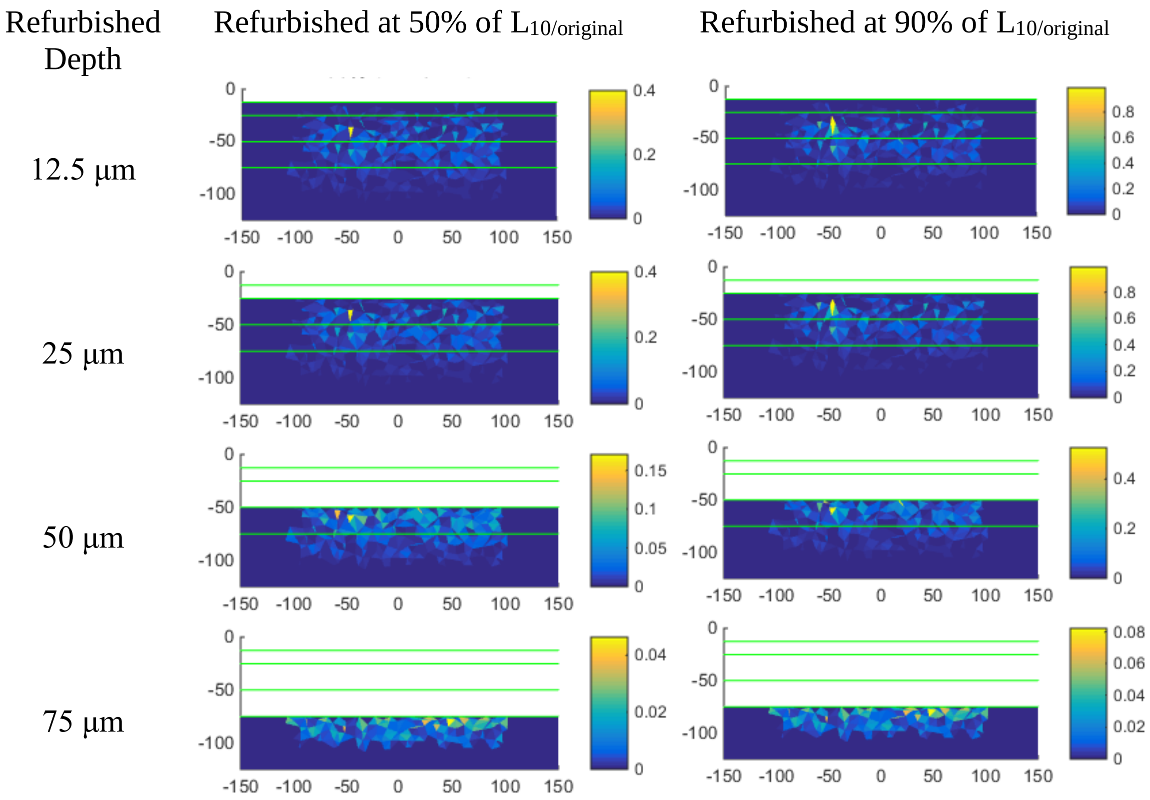

Figure 5.6: Accumulated damage before refurbishing at different cycles for different grinding depths for case carburized steel at P_{max} = 2.0 GPa. The colorbar represents the value of the damage variable for each element.

5.3.2 Comparison of RCF lives

Figure 5.7 and Figure 5.8 illustrate the Weibull plots for through hardened material at P_{max} = 2 GPa and 3.5 GPa, respectively. The L_{10} lives and Weibull slopes obtained from the model results are listed in Table 5.2 and Table 5.3. $L_{10/original}$ refers the RCF life of the pristine bearings with no refurbishing. While, $L_{10/refurbishing}$ refers the total RCF life of the refurbished bearings. The total RCF life of the refurbished bearings is calculated by addition of the fatigue cycles prior to refurbishing and the fatigue cycles experienced by the bearings after the refurbishing until the final failure. The ratio of the L_{10} life of refurbished bearings to the L_{10} life of bearings without refurbishing, which signifies the effectiveness of the refurbishing process, are also listed in the tables. Please note that there are no residual stresses, and material properties are uniform throughout the depth.

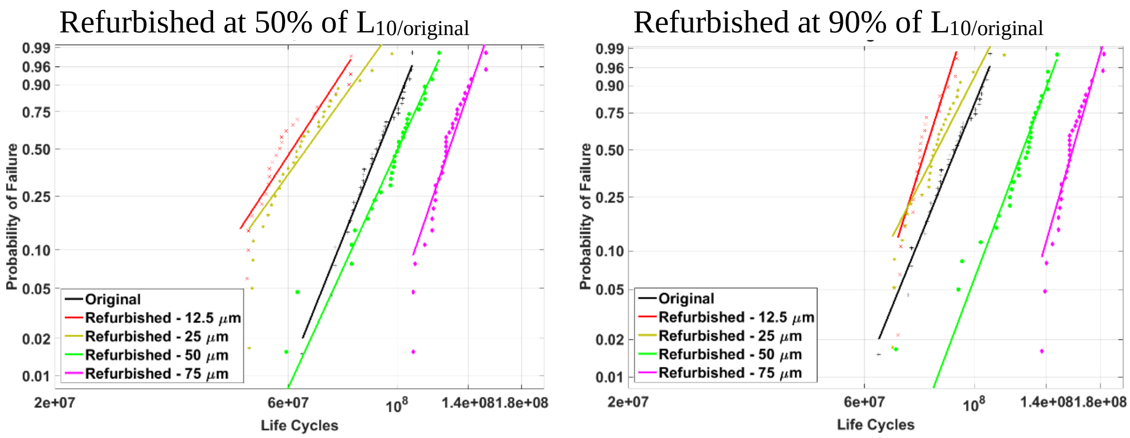

Figure 5.7: Weibull probability plots for refurbished bearings of through hardened steel at P_{max} = 2 GPa.

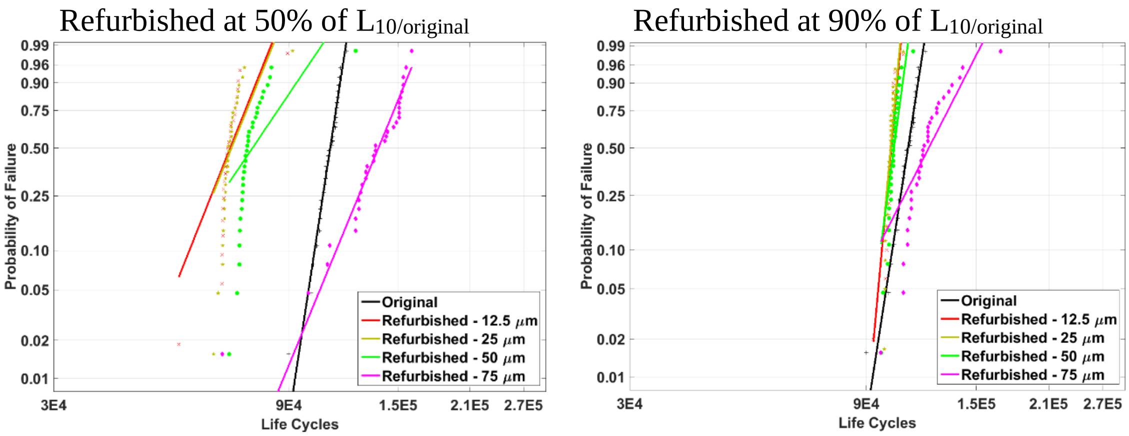

Figure 5.8: Weibull probability plots for refurbished bearings of through hardened steel at P_{max} = 3.5 GPa.

Table 5.2: Predicted Weibull slopes and L_{10} lives for refurbished bearings with through hardened steel at P_{max} = 2 GPa.

	Refurbished after 50% of $L_{10/orig}$			Refurbished after 90% of $L_{10/orig}$		
Refurbishing Depth	L_{10} Life (Cycles)	$\frac{L_{10/refurb}}{L_{10/orig}}$	Weibull Slope	L_{10} Life (Cycles)	$\frac{L_{10/refurb}}{L_{10/orig}}$	Weibull Slope
Pristine	7.58E+07	-	9.87	7.58E+07	-	9.87
12.5 μm	4.48E+07	0.59	6.07	6.87E+07	0.91	12.73
25 μm	4.64E+07	0.61	5.51	6.60E+07	0.87	7.80
50 μm	8.08E+07	1.07	8.63	1.05E+08	1.39	10.67
75 μm	1.09E+08	1.44	11.69	1.38E+08	1.82	13.94

Table 5.3: Predicted Weibull slopes and L_{10} lives for refurbished bearings with through hardened steel at P_{max} = 3.5 GPa.

	Refurbished after 50% of $L_{10/orig}$			Refurbished after 90% of $L_{10/orig}$		
Refurbishing Depth	L_{10} Life (Cycles)	$\frac{L_{10/refurb}}{L_{10/orig}}$	Weibull Slope	L_{10} Life (Cycles)	$\frac{L_{10/refurb}}{L_{10/orig}}$	Weibull Slope
Pristine	1.02E+05	-	25.82	1.02E+05	-	25.82
12.5 µm	5.66E+04	0.56	9.89	9.68E+04	0.95	43.45
25 µm	5.68E+04	0.56	9.77	9.66E+04	0.95	44.04
50 µm	5.50E+04	0.54	5.83	9.61E+04	0.95	29.71
75 µm	1.12E+05	1.11	9.55	9.45E+04	0.93	7.78

It can be noted from Table 5.2 and Table 5.3 that as the refurbishing depth increases, L_{10} life also increases, up to a maximum refurbishing depth of 75 µm. This is expected, since the part of the material critically damaged due to the fatigue cycles prior to refurbishing is removed by grinding. Thus, the refurbished bearing performs as well as the pristine bearing. For refurbishing depths smaller than 0.5b (50 µm), the total fatigue life of the refurbished bearings is actually less than the life of the unrefurbished bearings, which can also be explained by analyzing the accumulated damage before refurbishing shown in Figure 5.6. It is also interesting to see from the model results that refurbishing the bearing after 90% of $L_{10/original}$ is more effective than refurbishing after 50% of $L_{10/original}$. However, it should be recognized that life after refurbishing is more significant for bearings refurbished after 50% of $L_{10/original}$, which can be explained by the state of accumulated damage illustrated in Figure 5.6.

These results are consistent with the refurbishing model previously proposed by Paulson et al. [143]. Some minor differences in the values result from the fact that an elastic-plastic material model was incorporated in the current model. Comparing the effectiveness of refurbishing for P_{max} = 2 GPa and 3.5 GPa, model results show that refurbished bearings experiencing higher loads do not perform as well. This is because the extent of damage (volume of the material damaged) due to fatigue cycles prior to refurbishing is greater at higher loads. Therefore, there is a lot of damage close to the surface after resurfacing, which lowers the fatigue life after refurbishing. It should also be noted that in general, the scatter in fatigue lives is very high at low loads — a phenomenon often observed in the fatigue experiments.

The RCF lives of refurbished bearings made of case carburized steel (case depth = 500 μm) were investigated next. As described in section 2.1, there is variation in yield strength and residual stresses with depth in case carburized steels. To simplify the analysis and their effects on life distribution, each variable was first accounted for separately, and then their combined effect was studied. Figure 5.9 depicts the results accounting only for hardness with no residual stress. Similar to through hardened steel, as the refurbishing depth increases, the fatigue life increases. For P_{max} = 2 GPa, the refurbished bearing life is more than the original bearing life only if the bearing is refurbished after 90% of $L_{10/original}$ and refurbishing depth is more than 50 μm.

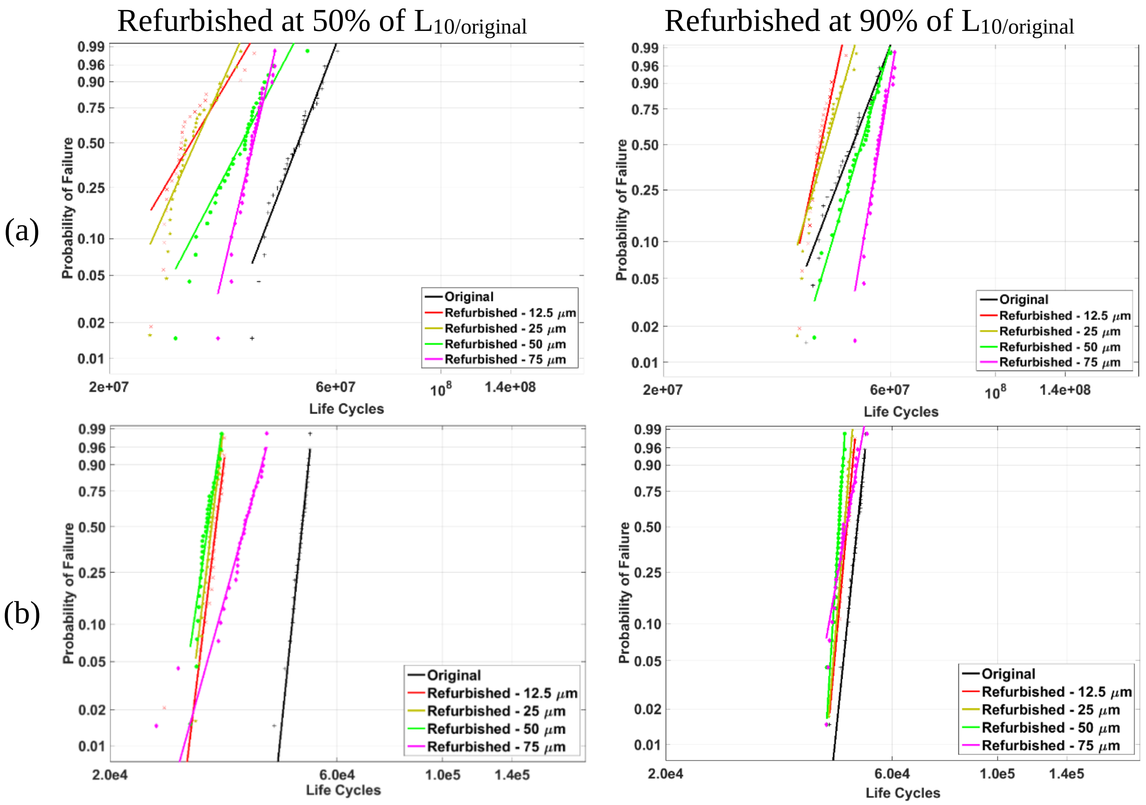

Figure 5.9: Weibull probability plots for refurbished bearings of case carburized steel accounting only for hardness variation: (a) P_{max} = 2 GPa; (b) P_{max} = 3.5 GPa.

Compared to through hardened steel, the effectiveness of refurbishing is less in this case. This can be best explained by studying the yield strength variation for refurbished bearings shown in Figure 5.5(a). During the refurbishing process, the harder region near the surface is removed. Therefore, critical stress due to rolling contact (shown by the dashed line in Figure 5.5(a)) occurs in the comparatively softer region, which diminishes the fatigue strength of the material. This phenomenon does not occur in the through hardened steel because it has uniform yield strength throughout the depth. This effect is even more pronounced for P_{max} = 3.5 GPa; the fatigue lives of the refurbished bearings for all test cases were lower than the original bearing life.

Figure 5.10 illustrates the Weibull plots for refurbished bearings while accounting only for the variation in residual stress, with the yield strength kept uniform at 2 GPa throughout the depth. In this case, refurbishing to the depth of 50 and 75 µm increases the fatigue life significantly above the life of the original bearing at P_{max} = 2 GPa. Moreover, the refurbishing is more effective in case carburized steel than in the through hardened steel, especially at a refurbishing depth of 50 µm. This can be explained by examining the RS distribution for refurbished bearings in Figure 5.5(b). After refurbishing, the critically stressed region (shown by the dashed line) exhibits the maximum compressive residual stress, which enhances the fatigue performance. For P_{max} = 3.5 GPa, however, the effect of the damage accumulated before refurbishing dominates, and the refurbishing process improves the fatigue life only in the case of a refurbishing depth of 75 µm.

Therefore, for case carburized steel, the variation of yield strength and residual stress with depth have conflicting influences on the effectiveness of refurbishing. Yield strength diminishes the fatigue life of the refurbished bearing — but, on the other hand, residual stress enhances fatigue life when compared to the life for through hardened steel.

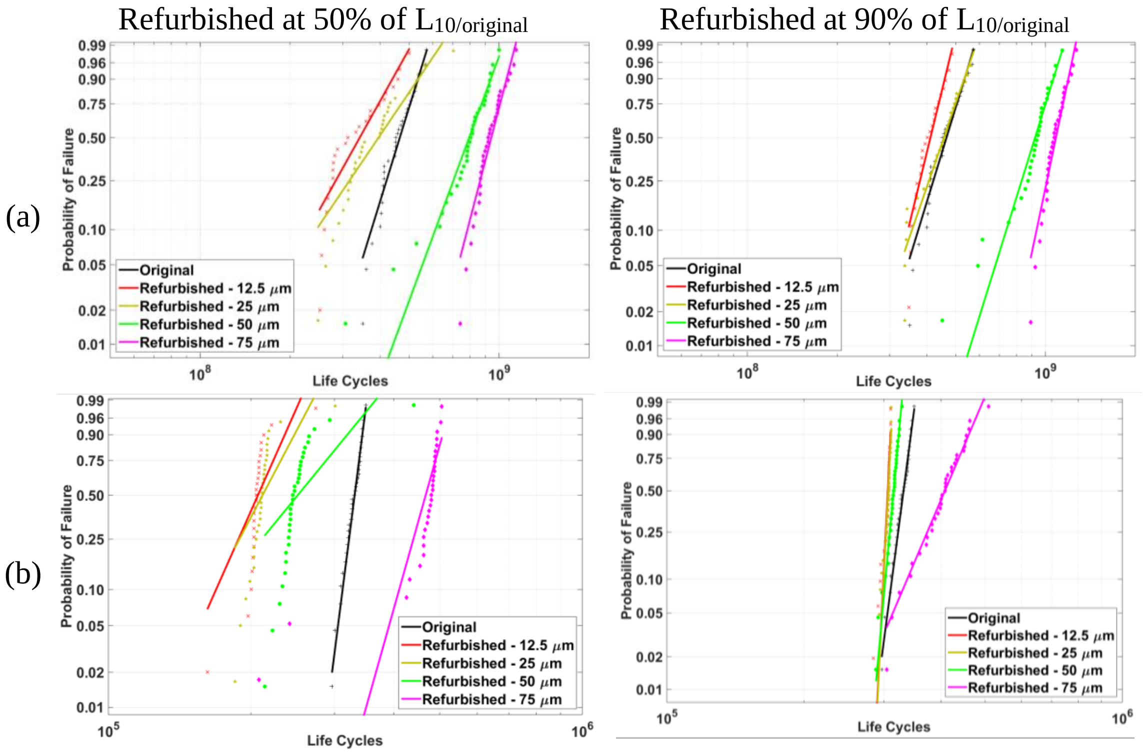

Figure 5.10: Weibull probability plots for refurbished bearings of case carburized steel accounting only for residual stress variation: (a) P_{max} = 2 GPa; (b) P_{max} = 3.5 GPa.

Accounting for both variations simultaneously, the model resulted in the fatigue lives demonstrated in Figure 5.11. The Weibull parameters calculated from the results are presented in Table 5.4 and Table 5.5. It can be observed from the tables that the adverse effect of hardness variation on the fatigue lives of the refurbished bearings dominates the effect of residual stress at a refurbishing depth of 75 µm. The ratio of $L_{10/\mathrm{refurbished}}$ to $L_{10/\mathrm{original}}$ for bearings refurbished after 90% of $L_{10/\mathrm{original}}$ reduces to 1.52 for case carburized steel at P_{max} = 2 GPa as compared to 1.82 for through hardened steel. At a refurbishing depth of 50 µm, however, the refurbishing effectiveness is higher in the case of carburized bearings due to higher compressive residual stresses at the critically stressed region (Figure 5.5(b)). The ratio of $L_{10/\mathrm{refurbished}}$ to $L_{10/\mathrm{original}}$ is 1.45 for case carburized steel compared to 1.39 for through hardened steel.

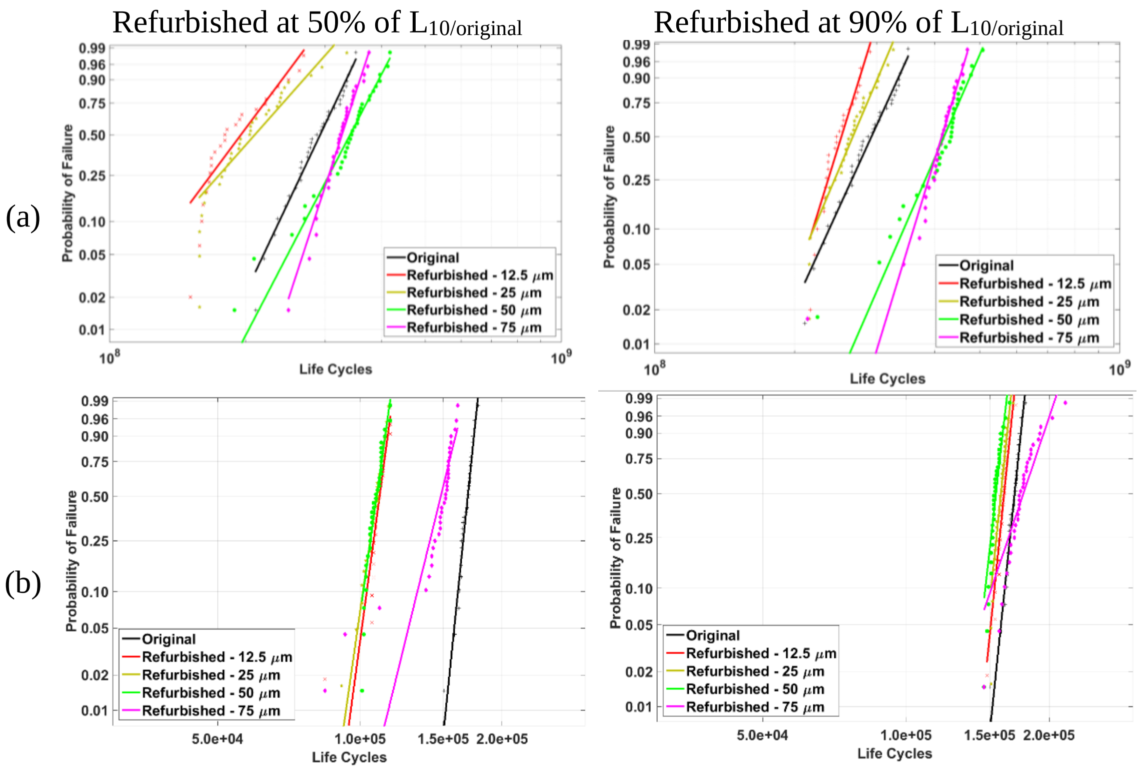

Refurbished at 50% of $L_{10/original}$

Refurbished at 90% of $L_{10/original}$

Figure 5.11: Weibull probability plots for refurbished bearings of case carburized steel (Case depth = 500μm) accounting for both yield strength and residual stress variation: (a) P_{max} = 2 GPa; (b) P_{max} = 3.5 GPa.

It should be noted that the ratio of the refurbishing depth and case depth significantly affects the RCF lives of the refurbished case carburized bearings. If the case depth is larger compared to the refurbishing depth, the fatigue performance of the refurbished bearing would increase as the adverse effect of hardness gradient reduces. In order to investigate the effect of case depth on refurbishing life, additional test cases were simulated with case depth of 1000 μm while keeping the contact half width fixed at 100 μm. The Weibull plots of the RCF lives for these test cases are depicted in Figure 5.12 and the parameters are listed in Table 5.6 and Table 5.7. In this case, the refurbishing effectiveness is higher than the through hardened bearings. This can be attributed to reduction in the hardness gradient as well as the higher compressive stresses at the critically stressed region due to larger case depth. Furthermore, since the peak residual stress occurs deeper in this case as compared to the case depth of 500 μm, the refurbishing effectiveness is greater for refurbishing depth of 75 μm than that of 50 μm.

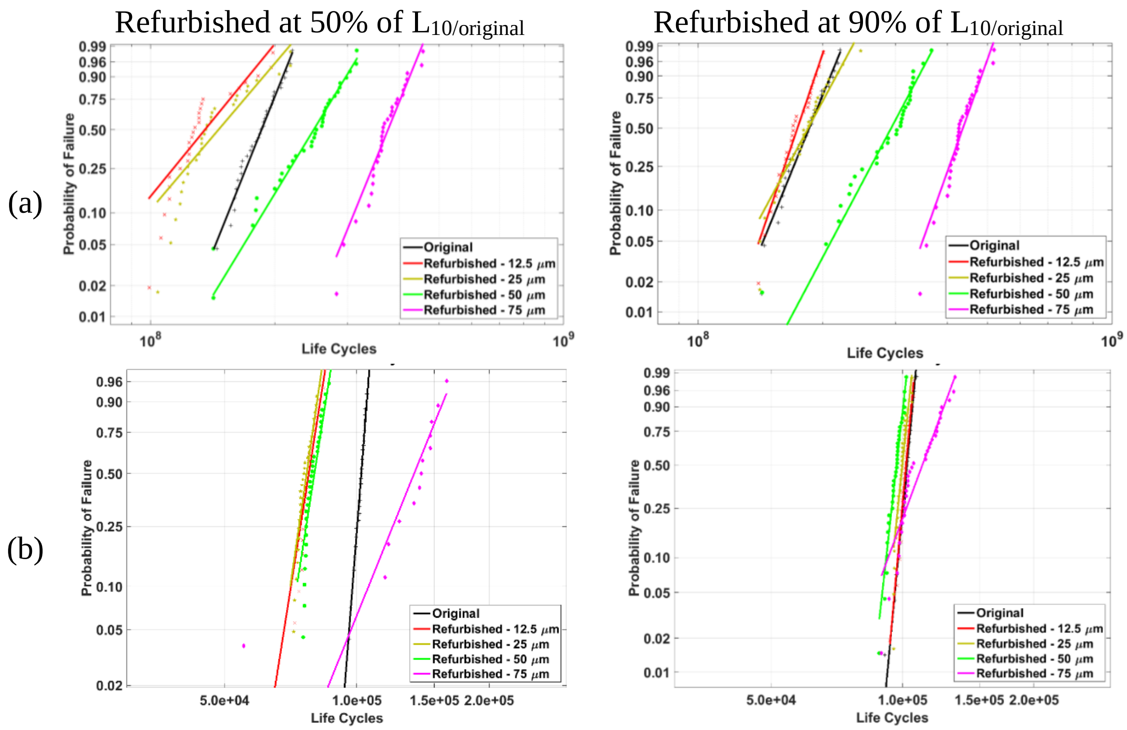

Figure 5.12: Weibull probability plots for refurbished bearings of case carburized steel (Case depth = 1000μm) accounting for both yield strength and residual stress variation: (a) P_{max} = 2 GPa; (b) P_{max} = 3.5 GPa.

These results also signify an important difference between refurbishing through hardened and case carburized bearings. For through hardened bearings, larger the refurbishing depth would yield more RCF life for refurbished bearing and the fatigue life after refurbishing would approach the pristine when all the accumulated damage before refurbishing is removed (refurbishing depth > b). This is, however, not true for case carburized bearings since the refurbishing process removes the hardened case region. Therefore, there is an optimum refurbishing depth for case carburized bearings which is related to the original case depth and contact half-width.

The model suggests that for the case depths and contact half widths studied in this chapter, refurbishing bearings exposed to higher loads (P_{max} = 3.5 GPa) may not always restore full RCF life when comparing the predicted performance of the refurbished bearing with the original bearing. However, this is highly dependent upon assumptions in the modeled material, contact conditions, and amount of material removed in the refurbishing process.

Table 5.4: Predicted Weibull slopes and L_{10} lives for refurbished bearings with case carburized steel (case depth = 500μm) at P_{max} = 2 GPa.

	Refurbished after 50% of $L_{10/orig}$			Refurbished after 90% of $L_{10/orig}$		
Refurbishing Depth	L_{10} Life (Cycles)	$\frac{L_{10/refurb}}{L_{10/orig}}$	Weibull Slope	L_{10} Life (Cycles)	$\frac{L_{10/refurb}}{L_{10/orig}}$	Weibull Slope
Pristine	2.37E+08	-	9.04	2.37E+08	-	9.04
12.5 μm	1.40E+08	0.59	5.74	2.19E+08	0.92	13.35
25 μm	1.41E+08	0.59	4.82	2.20E+08	0.93	9.71
50 μm	2.71E+08	1.14	8.2	3.43E+08	1.45	9.48
75 μm	2.82E+08	1.19	13.1	3.60E+08	1.52	13.56

Table 5.5: Predicted Weibull slopes and L_{10} lives for refurbished bearings with case carburized steel (case depth = 500μm) at P_{max} = 3.5 GPa.

	Refurbished after 50% of $L_{10/orig}$			Refurbished after 90% of $L_{10/orig}$		
Refurbishing Depth	L_{10} Life (Cycles)	$\frac{L_{10/refurb}}{L_{10/orig}}$	Weibull Slope	L_{10} Life (Cycles)	$\frac{L_{10/refurb}}{L_{10/orig}}$	Weibull Slope
Pristine	1.61E+05	-	39.55	1.61E+05	-	39.55
12.5 μm	1.03E+05	0.64	30.22	1.53E+05	0.95	40.43
25 μm	1.01E+05	0.63	28.46	1.51E+05	0.94	39.88
50 μm	1.02E+05	0.63	28.97	1.47E+05	0.91	36.47
75 μm	1.32E+05	0.82	16.56	1.51E+05	0.94	12.19

Table 5.6: Predicted Weibull slopes and L_{10} lives for refurbished bearings with case carburized steel (case depth = 1000μm) at P_{max} = 2 GPa.

	Refurbished after 50% of $L_{10/orig}$			Refurbished after 90% of $L_{10/orig}$		
Refurbishing Depth	L_{10} Life (Cycles)	$\frac{L_{10/refurb}}{L_{10/orig}}$	Weibull Slope	L_{10} Life (Cycles)	$\frac{L_{10/refurb}}{L_{10/orig}}$	Weibull Slope
Pristine	1.54E+08	-	10.16	1.54E+08	-	10.16
12.5 μm	9.28E+07	0.60	4.98	1.49E+08	0.97	12.23
25 μm	9.86E+07	0.64	4.79	1.45E+08	0.94	7.69
50 μm	1.87E+08	1.21	6.68	2.30E+08	1.49	7.81
75 μm	3.11E+08	2.02	9.99	3.71E+08	2.40	11.60

Table 5.7: Predicted Weibull slopes and L_{10} lives for refurbished bearings with case carburized steel (case depth = 1000μm) at P_{max} = 3.5 GPa.

	Refurbished after 50% of $L_{10/orig}$			Refurbished after 90% of $L_{10/orig}$		
Refurbishing Depth	L_{10} Life (Cycles)	$\frac{L_{10/refurb}}{L_{10/orig}}$	Weibull Slope	L_{10} Life (Cycles)	$\frac{L_{10/refurb}}{L_{10/orig}}$	Weibull Slope
Pristine	9.78E+04	-	41.17	9.78E+04	-	41.17
12.5 μm	7.09E+04	0.72	20.18	9.75E+04	1.00	43.13
25 μm	7.06E+04	0.72	22.00	9.50E+04	0.97	37.33
50 μm	7.30E+04	0.75	20.38	9.18E+04	0.94	34.65
75 μm	1.06E+05	1.09	7.90	9.28E+04	0.95	10.51

5.3.3 Comparison of spall patterns

Figure 5.13 and Figure 5.14 illustrate the spall patterns obtained from the model for different refurbishing depths for through hardened and case carburized bearings, respectively, for the same microstructure domain. Bearings were refurbished after 50% of $L_{10/original}$ in both cases. Here, the red area represents the material elements for which the damage value is more than 0.999, i.e. the effective stiffness of these material elements is close to 0. It can be observed that for refurbishing depths of 12.5 and 25 μm, the spall shapes were very similar to those of the unrefurbished bearing. The depth below the original surface where the damage initiates was also the same. This is expected, since the critical damage that occurred prior to refurbishing would be still present in the refurbished microstructure at these refurbishing depths. But for refurbishing depths of 50 and 75 μm, the spalls initiate at around 0.5b (50 μm) below the refurbished surface, since the initial critically damaged material has been removed during grinding. Comparing the spall patterns for through hardened and case carburized material, the patterns are nearly the same except for the refurbishing depth of 75 μm. In that case, the spall in the case carburized steel appears to initiate deeper in the material.

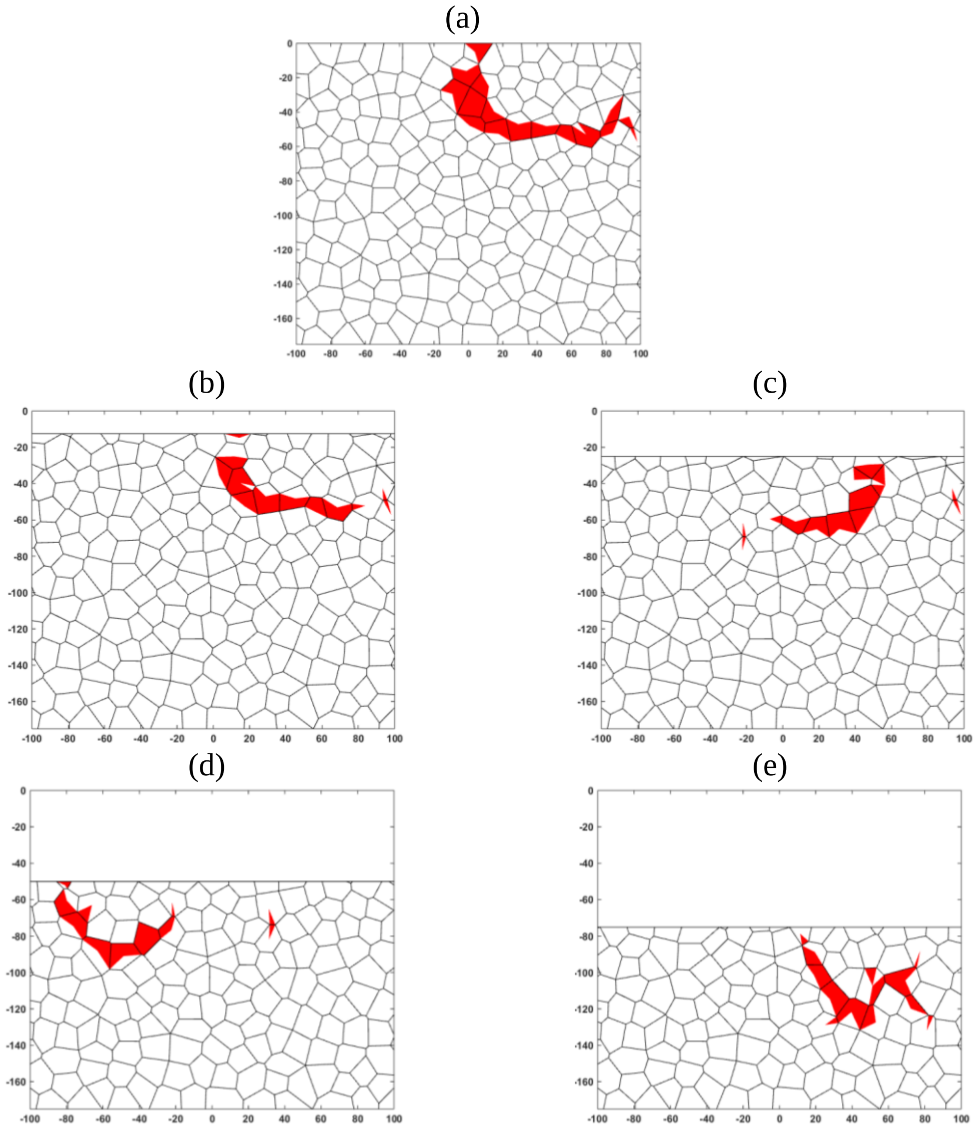

Figure 5.13: Spall patterns obtained from the model for through hardened steel at P_{max} = 2 GPa. Bearing refurbishing was conducted after 50% of $L_{10/original}$. (a) No refurbishing, (b) Refurbished – 12.5 µm, (c) Refurbished – 25 µm, (d) Refurbished – 50 µm, (e) Refurbished – 75 µm.

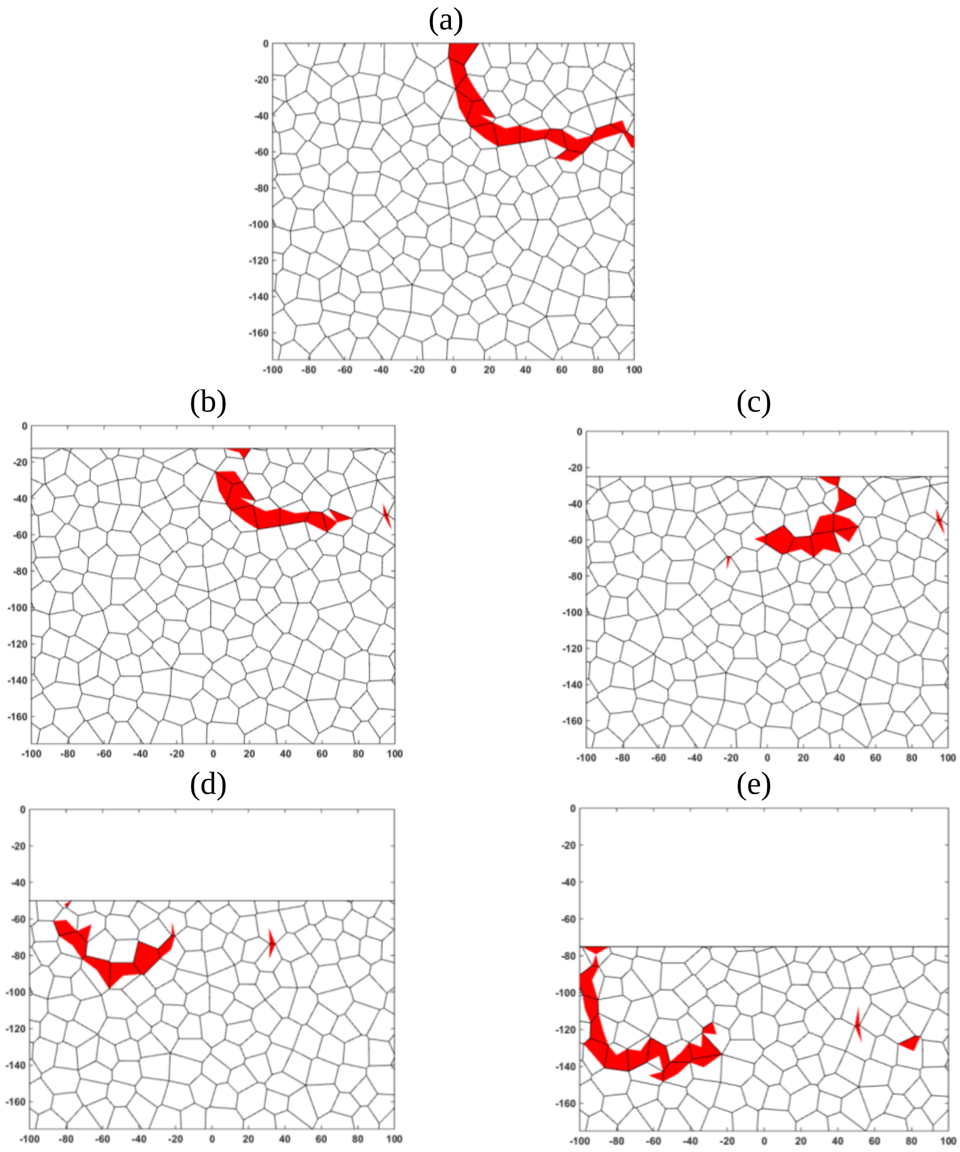

Figure 5.14: Spall patterns obtained from the model for case carburized steel at P_{max} = 2 GPa. Bearing refurbishing was conducted after 50% of $L_{10/original}$. (a) No refurbishing, (b) Refurbished – 12.5 μm, (c) Refurbished – 25 μm, (d) Refurbished – 50 μm, (e) Refurbished – 75 μm.

5.4 Summary and Conclusions

This chapter presents a numerical model to analyze the RCF lives of refurbished bearings made from case carburized steel. The focus of the study was to investigate whether refurbishing case carburized bearings is useful to extend their fatigue life. Gradients in hardness and residual stress distribution typically observed in case carburized material were also taken into account in the model. The hardness was modeled using the linear correlation between hardness and yield strength. A linear elastic kinematic plastic material model was incorporated in the finite element solver. Progressive degradation of material due to rolling contact fatigue was captured using damage mechanics. Scatter in fatigue life due to randomness in the material microstructure was simulated using Voronoi tessellations. Refurbishing was simulated by removing a layer of surface (0.125, 0.25, 0.5 and 0.75b) from the microstructural domain, but the damage in the remaining domain due to fatigue cycles before refurbishing was retained. The refurbished microstructure was again simulated using the fatigue damage model under RCF loading until the damage was observed. It should be noted that the current model does not account for the residual stresses or changes in material properties during the refurbishing process. The compressive residual stresses induced by the regrinding of the bearing surface can have a beneficial impact on the fatigue performance of the refurbished bearing. However, this factor is ignored in the current modeling.

The model compared case carburized steel against through hardened steel with respect to the RCF performance of refurbished bearings. It was found that increasing depths of refurbishing beyond 0.5b enhances the RCF life of the refurbished bearings for small loads (Pmax = 2 GPa). Further, refurbishing the bearing earlier (50% of $\mathrm{L}_{10/\mathrm{original}}$) increases the fatigue life of the refurbished bearings. However, the total life of the refurbished bearing is greater if the bearings are refurbished after 90% of $\mathrm{L}_{10/\mathrm{original}}$.

According to the results obtained from the model, the ratio of total L10 life of the refurbished bearings to $\mathrm{L}_{10/\mathrm{original}}$ is higher for through hardened bearings than for case carburized bearings with case depth of 500 µm. This is attributed to the removal of the surface layer, which has higher fatigue resistance, and exposing the soft core to fatigue stress. However, this effect reduces as the case depth increases relative to contact half width; therefore the effectiveness of refurbishing for larger case depth (1000 µm) is more than the through hardened bearings. The model also suggested that it is not beneficial to refurbish bearings exposed to a higher load (P_{max} = 3.5 GPa) for the case depths and contact half width studied in this chapter since for higher load the total RCF life of the refurbished bearing is less than the total life of the original bearing.

6. SUMMARY, CONCLUSIONS, AND RECOMMENDATIONS FOR FUTURE RESEARCH

6.1 Summary and Conclusions

This dissertation investigated material response to two types of fatigue damages often experienced by machine components containing contact bodies: fretting fatigue and rolling contact fatigue (RCF). Chapter 1 presented a comprehensive literature review of two types of fatigue phenomena that commonly occur in contacting bodies. The topic of fretting fatigue and rolling contact fatigue were introduced with brief historical background, machine elements frequently affected by them, mechanism of their manifestations and comparison with classical fatigue phenomenon. Relevant empirical, analytical, and numerical models previously developed to predict RCF and fretting fatigue failures in machine components were also reviewed.

In Chapter 2, the fretting fatigue behavior of AISI 4140 vs. Ti-6-4 was studied experimentally in a cylinder-on-flat contact configuration. For this purpose, a fretting test fixture was designed and developed which was coupled with an MTS machine to impose the fretting fatigue damage. Fretting fatigue experiments were conducted under completely (R=-1) reversed axial stress amplitudes, a constant maximum Hertzian Pressure (P_h) of 3 GPa and at a frequency of 5 Hz. A fretting test in gross slip regime was performed to determine the friction coefficient for the current experimental configuration. The critical damage value for AISI 4140 was extracted using the method of variation of elasticity modulus. A finite element model was developed incorporating damage mechanics constitutive relations to simulate fatigue degradation and Voronoi tessellation to account for the geometric randomness of the material microstructure. Alternating normal stress resolved on the Voronoi cell boundary was used as the damaging criterion. Friction coefficient of 0.6 and critical damage value of 0.12 obtained from the experiments were used in the simulations. Fretting fatigue lives predicted from the analytical model showed good agreement with the measured experimental results.

The third chapter presented a new computationally efficient approach to investigate RCF life scatter and spall formation in large line contacts. This model was built on the previously developed RCF model which incorporated continuum damage mechanics to capture progressive fatigue damage and Voronoi tessellations to study the variability occurring due to the randomness in material microstructure. To make this model computationally efficient, Voronoi tessellation and finite element model was decoupled by using Delaunay triangulation to generate the FE mesh. Use of a Delaunay mesh significantly reduced the simulation time compared to the previous approach. A mapping procedure was developed to communicate the state of stress and damage between FE mesh and Voronoi tessellations. Further, a remeshing tool was built to dynamically refine the Delaunay triangle mesh around the damaged elements in order to capture the stress concentration accurately. The new modeling approach enabled simulation of RCF in line contacts of widths up to 1 mm. For fixed contact pressures, the simulated RCF lives were shown to increase with increase in the half contact width. The ratio of L_{10} lives for different sized bearings computed from the model correlated well with the formula derived from the basic life rating for radial roller bearing as per ISO 281. The model was then extended to study the effect of initial internal voids on RCF life. It was found that for the same initial void density, the L_{10} life decreases with the increase in the bearing size.

In Chapter 4, an elastic-plastic finite element model based on micro-indentation tests developed to investigate the rolling contact fatigue of case carburized steels was presented. It employed Mises based plasticity model with kinematic hardening to incorporate the effect of material plasticity. The hardness gradient in the material was modeled by changing the yield strength as a function of depth. Linear relationship between hardness and yield strength was assumed. The FE model was coupled with continuum damage mechanics approach to capture material degradation due to fatigue damage. It considers both; stress and accumulated plastic strain based damage evolution laws for fatigue failure initiation and propagation. The effects of residual stress distribution due to carburization process on fatigue damage progression were modeled by modifying the damage evolution law. Material dependent parameters used in the damage evolution laws were determined using the SN results for torsional fatigue of the bearing steel. Similar to fatigue damage models developed in previous chapters, this model also accounted for the effects of topological randomness in the material microstructure through the use of Voronoi tessellations. The model was used to compare the rolling contact fatigue (RCF) lives of through hardened and case carburized bearing steel with different case depths at contact pressures ranging from 2 to 3.5 GPa. The results showed that the optimum case depth for which maximum RCF lives were 6.2b for P_{max}= 2 GPa and 7.6b for P_{max}= 3.5 GPa. The spall shapes and the depth below the surface where damage initiates were found to be dependent on the case depth.

Chapter 5 built upon the model developed in chapter 4 with a modification to quantify the RCF lives of refurbished bearings made from case carburized steel. In order to simulate the refurbishing process, damage accumulation was calculated for a set number of fatigue cycles with the original bearing geometry. A layer of the original surface was then removed, but the fatigue damage accumulated prior to refurbishing was preserved. The yield strength and residual stresses in the remaining material were assumed to be the same as the original material. The refurbished geometry was then subjected to additional fatigue cycles until the damage was detected. The model was used to compare the RCF lives of refurbished bearings made from through hardened and case carburized bearing steel at contact pressures ranging from 2 to 3.5 GPa. The number of fatigue cycles prior to the refurbishing and the depth of material removal were varied to analyze their influence on refurbished life. It was found that greater regrinding depth (more than 0.5 times the half-width) and more fatigue cycles prior to refurbishing enhanced the total fatigue life of refurbished bearings. The model predicted that the ratio of the total RCF life of refurbished bearing to that of unrefurbished bearing is more for through hardened bearings than case carburized bearings with case depth of 500 μm. This was expected, because the material properties are uniform with depth in through hardened steel, therefore material properties in the critically stressed region are not affected by refurbishing. In the case hardened bearing steel, however, the refurbishing process removes part of the hardened case region and exposes the softer material to the critical stress which reduces the fatigue performance of the refurbished bearing. Since this effect diminishes as the case depth increases; the increase in the fatigue life after refurbishing was found to be larger for case carburized bearings with case depth of 1000 μm than through hardened bearings.

6.2 Recommendations for Future Work

The fatigue damage models developed and presented in this dissertation have demonstrated an excellent capacity for predicting the fretting fatigue and rolling contact fatigue behavior of machine components by taking into account the microstructure topology and the some of the mechanical properties of the material. However, accurately modeling all aspect of reality is difficult therefore; these models were built on some simplifying assumptions which were essential to developing a computationally feasible modeling approach. Some of the major assumptions include homogenous, isotropic material and idealized contact pressure. In reality, steels used to manufacture machine components consist of multiple phases due to heat treatment. These phases can also transform during the life of the machine component depending on the operating load, temperature, etc. Furthermore, the pressure distribution between contacting bodies depend on speed, applied load, lubricant viscosity, temperature, surface roughness, presence of surface defects etc. Material degradation due to fatigue increases the deformation, which further modifies the pressure profile. These changes, in some cases can significantly influence the state of stress in the material causing significant variation in fatigue lives of the machine components. Therefore, there is great scope for improvements to the fatigue damage models presented in this dissertation to achieve the goal of developing an accurate tool to predict the fatigue life of machine components.

6.2.1 Effects of Residual Stress Evolution on RCF

The beneficial effects of compressive residual stresses on fatigue life have been a focus of research interest since many years. Most commonly, residual stresses are produced by processes used to form and fabricate them into engineering components. Examples of these processes are welding, forging, rolling, grinding, machining, etc. Residual stresses are imparted by inducing plastic deformation in the material through severe temperature gradients or mechanical forces. Another common source of residual stresses, which is not the direct result of plastic deformation, is localized permanent elastic expansion or contraction of the metallic lattice by heat treatment which induces phase transformation. Case carburization is one such process which has become increasing more popular in high-performance ball and rolling element bearing applications. In Chapter 4, rolling contact fatigue damage model for case carburized steel was presented. However, this investigation assumed that distribution of residual stresses do not vary with cycles. However, the residual stress distribution in the bearing material evolves during the operation due to the loading and other microstructural phenomena.

Retained austenite (RA) is the austenite that does not transform to martensitic phase upon quenching. The RA in the bearing microstructure exhibits metastablilty at ambient temperatures and undergoes a phase transformation during RCF. These transformations are accompanied by volume expansion of approximately 4 percent caused by the RA changing from the face-centered cubic lattice structure to a martensitic body centered tetragonal or body centered cubic structure. The volume expansion induces compressive residual stresses in the material. Voskamp [146] have studied the decomposition of RA and corresponding variation in residual stresses during RCF. Figure 6.1: Decomposition of retained austenite and evolution of residual stresses with fatigue cycles. demonstrates the evolution of residual stress due to RA transformation during RCF. There is a general agreement among researchers that there exist an optimum austenite content that results in the highest fatigue endurance. Additionally, the microscale plasticity due to the fatigue loading causes residual stress relaxation. The demand for greater reliability of tribological components has focused attention on understanding the sources of residual stresses and their interactions with applied stresses to affect material fatigue. Therefore, it is important to study and analyze the evolution of residual stresses.

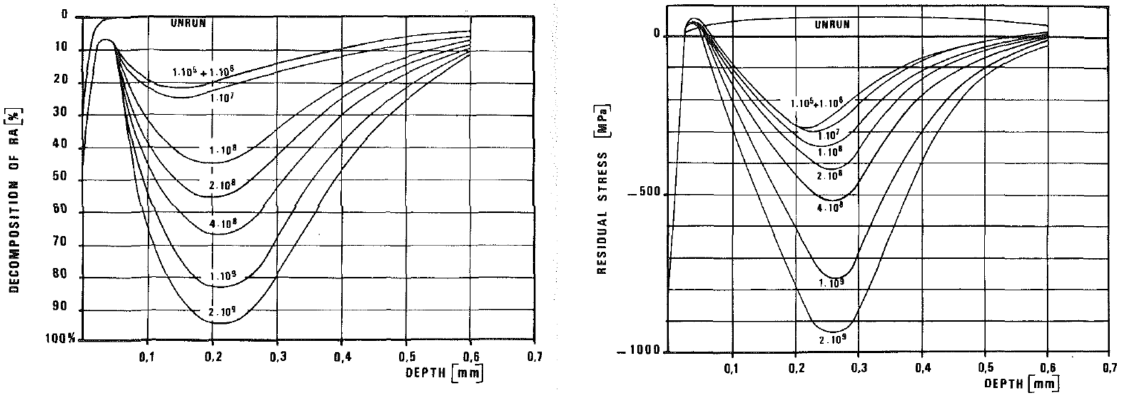

Figure 6.1: Decomposition of retained austenite and evolution of residual stresses with fatigue cycles.

Some preliminary experiments for this investigation were conducted during the course of this research at Mechanical Engineering Tribology Laboratory of Pursue University. Using the equivalence between RCF and torsion fatigue ([30], [97], [113]), the variation in residual stresses due to stress cycles were analyzed using torsion fatigue test rig ([147]). The test specimens were fatigued for a preset number of cycles at 3 different load levels – 0.8 S_{us}, 0.6 S_{us}, 0.4 S_{us}. The preset number of cycles for each load level was chosen based on the SN curve of the material (Figure 6.2(a)). After the torsion testing, the sub-surface residual stress distributions on the fatigued specimen were measured using XRD at four different depths: 12.7µm, 25.4µm, 50.8µm and 76.2µm. Please note that a new specimen needed tested for each data point as XRD technique for RS measurement is destructive. Also, the depths where RS measurements are performed are very close to the surface, hence the shear stress experienced by the material points at these depth can be assumed to be the same as the maximum shear stress at the cross-section. At 0.4 S_{us}, as the fatigue cycles increase, the residual stress values increase (more negative) at all depths, which can be attributed to the volume expansion due to RA transformation. At 0.6 $S_{us,}$ however, the magnitude of residual stress increases till cycle number 10 then start to decrease (less negative). The initial increase in the residual stresses can be explained by the RA decomposition while the decrease in the magnitude can be caused by stress relaxation due to microscale plasticity. Since plasticity does not occur at low loads, it can be inferred that the decrease in the magnitude was not observed at 0.4 S_{us}. The effect of microscale plasticity on stress relaxation is more evident at higher load of 0.8 $S_{us.}$ It can also be observed that the initial magnitude of residual stress also play a role in determining the rate of change in residual stresses.

Future work in this regard should involve performing more experiments with different initial residual stress distribution and RA content. The RA composition in the material at different cycles also need be measured. From the experimental results, an equation the evolution of residual stresses with fatigue cycles cycles, N may be derived in terms of state of stress, initial RA composition, and residual stress similar to the following:

$$\sigma_{RS}(N) = \sigma_{RS}(0) + \alpha_1 (\% \, RA)^{\zeta_1} + \alpha_2 \left(\frac{\sigma'}{S_y} \right)^{\zeta_2} \tag{6.1}$$

The RCF model for case carburized steels presented in Chapter 4 should be modified to account for the variation in the residual stresses with fatigue cycles. From the model results, optimal residual stress distribution to enhance the RCF lives can be estimated.

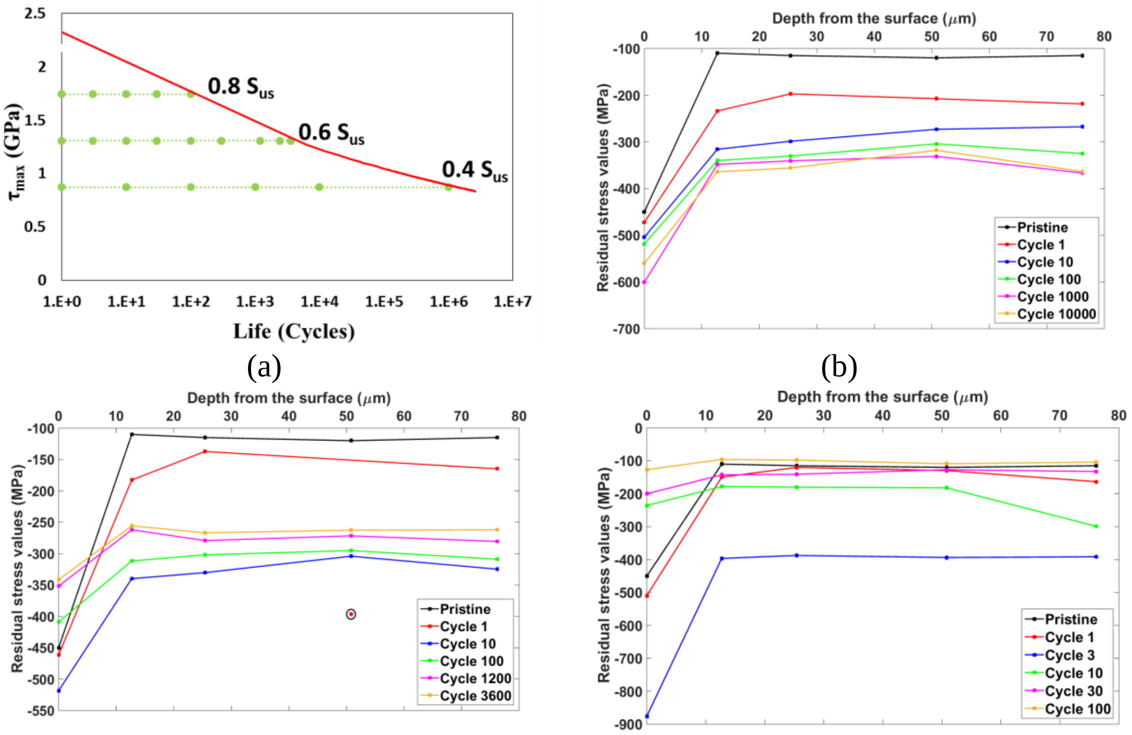

(a) (b)

(c) (d)

Figure 6.2: (a) Data points for residual stress measurement using XRD; Evolution of residual stress during torsion fatigue at (b) 0.4S_{us} , (c) 0.6S_{us}, (d) 0.8S_{us}.

6.2.2 3D RCF Modeling of Large Bearing Contacts

Two-dimensional representations of materials are commonly used in the formulation of RCF models. This is because the contact geometry can usually be approximated as infinitely wide. However, the grains of the material microstructure are three dimensional. Furthermore, the contact geometry in the RCF experiments is often elliptical which produce spall which have 3D shapes. Figure 6.3 depicts the rendition of the spalls obtained during RCF experiments. The existing 3D rolling contact fatigue damage models incorporated 3D representations of the subsurface material topology. However, these studies only considered line contact geometry in 3D and simulated contact half-width of 50 μm. The contact sizes in large bearings can be as large as 1000 μm. The typical contact sizes in RCF experiments are also in range of 200-400 μm. The existing 3D RCF models becomes computationally infeasible for contact sizes beyond 50 μm. In Chapter 3 of this dissertation, a modified approach for 2D RCF studies of large bearings was presented. As in 2D, the computational costs of using the Voronoi meshes in the FE solver for large contacts are enormous since the number of nodes and elements increases with cube of contact half-width. The 2D RCF model for large bearings incorporates decoupling of Voronoi mesh representing material microstructure and the FE mesh. Similar approach can be implemented in 3D RCF model to develop a computationally efficient model that can simulate large elliptical contacts. The stress mapping procedure for communicating stress and damage information between Delaunay and Voronoi mesh developed for 2D elements in Chapter 3 can be modified to work for 3D meshes. This model can also be used to study the effects of material defects and inclusion sizes, white etching bands on the large bearings.

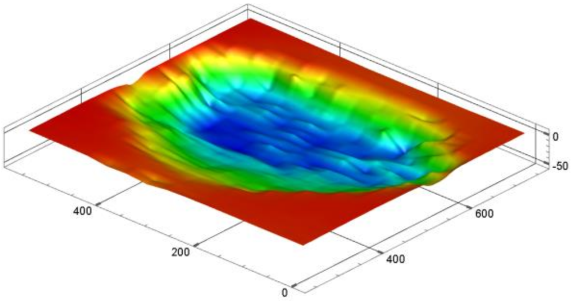

Figure 6.3: 3D rendition of a spall observed in 8620 steel at 3.6GPa of maximum Hertzian pressure during 3-ball-on-rod tests [148].

6.2.3 Effects of EHL Pressure on RCF in Case Carburized Bearings Incorporating Surface Dents

Most of the RCF damage models including those presented in this dissertation assume idealized Hertzian pressure between contacting bodies. However, this assumption is only applicable to dry contact conditions, whereas, bearings operate in the presence of a lubricant. As the speed increases the wedge effect of the lubricant at the inlet becomes significant. Lubricant properties and temperature also play an important role in deciding the lubrication regime. Pressure profile between contacting bodies during elastohydrodynamic lubrication (EHL) regime differs considerably from the Hertzian pressure. As mentioned in Chapter 4, case carburized material is characterized by hardened outer layer and residual stresses in the case region. These characteristics can also significantly influence the pressure profile. Furthermore, when debris enters an EHL contact, it indents the mating surfaces. Depending on the material properties of the debris (i.e. whether it is ductile or brittle) the dent generated by the debris can be either large and shallow or small with sharp edges. However, due to the plastic deformation of the surfaces, residual stresses are generated around the dent, which affect the sub-surface-stress distribution. Case carburized material is supposed to provide better resistance to the plastic deformation due to the debris due to improved hardness at the surface.

Paulson et al. [149] developed a coupled finite element EHL and damage mechanics model to investigate the effects of EHL pressure profile in RCF lives. The modeling approach for case carburized material presented in this dissertation can implemented in the model developed by Paulson et al. [150]. This model may be used to investigate spall initiation and propagation from the surface dent in case carburized material and evaluate its performance against through hardened material.

6.2.4 Effects of grain size on RCF

It is well established that material properties are related to the grain size. Hall–Petch equation [150] given in Equation (6.2) relates yield stress of the material to the grain size, (d in microns) for conventional metals with grains at micron scale.. ${S_y}_o$, k are the material constants independent of grain size. The equation indicates that the decrease of grain size will improve the mechanical properties of the material.

$$S_y = {S_y}_o + \frac{k}{d^{0.5}} \tag{6.2}$$

The material constants in Equation (6.2) should be evaluated from torsion experiments on bearing steel with different prior austenite grain sizes. In Chapter 4, the hardness gradient in the case carburized material was simulated using the relationship between hardness and yield strength. Damage parameters for different yield strengths were also evaluated. Similarly, the yield strength and the corresponding damage parameters can be calculated for the material with different grain sizes. The model results may be considered to estimate the best grain size for bearing materials to maximize their RCF performance.

REFERENCES

[1] T. A. Harris, *Rolling Bearing Analysis*. Wiley: New York, 2001.

[2] W. E. Littmann, “The Mechanism of Contact Fatigue,” *NASA Spec. Report, SP-237*.

[3] W. E. Littmann and R. L. Widner, “Propagation of Contact Fatigue from Surface and Subsurface Origins,” *J. Basic Eng.*, vol. 88, no. 3, pp. 624–636, 1966.

[4] A. F. Bower, “The Influence of Crack Face Friction and Trapped Fluid on Surface Initiated Rolling Contact Fatigue Cracks,” *J. Tribol.*, vol. 110, no. 4, p. 704, 1988.

[5] B. Lou, L. Han, Z. Lu, S. Liu, and F. Shen, “he rolling contact fatigue behaviors in carburized and hardened steel,” *Fatigue 90 Proc. Fourth Int. Conf. Fatigue Fatigue Threshold.*, pp. 627–632, 1990.

[6] V. Bhargava, G. T. Hahn, and C. A. Rubin, “Rolling contact deformation and microstructural changes in high strength bearing steel,” *Wear*, vol. 133, no. 1, pp. 65–71, 1989.

[7] F. Sadeghi, B. Jalalahmadi, T. . Slack, N. Raje, and N. K. Arakere, “A review of rolling contact fatigue,” *J. Tribol.*, vol. 131, no. 4, p. 41403, 2009.

[8] A. Palmgren, “Ball and roller bearing engineering,” *Philadelphia SKF Ind. Inc*, vol. 1959, no. 1, 1959.

[9] “ISO 281: Rolling bearings — Dynamic load ratings and rating life,” *ISO Stand.*, vol. 3, no. May, 2007.

[10] G. Lundberg and A. Palmgren, “Dynamic Capacity of Rolling Bearings,” *Acta Polytech. Mech. Eng. Ser. R. Swedish Acad. Eng. Sci.*, vol. 1, no. 3, pp. 1–52, 1947.

[11] G. Lundberg and A. Palmgren, “Dynamic Capacity of Roller Bearings,” *Acta Polytech. Mech. Eng. Ser. R. Swedish Acad. Eng. Sci.*, vol. 2, no. 4, pp. 96–127, 1952.

[12] E. Ioannides and T. A. Harris, “A New Fatigue Life Model for Rolling Bearings,” *J. Tribol.*, vol. 107, no. 3, p. 367, 1985.

[13] E. Ioannides, G. Bergling, and A. Gabelli, “An analytical formulation for the life of rolling bearings,” *Acta Polytech. Scand. Mech. Eng. Ser.*, vol. 137, no. 58–60, 1999.

[14] E. V. Zaretsky, “Design for life, plan for death,” *Mach. Des.*, vol. 66, no. 15, pp. 55–59, 1994.

[15] L. M. Keer and M. D. Bryant, "A Pitting Model for Rolling Contact Fatigue," *Journal of Lubrication Technology*, vol. 105, no. 2. p. 198, 1983.

[16] T. E. Tallian, "Simplified contact fatigue life prediction model – Part II: New model," *J. Tribol.*, vol. 114, pp. 214–222, 1992.

[17] M. T. Hanson and L. M. Keer, "An Analytical Life Prediction Model for the Crack Propagation Occuring in Contact Fatigue," *Tribol. Trans.*, vol. 35, no. 2, pp. 451–461, 1992.

[18] R. S. Zhou, "Surface Topography and Fatigue Life of Rolling Contact Bearing," *Tribol. Trans.*, vol. 36, pp. 329–340, 1993.

[19] R. S. Zhou, H. S. Cheng, and T. Mura, "Micropitting in Rolling and Sliding Contact Under Mixed Lubrication," *J. Tribol.*, vol. 111, no. 4, p. 605, 1989.

[20] Y. Jiang and H. Sehitoglu, "A model for rolling contact failure," *Wear*, vol. 224, no. 1, pp. 38–49, 1999.

[21] H. Sehitoglu and Y. Jiang, "Fatigue and stress analyses of rolling contact," *Tech. Report, Mater. Eng. - Mech. Behav. Coll. Eng. Univ. Illinois Urbana-Champaign*, 1992.

[22] K. J. Miller, "A historical perspective of the important parameters of metal fatigue and problems for the next century," *Fatigue '99 Proc. Seventh Int. Fatigue Congr. Beijing, China*, pp. 15–39, 1999.

[23] N. Raje, F. Sadeghi, J. Rateick, G. Richard, and M. R. Hoeprich, "A Numerical Model for Life Scatter in Rolling Element Bearings," *J. Tribol.*, vol. 130, no. 1, p. 11011, 2007.

[24] D. L. McDiarmid, "A General Crierion For High Cycle Multiaxial Fatigue Failure," *Fatigue Fract. Eng. Mater. Struct.*, vol. 14, no. 4, pp. 429–453, 1991.

[25] D. L. McDiarmid, "A Shear Stress Based Critical- Plane Criterion of Multiaxial Fatigue Failure for Design and Life Prediction," *Fatigue Fract. Eng. Mater. Struct.*, vol. 17, no. 12, pp. 1475–1484, 1994.

[26] L. Susmel and P. Lazzarin, "A bi-parametric Wohler curve for high cycle multiaxial fatigue assessment," *Fatigue Fract. Eng. Mater. Struct.*, vol. 25, no. 1, pp. 63–78, 2002.

[27] N. Raje, F. Sadeghi, and R. G. Rateick, “A Statistical Damage Mechanics Model for Subsurface Initiated Spalling in Rolling Contacts,” *J. Tribol.*, vol. 130, no. 4, p. 42201, 2008.

[28] L. Kachanov, “Rupture Time Under Creep Conditions,” *Int. J. Fract.*, vol. 97, no. 8, pp. 11–18, 1999.

[29] B. Jalalahmadi and F. Sadeghi, “A Voronoi Finite Element Study of Fatigue Life Scatter in Rolling Contacts,” *J. Tribol.*, vol. 131, no. 2, p. 22203, 2009.

[30] B. Jalalahmadi and F. Sadeghi, “A Voronoi FE Fatigue Damage Model for Life Scatter in Rolling Contacts,” *J. Tribol.*, vol. 132, no. 2, p. 21404, 2010.

[31] N. Weinzapfel, A. Liebel, F. Sadeghi, and V. Bakolas, “A 3D Finite Element Study of Fatigue Life Dispersion in Rolling Line Contacts,” *J. Tribol.*, vol. 133, no. 4, pp. 042202–042202, 2011.

[32] J. A. R. Bomidi, N. Weinzapfel, F. Sadeghi, A. Liebel, and J. Weber, “An Improved Approach for 3D Rolling Contact Fatigue Simulations with Microstructure Topology,” *Tribol. Trans.*, vol. 56, no. January 2015, pp. 385–399, 2013.

[33] A. Warhadpande, F. Sadeghi, M. N. Kotzalas, and G. Doll, “Effects of plasticity on subsurface initiated spalling in rolling contact fatigue,” *Int. J. Fatigue*, vol. 36, no. 1, pp. 80–95, 2012.

[34] J. A. R. Bomidi and F. Sadeghi, “Three-Dimensional Finite Element Elastic–Plastic Model for Subsurface Initiated Spalling in Rolling Contacts,” *J. Tribol.*, vol. 136, no. 1, p. 11402, 2013.

[35] P. A. McVeigh, “Finite element analysis of fretting fatigue stresses,” 1995.

[36] D. Nowell, D. Dini, and D. A. Hills, “Recent developments in the understanding of fretting fatigue,” *Eng. Fract. Mech.*, vol. 73, no. 2, pp. 207–222, 2006.

[37] E. M. Eden, W. N. Rose, and F. L. Cunningham, “The endurance of metals: experiments on rotating beams at University College, London,” *Arch. Proc. Inst. Mech. Eng.*, vol. 81, no. 1, pp. 839–974, 2006.

[38] G. A. Tomlinson, P. L. Thorpe, and H. J. Gough, “An investigation of the fretting corrosion of closely fitting surfaces,” *Proc. Inst. Mech. Eng.*, vol. 141, no. 1, pp. 223–249, 1939.

[39] E. J. Warlow-Davies, “Fretting corrosion and fatigue strength: brief results of preliminary experiments,” *Proc. Inst. Mech. Eng.*, vol. 146, no. 1, pp. 32–38, 1941.

[40] J. R. McDowell, “Fretting of Hardened Steel in Oil,” *ASLE Trans.*, vol. 1, no. 2, pp. 287–295, 1958.

[41] A. J. Fenner and J. E. Field, “A study of the onset of fatigue damage due to fretting,” *Trans. North East Coast Inst. Eng. Shipbuild.*, vol. 76, pp. 183–189, 1960.

[42] K. Nishioka, K. Hirakawa, and S. Nishimura, “Fundamental Investigations of Fretting Fatigue : Part 1,On the Relative Slip Amplitude of Press-fitted Axle Assemblies,” *Bull. JSME*, vol. 11, no. 45, pp. 437–445, 1968.

[43] K. Nishioka and K. Hirakawa, “Fundamental Investigations of Fretting Fatigue:(Part 2, Fretting Fatigue Testing Machine and Some Test Results),” *Bull. JSME*, vol. 12, no. 50, pp. 180–187, 1969.

[44] D. A. Hills, D. Nowell, and J. J. O’Connor, “On the mechanics of fretting fatigue,” *Wear*, vol. 125, no. 1–2, pp. 129–146, 1988.

[45] M. P. Szolwinski and T. N. Farris, “Observation, analysis and prediction of fretting fatigue in 2024-T351 aluminum alloy,” *Wear*, vol. 221, no. 1, pp. 24–36, 1998.

[46] R. Cortez, S. Mall, and J. R. Calcaterra, “Investigation of variable amplitude loading on fretting fatigue behavior of Ti–6Al–4V,” *Int. J. Fatigue*, vol. 21, no. 7, pp. 709–717, 1999.

[47] S. A. Namjoshi, V. K. Jain, and S. Mall, “Effects of shot peening on fretting fatigue behavior of Ti6Al4V,” *J. Eng. Mater. Technol.*, vol. 124, no. 2, pp. 222–228, 2002.

[48] P. Ramasundaram and R. Bowman, “An investigation of fatigue and fracture in NiAl – Mo composites,” *Mater. Sci. Eng. A*, vol. 248, no. 1, pp. 132–146, 1998.

[49] P. Papanikos, “Theoretical and experimental studies of fretting-initiated fatigue failure of aeroengine compressor discs,” *Int. J. Fatigue*, vol. 17, no. 6, p. 449, 1995.

[50] B. P. Conner and T. Nicholas, “Using a Dovetail Fixture to Study Fretting Fatigue and Fretting Palliatives,” *J. Eng. Mater. Technol.*, vol. 128, no. 2, p. 133, 2006.

[51] M. H. Attia and R. B. Waterhouse, *Standardization of Fretting Fatigue Test Methods and Equipment (No. 1159)*. 1992.

[52] “ASTM E2789: Standard Guide for Fretting Fatigue Testing,” *E2789 - 10*, pp. 1–10, 2011.

[53] R. W. Neu, “Progress in standardization of fretting fatigue terminology and testing,” in *Tribology International*, 2011, vol. 44, no. 11, pp. 1371–1377.

[54] C. D. Lykins, “An investigation of fretting fatigue crack initiation behavior of the titanium alloy Ti-6Al-4V,” University of Dayton, 1999.

[55] D. B. Rayaprolu and R. Cook, “A Critical Review of Fretting Fatigue Investigations at the Royal Aerospace Establishment,” in *Standardization of Fretting Fatigue Test Methods and Equipment*, vol. 1159, 1992, pp. 129–152.

[56] R. B. Waterhouse, “Fretting fatigue,” *Elsevier Sci. Technol.*, 1981.

[57] S. Adibnazari and D. W. Hoeppner, “Study of fretting fatigue crack nucleation in 7075-T6 aluminum alloy,” *Wear*, vol. 159, no. 2, pp. 257–264, 1992.

[58] W. J. Harris, “The influence of fretting on fatigue,” *Advis. Gr. Aerosp. Res. Dev. PARIS*, 1970.

[59] K. J. Nix and T. C. Lindley, “The application of fracture mechanics to fretting fatigue,” *Fract. Eng. Mater. …*, vol. 8, no. 2, pp. 143–160, 1985.

[60] S. Faanes, “Inclined Cracks in Fretting Fatigue,” *Eng. Fract. Mech.*, vol. 52, no. 1, pp. 71–82, 1995.

[61] A. E. Giannakopoulos, T. C. Lindley, and S. Suresh, “Aspects of equivalence between contact mechanics and fracture mechanics: theoretical connections and a life-prediction methodology for fretting-fatigue,” *Acta Mater.*, vol. 46, no. 9, pp. 2955–2968, 1998.

[62] P. J. Golden and A. F. Grandt Jr., “Fracture mechanics based fretting fatigue life predictions in Ti-6Al-4V,” *Eng. Fract. Mech.*, vol. 71, no. 15, pp. 2229–2243, 2004.

[63] H. A. Fadag, S. Mall, and V. K. Jain, “A finite element analysis of fretting fatigue crack growth behavior in Ti–6Al–4V,” *Eng. Fract. Mech.*, vol. 75, no. 6, pp. 1384–1399, 2008.

[64] T. N. Farris, “Finite Element Analysis of Fretting Stresses,” *J. Tribol.*, vol. 119, no. 4, p. 797, 1997.

[65] E. Giner, N. Sukumar, F. D. Denia, and F. J. Fuenmayor, “Extended finite element method for fretting fatigue crack propagation,” *Int. J. Solids Struct.*, vol. 45, no. 22–23, pp. 5675–5687, 2008.

[66] M. C. Baietto, E. Pierres, and A. Gravouil, “A multi-model X-FEM strategy dedicated to frictional crack growth under cyclic fretting fatigue loadings,” *Int. J. Solids Struct.*, vol. 47, no. 10, pp. 1405–1423, 2010.

[67] C. Ruiz, Z. P. Wang, and P. H. Webb, “Techniques for the characterization of fretting fatigue damage,” *Stand. Frett. Fatigue Test Methods Equipment. ASTM Int.*, 1992.

[68] D. Nowell and D. A. Hills, “Crack initiation criteria in fretting fatigue,” *Wear*, vol. 136, no. 2, pp. 329–343, 1990.

[69] D. Socie, “Multiaxial fatigue damage models.,” *Trans. ASME. J. Eng. Mater. Technol.*, vol. 109, no. 4, pp. 293–298, 1987.

[70] K. Nishioka and K. Hirakawa, “Fundamental investigations of fretting fatigue: Part 3, some phenomena and mechanisms of surface cracks,” *Bull. JSME*, vol. 12, no. 51, pp. 397–407, 1969.

[71] K. N. Smith, T. H. Topper, and P. Watson, “A stress-strain function for the fatigue of metals(Stress-strain function for metal fatigue including mean stress effect),” *J. Mater.*, vol. 5, pp. 767–778, 1970.

[72] D. Socie, “Critical plane approaches for multiaxial fatigue damage assessment,” *Adv. multiaxial fatigue. ASTM Int.*, 1993.

[73] R. W. Neu, J. A. Pape, and D. R. Swalla, “Methodologies for linking nucleation and propagation approaches for predicting life under fretting fatigue,” *Frett. fatigue Curr. Technol. Pract. ASTM Int.*, 2000.

[74] S. Fouvry, P. Kapsa, and L. Vincent, “Quantification of fretting damage,” *Wear*, vol. 200, no. 1–2, pp. 186–205, 1996.

[75] K. Dang Van, “Macro-Micro Approach in High Cycle Multiaxial Fatigue,” *Advances in Multiaxial Fatigue*. pp. 120–130, 1983.

[76] K. Iyer and S. Mall, “Effects of cyclic frequency and contact pressure on fretting fatigue under two-level block loading,” *Fatigue Fract. Eng. Mater. Struct.*, vol. 23, no. 4, pp. 335–346, 2000.

[77] A. L. Hutson, T. Nicholas, and R. Goodman, “Fretting fatigue of Ti–6Al–4V under flat-on-flat contact,” *Int. J. Fatigue*, vol. 21, no. 7, pp. 663–669, 1999.

[78] J. A. Pape and R. W. Neu, “Influence of contact configuration in fretting fatigue testing,” *Wear*, vol. 225–229, no. PART II, pp. 1205–1214, 1999.

[79] C. D. Lykins, S. Mall, and V. Jain, “An evaluation of parameters for predicting fretting fatigue crack initiation,” *Int. J. Fatigue*, vol. 22, no. 8, pp. 703–716, 2000.

[80] S. M. Quraishi, M. M. Khonsari, and D. Baek, “A thermodynamic approach for predicting fretting fatigue life,” *Tribol. Lett.*, vol. 19, no. 3, pp. 169–175, 2005.

[81] A. B. Aghdam, A. Beheshti, and M. M. Khonsari, “On the fretting crack nucleation with provision for size effect,” *Tribol. Int.*, vol. 47, pp. 32–43, 2012.

[82] T. Zhang, P. E. Mchugh, and S. B. Leen, “Finite element implementation of multiaxial continuum damage mechanics for plain and fretting fatigue Mð r,” *Int. J. Fatigue*, vol. 44, pp. 260–272, 2012.

[83] R. Hojjati-Talemi and M. A. Wahab, “Fretting fatigue crack initiation lifetime predictor tool: Using damage mechanics approach,” *Tribol. Int.*, vol. 60, pp. 176–186, 2013.

[84] P. J. Golden, H. R. Millwater, and X. Yang, “Probabilistic fretting fatigue life prediction of Ti-6Al-4V,” *Int. J. Fatigue*, vol. 32, no. 12, pp. 1937–1947, 2010.

[85] T. Slack, B. D. Leonard, and F. Sadeghi, “Estimating life scatter in fretting fatigue crack initiation,” *Tribol. Trans.*, vol. 56, no. 4, pp. 531–535, 2013.

[86] P. A. McVeigh and T. N. Farris, “Finite Element Analysis of Fretting Stresses,” *J. Tribol.*, vol. 119, no. 4, p. 797, 1997.

[87] M. P. Szolwinski and T. N. Farris, “Mechanics of fretting fatigue crack formation,” *Wear*, vol. 198, no. 1, pp. 93–107, 1996.

[88] S. A. Namjoshi, S. Mall, V. K. Jain, and O. Jin, “Fretting fatigue crack initiation mechanism in Ti-6Al-4V,” *Fatigue Fract. Eng. Mater. Struct.*, vol. 25, no. 10, pp. 955–964, 2002.

[89] C. D. Lykins, S. Mall, and V. Jain, “A shear stress-based parameter for fretting fatigue crack initiation,” *Fatigue Fract. Eng. Mater. Struct.*, vol. 24, no. 7, pp. 461–473, 2001.

[90] D. M. Mulvihill, M. E. Kartal, A. V. Olver, D. Nowell, and D. A. Hills, “Investigation of non-Coulomb friction behaviour in reciprocating sliding,” *Wear*, vol. 271, no. 5–6, pp. 802–816, 2011.

[91] R. H. Talemi and M. A. Wahab, “Finite Element Analysis of Localized Plasticity in Al 2024-T3 Subjected to Fretting Fatigue,” *Tribol. Trans.*, vol. 55, no. 6, pp. 805–814, 2012.

[92] F. Mücklich, J. Ohser, and G. Schneider, “Die Charakterisierung homogener polyedrischer Gefüge mit Hilfe des räumlichen Poisson-Voronoi-Mosaiks und der Vergleich zur DIN 50 601,” *Zeitschrift für Met.*, vol. 88, no. 1, pp. 27–32, 1997.

[93] H. Espinosa and P. Zavattieri, “A grain level model for the study of failure initiation and evolution in polycrystalline brittle materials. Part I: Theory and numerical implementation,” *Mech. Mater.*, vol. 35, no. 3, pp. 333–364, 2003.

[94] A. Warhadpande, B. Jalalahmadi, T. Slack, and F. Sadeghi, “A new finite element fatigue modeling approach for life scatter in tensile steel specimens,” *Int. J. Fatigue*, vol. 32, no. 4, pp. 685–697, 2010.

[95] J. A. R. Bomidi, N. Weinzapfel, C.-P. Wang, and F. Sadeghi, “Experimental and numerical investigation of fatigue of thin tensile specimen,” *Int. J. Fatigue*, vol. 44, pp. 116–130, 2012.

[96] N. RAJE, T. SLACK, and F. SADEGHI, “A discrete damage mechanics model for high cycle fatigue in polycrystalline materials subject to rolling contact,” *Int. J. Fatigue*, vol. 31, no. 2, pp. 346–360, 2009.

[97] T. Slack and F. Sadeghi, “Explicit finite element modeling of subsurface initiated spalling in rolling contacts,” *Tribol. Int.*, vol. 43, no. 9, pp. 1693–1702, 2010.

[98] J. R. Shewchuk, “Triangle: Engineering a 2D Quality Mesh Generator and Delaunay Triangulator,” *Appl. Comput. Geom. Towar. Geom. Eng.*, pp. 203–222, 1996.

[99] D. Nowell and D. A. Hills, “Mechanics of Fretting Fatigue Tests,” *Int. J. Mech. Sci.*, vol. 29, no. 5, pp. 355–365, 1987.

[100] J. Lemaître, *A course on damage mechanics*. Springer-Verlag, Berlin; New York, 1992.

[101] Y. C. Xiao, S. Li, and Z. Gao, “A continuum damage mechanics model for high cycle fatigue,” *Int. J. Fatigue*, vol. 20, no. 7, pp. 503–508, 1998.

[102] H. Hertz, “On the Contact of Elastic Solids,” *J. Reine Angew. Math*, vol. 92, pp. 156–171, 1882.

[103] Y. Bergengren, “Literature review of contact fatigue part I: Experimental results,” *Swedish Inst. Met. Res. Rep. IM 3083*, 1993.

[104] E. V. Zaretsky, R. J. Parker, and W. J. . Anderson, “A study of residual stress induced during rolling,” *Trans. ASME J. Lubr. Technol.*, vol. 91, pp. 314–319, 1969.

[105] Y. Murakami and S. Usuki, “Quantitative evaluation of effects of non-metallic inclusions on fatigue strength of high strength steels II: Fatigue limit evaluation based on statistics for extreme value of inclusion size,” *Int. J. Fatigue*, vol. 11, no. 5, pp. 299–307, 1989.

[106] K. Nishioka, “On the effect of Inclusion upon the Fatigue Strength,” *J. Soc. Mater. Sci. Jpn*, vol. 6, pp. 382–385, 1957.

[107] N. Weinzapfel and F. Sadeghi, “Numerical modeling of sub-surface initiated spalling in rolling contacts,” *Tribol. Int.*, vol. 59, pp. 210–221, 2013.

[108] T. H. Kim, A. V. Olver, and P. K. Pearson, “Fatigue and fracture mechanisms in large rolling element bearings,” *Tribol. Trans.*, vol. 44, no. 4, pp. 583–590, 2001.

[109] O. Ito and E. R. Fuller, “Computer modelling of anisotropic grain microstructure in two dimensions,” *Acta Metall. Mater.*, vol. 41, no. 1, pp. 191–198, 1993.

[110] W. D. J. Callister, *Material Science and Engineering: An Introduction*. Wiley, New York, 2000.

[111] J. Lemaitre, “A Continuous Damage Mechanics Model for Ductile Fracture,” *J. Eng. Mater. Technol.*, vol. 107, pp. 83–89, 1985.

[112] V. V. Bolotin and I. L. Belousov, “Early fatigue crack growth as the damage accumulation process,” *Probabilistic Eng. Mech.*, vol. 16, no. 4, pp. 279–287, 2001.

[113] H. Styri, “Fatigue Strength of Ball Bearing Races and Heat-Treated 52100 Steel Specimens,” *Proc. ASTM*, vol. 51, pp. 682–700, 1951.

[114] T. E. Tallian, *Failure Atlas for Hertz Contact Machine Elements*. 1992.

[115] T. A. Harris and R. M. Barnsby, “Life ratings for ball and roller bearings,” *Proc. Inst. Mech. Eng. Part J J. Eng. Tribol.*, vol. 215, no. 6, pp. 577–595, 2001.

[116] X. Ai, “A Comprehensive Model for Assessing the Impact of Steel Cleanliness on Bearing Performance,” *J. Tribol.*, vol. 137, no. 1, p. 11101, 2014.

[117] Q. Chen, E. Shao, D. Zhao, J. Guo, and Z. Fan, “Measurement of the critical size of inclusions initiating contact fatigue cracks and its application in bearing steel,” *Wear*, vol. 147, no. 2, pp. 285–294, 1991.

[118] A. Bhattacharyya, G. Subhash, and N. Arakere, “Evolution of Subsurface Plastic Zone due to Rolling Contact Fatigue of Case Hardened Bearing Steel,” *Int. J. Fatigue*, vol. 59, pp. 102–113, 2013.

[119] M. Widmark, “Effect of material, heat treatment, grinding and shot peening on contact fatigue life of carburised steels,” *Int. J. Fatigue*, vol. 21, pp. 309–327, 1999.

[120] D. Scott, “Rolling contact fatigue,” *Treatise Mater. Sci. Technol.*, vol. 13, pp. 321–361, 1979.

[121] O. Zwirlein and H. Shlicht, “Rolling Contact Fatigue Mechanisms - Accelerated Testing versus Field performance,” *Roll. Contact Fatigue Test. Bear. Steels. ASTM Int.*, 1982.

[122] V. K. Sharma, “Roller contact fatigue study of austempered ductile iron,” *J. Heat Treat.*, vol. 3, no. 4, pp. 326–334, 1984.

[123] A. G. Haynes, “The case hardening of steel,” 1967.

[124] M. A. Klecka, G. Subhash, and N. K. Arakere, “Microstructure–Property Relationships in M50-NiL and P675 Case-Hardened Bearing Steels,” *Tribol. Trans.*, vol. 56, no. 6, pp. 1046–1059, Nov. 2013.

[125] N. Branch, G. Subhash, N. Arakere, and M. Klecka, “A new reverse analysis to determine the constitutive response of plastically graded case hardened bearing steels,” *Int. J. Solids Struct.*, vol. 48, no. 3–4, pp. 584–591, Feb. 2011.

[126] I. Choi, M. Dao, and S. Suresh, “Mechanics of Indentation of Plastically Graded Materials—I: Analysis,” *J. Mech. Phys. Solids*, vol. 56, no. 1, pp. 157–171, 2008.

[127] J. R. Cahoon, “An improved equation relating hardness to ultimate strength,” *Metall. Trans.*, vol. 3, no. 11, p. 3040, Nov. 1972.

[128] E. J. Pavlina and C. J. Van Tyne, “Correlation of Yield strength and Tensile strength with hardness for steels,” *J. Mater. Eng. Perform.*, vol. 17, no. 6, pp. 888–893, Dec. 2008.

[129] T. Reti, “Residual stresses in carburized, carbonitrided, and case-hardened components,” *Handb. residual Stress Deform. steel*, pp. 189–208, 2002.

[130] G. Parrish and G. S. Harper, *Production gas carburising: The pergamon materials engineering practice series*. Elsevier, 1985.

[131] G. T. Hahn, V. Bhargava, C. A. Rubin, Q. Chen, and K. Kim, “Analysis of the Rolling Contact Residual Stresses and Cyclic Plastic Deformation of SAE 52100 Steel Ball Bearings,” *J. Tribol.*, vol. 109, no. 4, p. 618, 1987.

[132] Y. Shen, S. M. Moghadam, F. Sadeghi, K. Paulson, and R. W. Trice, “Effect of retained austenite - Compressive residual stresses on rolling contact fatigue life of carburized AISI 8620 steel,” *Int. J. Fatigue*, vol. 75, pp. 135–144, 2015.

[133] S. Shimizu, K. Tsuchiya, and K. Tosha, “Probabilistic Stress-Life (P-S-N) Study on Bearing Steel Using Alternating Torsion Life Test,” *Tribol. Trans.*, vol. 52, no. 6, pp. 807–816, 2009.

[134] A. Mihailidis, J. Retzepis, C. Salpistis, and K. Panajiotidis, “Calculation of friction coefficient and temperature field of line contacts lubricated with a non-Newtonian fluid,” *Wear*, vol. 232, no. 2, pp. 213–220, 1999.

[135] A. Mihallidis, C. Salpistis, N. Drivakos, and K. Panagiotidis, “Friction behavior of FVA reference mineral oils obtained by a newly designed two-disk test rig,” *Int. Conf. Power Transm.*, vol. 3, 2003.

[136] J. J. Coy, E. V. Zaretsky, and G. R. Cowgill, “Life Analysis of Restored and Refurbished Bearings,” *NASA Lewis Res. Cent.*, 1977.

[137] J. Alexander, “Bearing Repair Provides Valuable Alternative To Bearing Replacement for Heavy Industries,” *South Carolina Timken Ind. Serv. Center.*, 1985.

[138] E. V Zaretsky and E. V Branzai, “Model Specification for Rework of Aircraft Engine , Power Transmission , and Accessory / Auxiliary Ball and Roller Bearings,” *Power Transm. Accessory/Auxiliary Ball Roll. Bear.*, 2007.

[139] “Bearing Repair Services Offer a Cost-Effective Alternative to Expensive Replacement,” *Coal Age*, vol. 114, no. 2, pp. 48–50, 2009.

[140] M. N. Kotzalas and M. R. Eckels, “Repair as an Option to Extend Bearing Life and Performance,” *SAE Tech. Pap.*, no. No. 2007-01-4234, 2007.

[141] E. V. Zaretsky and E. V. Branzai, “Effect of Rolling Bearing Refurbishment and Restoration on Bearing Life and Reliability,” *Tribol. Trans.*, vol. 48, no. 1, pp. 32–44, 2005.

[142] R. M. Barnsby (Ed.), “Life ratings for modern rolling bearings: a design guide for the application of International Standard ISO 281/2,” *Am. Soc. Mech. Eng.*, vol. 1, 2003.

[143] N. R. Paulson, N. E. Evans, J. A. R. Bomidi, F. Sadeghi, R. D. Evans, and K. K. Mistry, “A finite element model for rolling contact fatigue of refurbished bearings,” *Tribol. Int.*, vol. 85, pp. 1–9, 2015.

[144] M. Erdogan and S. Tekeli, “The effect of martensite particle size on tensile fracture of surface-carburised AISI 8620 steel with dual phase core microstructure,” *Mater. Des.*, vol. 23, no. 7, pp. 597–604, Oct. 2002.

[145] H. Boyer, *Case hardening of steel*. 1987.

[146] A. P. Voskamp, “Material Response to Rolling Contact Loading,” *J. Tribol.*, vol. 107, no. 3, p. 359, 1985.

[147] J. A. R. Bomidi *et al.*, “Experimental and Numerical Investigation of Torsion Fatigue of Bearing Steel,” *J. Tribol.*, vol. 135, no. 3, p. 31103, 2013.

[148] A. A. Walvekar, D. Morris, Z. Golmohammadi, F. Sadeghi, and M. Correns, “A Novel Modeling Approach to Simulate Rolling Contact Fatigue and Three-Dimensional Spalls,” *J. Tribol.*, vol. 140, no. 3, p. 31101, Oct. 2017.

[149] N. R. Paulson, F. Sadeghi, and W. Habchi, “A coupled finite element EHL and continuum damage mechanics model for rolling contact fatigue,” *Tribol. Int.*, vol. 107, pp. 173–183, Mar. 2017.

[150] E. O. Hall, “The Deformation and Ageing of Mild Steel: III Discussion of Results,” *Proc. Phys. Soc. Sect. B*, vol. 64, no. 9, pp. 747–753, Sep. 1951.

VITA

Aditya Avdhut Walvekar was born on September 22nd, 1989 in Mahbubnagar, India. He attended the Birla Institute of Technology and Science (BITS), Pilani – Goa Campus, India where he received his Bachelor of Engineering (Honors) in Mechanical Engineering degree in June 2011. He then pursued graduate studies at Purdue University, West Lafayette, IN and obtained a Master of Science in Mechanical Engineering in May, 2014. He continued on for his doctoral studies and earned his Doctor of Philosophy degree in December, 2017 under the supervision of Professor Farshid Sadeghi. His research interests are in the areas of fatigue, tribology, numerical simulation, and material modeling.